Luminescent Heteroatom doped Carbon Quantum Dots for Sensing and Drug Delivery Applications

Rahul Kumar Das

Department of Chemistry
National Institute of Technology Rourkela

Luminescent Heteroatom doped Carbon Quantum Dots for Sensing and Drug Delivery Applications

Dissertation submitted in partial fulfillment

of the requirements for the degree of

Doctor of Philosophy

in

Chemistry

by

Rahul Kumar Das

(Roll Number: 513CY6080)

based on research carried out

under the supervision of

Prof. Sasmita Mohapatra

January, 2019

Department of Chemistry

National Institute of Technology Rourkela

Department of Chemistry
National Institute of Technology Rourkela

, , 2019

Certificate of Examination

Roll Number: *513CY6080*

Name: *Rahul Kumar Das*

Title of Dissertation: *Luminescent Heteroatom doped Carbon Quantum Dots for Sensing and Drug Delivery Applications*

We the below signed, after checking the dissertation mentioned above and the official record book (s) of the student, hereby state our approval of the dissertation submitted in partial fulfillment of the requirements of the degree of *Doctor of Philosophy* in *Chemistry* at *National Institute of Technology Rourkela*. We are satisfied with the volume, quality, correctness, and originality of the work.

Prof. Sasmita Mohapatra
Principal Supervisor

Prof. Bibhuti Bhushan Nayak
Member, DSC

Prof. Braja Gopal Mishra
Member, DSC

Prof. Debayan Sarkar
Member, DSC

Prof. Paritosh Mohanty
I.I.T. Roorkee
External Examiner

Prof. Niranjan Panda
Chairperson, DSC

Prof. Rupam Dinda
Head of the Department

Department of Chemistry
National Institute of Technology Rourkela

Prof. Sasmita Mohapatra
Associate Professor

, , 2019

Supervisors' Certificate

This is to certify that the work presented in the dissertation entitled *Luminescent Heteroatom doped Carbon Quantum Dots for Sensing and Drug Delivery Applications* submitted by *Rahul Kumar Das*, Roll Number 513CY6080, is a record of original research carried out by him under my supervision in partial fulfillment of the requirements of the degree of *Doctor of Philosophy* in *Chemistry*. Neither this dissertation nor any part of it has been submitted earlier for any degree or diploma to any institute or university in India or abroad.

Dr. Sasmita Mohapatra
Associate Professor

Dedicated to my mother

Signature

Declaration of Originality

I, *Rahul Kumar Das*, Roll Number *513CY6080* hereby declare that this dissertation entitled *Luminescent Heteroatom doped Carbon Quantum Dots for Sensing and Drug Delivery Applications* presents my original work carried out as a doctoral student of NIT Rourkela and, to the best of my knowledge, contains no material previously published or written by another person, nor any material presented by me for the award of any degree or diploma of NIT Rourkela or any other institution. Any contribution made to this research by others, with whom I have worked at NIT Rourkela or elsewhere, is explicitly acknowledged in the dissertation. Works of other authors cited in this dissertation have been duly acknowledged under the "Reference" section. I have also submitted my original research records to the scrutiny committee for evaluation of my dissertation.

I am fully aware that in case of any non-compliance detected in future, the Senate of NIT Rourkela may withdraw the degree awarded to me on the basis of the present dissertation.

Rahul Kumar Das

NIT Rourkela

Acknowledgment

First of all, I would like to express my profound gratitude to my supervisor Prof. Sasmita Mohapatra for her excellent guidance, constant encouragement, continuous support, generous help and inspiration during the entire period of my research work. I would believe myself really fortunate to be associated with her at the important turn of my career.

I wish to express my sincere thanks to Director, NIT Rourkela for providing necessary facilities to carry out this research work. I am grateful to Prof. Rupam Dinda, Head, Department of Chemistry, NIT Rourkela for fulfilling the academic needs of my Ph.D. programme.

I sincerely thank Prof. Niranjan Panda, for his valuable training, guidance and contribution to my scientific work at the time of requirement.

I thank to my DSC members Prof. Bibhuti Bhusan Nayak, Prof. Braja Gopal Mishra and Prof. Debayan Sarkar for their valuable suggestions during this program.

I wish to place on record my appreciation to numerous technical and non-technical staffs of Department of Chemistry, NIT, Rourkela who have lent their expertise and cooperation at various stages of their endeavour. Especially, I would like to mention Mr. Samir, Ms. Swagatika , Mr. Pratap, Mr. Arup, Mr. Nitya and Mr. Murali for their help during this program.

I am indebted to our collaborators, Prof. Sujit Kumar Bhutia, Department of Life Sciences, NIT Rourkela for his brilliant input in carrying out all biological work and Dr. Megharay Majhi, Department of Radiodiagnosis, Ispat General Hospital, Rourkela for his unconditional support in performing MRI experiments. I thank Dr. Arindam Pramanik, for his assistance in some of the *in vitro* studies. I owe my appreciation to Mr. Chandra S. Bhol for his cooperation in handling the biological experiments.

My sincere regards to Prof. N.D. Pradeep Singh, Department of Chemistry, I.I.T. Kharagpur and Prof. Ramesh Ramapanicker, Department of Chemistry, I.I.T. Kanpur for blessing me with the opportunity of cultivating theoretical-technical knowledge and being trained at their respective laboratories.

It is a great pleasure for me to acknowledge all my lab mates Dr. Smruti, Dr. Swagatika, Dr. Ashis, Mr. Mihir, Ms. Snigdha, Mr. Arun, Mr. Swayam, Ms. Supriya, Mr.

Vinay, Mr. Pradyumna, Mr. Sitikantha, Mr. Tino, Mr. Kushagra, Ms. Arpita, Mr. Balaram and Ms. Sangita for being friendly, helpful and supportive throughout.

Indescribable thanks to my mother Smt. Baby Mohanty without whose continuous moral and determined support, I would be incomplete for this life and degree. Words cannot express how grateful I am to Ms. Aarti, Sunita auntie, Saranjit auntie, Ms. Baljeet Kaur, Bijaya uncle, Sarabjit uncle, Mr. Tanveer Singh, Mr. Inder Tej Veer Singh and lovable little one's Subhashree, Meher and Ganeev for all of their support in my cheerful personal life. Sincere thanks to Mr. Partha Pratim Hazra (Subject), Mr. Abhishek Garai (Photocatalysis), Mr. Sourabh Bera (Spectroscopy support) and Mr. Shivam Dalaniya (Award presentation) for their support on technical and professional grounds. Your prayer for me was what sustained me thus far.

I place on record my thankfulness to seniors and colleagues, Dr. Rakesh Muduli, Dr. Satyabrata Satpathy, Dr. Sarita Garnayak, Dr. Prakash Malik, Dr. Sudhakar Reddy, Dr. Nishant Tiwari, Dr. Sunirmal Saha, Dr. Pankaj Prasad, Dr. Aaryan Kashyap, Er. Om Das, Er. Digvijay Singh, Er. Mahdi Eskandari, Er. Prateek Kar, Er. Ayush Pradhan, Er. Souvik Dutta, Mr. Fakira Bastia, Er. Satyanarayan Sabat, Er. Prasamit Nath, Er. Love Dashariya, Er. Satya Gope, Mr. Rahul Agarwal, Er. Subham Singh, Er. Nikhil Chandra and Er. Piyush Pritam for making my stay in this campus and research coordination a memorable one.

Rahul Kumar Das

NIT Rourkela 513CY6080

Abstract

The present dissertation entitled, “Luminescent Heteroatom doped Carbon Quantum Dots for Sensing and Drug Delivery Applications” is an embodiment of the investigations aimed at developing simple inexpensive synthetic methodologies for producing heteroatom doped carbon quantum dots pertinent for sensing and biomedical application. The diagnostic and therapeutic applications of these multifunctional nanomaterials have been studied in vitro. The thesis has been divided into seven chapters.

Hydrophilic boronic acid modified nitrogen sulphur doped carbon quantum dots (BNSCQD) have been prepared following a cost effective hydrothermal approach. The co-doping is aimed to improve the luminescence as well as targeting affinity of the CQD. Due to intense fluorescence property, appreciable photostability, boronic acid functionality and low cytotoxicity the carbon quantum dots (CQD) have been utilised in sensing glucosamine and cancer cell receptor Sialyl Lewis^{a} (SL^{a}). This method is highly sensitive and selective for visual detection of glucosamine sensing using a paper based sensor strip. Furthermore, integration of dopamine with BNSCQD (BNSCQD-Dopa) sets a platform for development of a fluorescence turn-on nanoprobe for fluoride detection in real samples. Due to boron’s affinity towards fluorine, the system was very selective towards fluoride when compared with other anions with a detection limit 0.7 pM. The practical ultrasensitive utility of the sensor is well demonstrated in human serum samples and also extended for fluoride detection in cellular environment. Further, the BNSCQD has been integrated with gadolinium iron oxide and mesoporous silica to construct a theranostic nanoparticle where BNSCQD imparts multiple functions such as simultaneous pH-sensitive gate opening, leading to control drug release, optical imaging, and receptor targeted internalization of the theranostic particle. The drug release experiment under variable pH and in the presence of competitive binding ligand SLa clearly shows the excellent responsiveness of the BNSCQD capped MSN hybrid system toward dual stimuli. Because of reasonably good r1 r2 relaxivities of the magnetic core and excellent fluorescence property of the doped carbon quantum dot, the hybrid can be utilized to

monitor the therapeutic response through MRI and/or fluorescence imaging. Nitrogen doped mesoporous hollow carbon nanospheres (NCQD-HCS) have been prepared by inert calcination of polymer synthesized using pyrrole, aniline and Triton X-100 as molecular precursors. Here a direct synthetic approach is followed to yield high surface area carbon spheres with fluorescence property. An optimization of both surface area and photoluminescence is achieved by tuning temperature of calcination. The highest PL quantum yield of 14.6% is recorded, which is suitable for confocal imaging of cells. The fluorescence property of these spheres is attributed to the embedded nitrogen doped carbon quantum dots (NCQD) in carbon matrix. The photothermal property of NCQD-HCS has been investigated under 980 nm NIR irradiation. Cell killing efficacy of hollow spheres by photothermal ablation effect is evaluated in FaDu cells (oral cancer) as a modal cell line. Similarly, the upconversion property of carbon spheres is explored for light responsive drug release of gemcitabine. A highly biocompatible click chemistry based gating system is designed to restrict the premature release of drug molecules from porous nanospheres. The utilization of upconverted radiation by substituted nitrobenzyl linker, initiating its cleavage followed by drug release under periodic irradiation (980 nm laser) intervals has been tested in vitro. These fluorescent multifunctional nanoparticles provide a platform for combinatorial therapy of oral cancer.

Table of Contents

GLOSSARY

Abbreviation	Expansion
3-APBA	3-aminophenyl boronic acid
5-Fu	5-Fluorouracil
APTS	(3-Aminopropyl)triethoxysilane
BCQD	Boron doped Carbon Quantum Dot
BET	Brunauer-Emmett-Teller
BJH	Barrett-Joyner-Halenda
BNSCQD	Boron, Nitrogen, Sulphur co-doped Carbon Quantum Dot
CNT	Carbon Nanotube
CQD	Carbon Quantum Dot
CTAB	Cetyltrimethylammonium bromide
Cu(I)CQD	Copper doped Carbon Quantum Dot
DA	Dopamine
DAPI	4',6-diamidino-2-phenylindole
DMEM	Dulbecco's Modified Eagle Media
DMSO	Dimethyl sulfoxide
EDAX	Energy-Dispersive X-ray Analysis
EPA	Environmental Protection Agency
EPR	Enhanced Permeability and Retention
FACS	Fluorescence-Activated Cell Sorting
FBS	Fetal Bovine Serum
FESEM	Field Emission Scanning Electron Microscopy
FLQY	Fluorescence Quantum Yield
FRET	Fluorescence Resonance Electron Transfer
FTIR	Fourier-Transform Infrared spectroscopy
GdIO	Gadolinium oxide-Iron oxide
HCS	Hollow Carbon Sphere
HRTEM	High Resolution Transmission Electron Microscopy
LOD	Limit of Detection
MEM	Minimum Essential mMedium
MRI	Magnetic Resonance Imaging
$mSiO_2$	Mesoporous Silica
MSN	Mesoporous Silica nanoparticles
MTT	3-(4,5-dimethylthiazol-2-yl)-2,5-diphenyl tetrazolium bromide
NCQD	Nitrogen doped Carbon Quantum Dot
NIR	Near-Infrared
NPCQD	Nitrogen, Phosphorus co-doped Carbon Quantum Dot
NSCQD	Nitrogen, Sulphur co-doped Carbon Quantum Dot
PACP	Polyaniline-co-polypyrrole
PBS	Phosphate Buffer Saline
PCQD	Phosphorus doped Carbon Quantum Dot
PEG	Polyethylene Glycol
PET	Photoinduced Electron Transfer
PFA	Paraformaldehyde
PL	Photoluminescence
PTT	Photothermal Therapy

r1	Longitudinal relaxivity
r2	Transverse relaxivity
SCQD	Sulphur doped Carbon Quantum Dot
SEM	Scanning Electron Microscopy
SiCQD	Silicon doped Carbon Quantum Dot
SiO_2	Silica
SL^a	sialyl Lewis a
STEM	Scanning Transmission Electron Microscopy
T1	Longitudinal relaxation Time
T2	Transverse relaxation Time
TEM	Transmission Electron Microscopy
UV	Ultra Violet
XPS	X-ray Photoelectron spectroscopy
XRD	X-ray Diffraction

Measurements

mL	millilitre
mg	milligram
m^2g^{-1}	metre square per gram
mm	millimetre
mM	millimolar
mmol	millimole
$mM^{-1}s^{-1}$	Per millimolar per second
µM	micromolar
µL	microlitre
µg	microgram
eV	Electron volt
emu g^{-1}	Electromagnetic unit per gram
nm	nanometre
nM	nanomolar
pM	picomolar
mL^{-1}	Per mililitre
$µL^{-1}$	Per microlitre
cm^{-1}	Per centimetre
λ_{em}	Emission wavelength
λ_{ex}	Excitation wavelength
min	minute
h	hour
Hz	Hertz
IC50	inhibitory concentration 50

Chapter – 1

Literature review on doped carbon quantum dots and their application as fluorescent nanoprobe for sensing and drug delivery

1.1 Introduction

Carbon quantum dots were first discovered as a new family of quantum dots (QDs) in 2004, subsequently emerged as an excellent fluorescent nanomaterial.[1] In current research advancement, the fluorescent carbon quantum dots have shown enormous potentials for biomedical and optoelectronic applications owing to their outstanding properties such as appreciable biocompatibility, low cytotoxicity, photostability and versatility in addition to their unique tunable photoluminescence and other exceptional physicochemical properties.[2-4] Moreover, compared to organic dyes and traditional semiconductor QDs, not only are CQDs advantageous in terms of photostability against photobleaching and blinking, they also have a lower toxicity and better biocompatibility.[5,6] Owing to their low cost and ease of synthesis, they have been extensively applied in areas such as optical sensing, bioimaging, photocatalysis and electrocatalysis.[7-12] Fundamental approaches to tune the responses of CQDs towards photo-interactions and the design of bionanoprobes are presented, which enable biomedical applications involving diagnostics and therapeutics.[13-16] These strategies represent comprehensive platforms for engineering multifunctional probes for nanomedicine.

Tailoring carbon nanomaterials with heteroatoms can effectively tune their electronic and chemical properties.[17-19] Among many heteroatoms, nitrogen, which has an atomic size comparable to that of neighbouring carbon, has been the most widely employed heteroatom for the chemical doping of carbon nanomaterials leading to a modulated bandgap in carbon quantum dots.[20] In addition, recent approaches have extended to the co-doping of heteroatoms like S, P, B, Si etc. to take the advantage of the synergetic coupling effect between heteroatoms, which facilitates charge distribution, and enhanced optical properties.[21-26]

1.2 Synthesis of doped carbon quantum dots

Numerous approaches exist for the successful synthesis and functionalization of carbon quantum dots. However, CQDs have relatively low emission efficacy when compared to the conventional semiconductor quantum dots, even after surface passivation and functionalization. Furthermore, the majority of CQDs require higher degree of passivation to obtain significant luminescence which makes the preparation process complex and limits their use in industrial scale applications. Therefore, efficient means for increasing the photoluminescence properties of CQDs remained a challenge to enlarge their

biomedical application potential. Recently, the doping approach has proved well to tune the fluorescent properties of CQDs and considered as a most promising engineering pathway for the purpose. As briefly introduced earlier, doping elements can be generally classified into metal atoms and heteroatoms (non-metal). The major obstacle to metal-atom doping is the associated increase in toxicity. Hence, this part will mainly concentrate on non-metal based heteroatom doping of CQDs which attracted much attention in recent years. Various doping methods with heteroatoms have been reported to improve the optical and electronic properties of CQDs. The effect of different elements, including single- and co-doping, on the properties (PL properties) of the prepared CQDs is reviewed.

Single-heteroatom doping

(i) Doping with nitrogen. Due to the close similarity between N and C, N-doping is the most widely used way to improve the PL properties of CQDs. Here, the nitrogen atom contributes electrons into CQDs and changes the internal electronic environment, which effectively improve their fluorescence properties. N-Doped CQDs showed excellent performance in biomedical applications such as biosensing and imaging.

Till date, there have been various top-down approaches reported for preparing highly fluorescent N-doped CQDs. One of the main strategies focuses on leveraging the abundance and sustainability of natural biomass materials to provide a cheap and green route for producing CQDs. Zhang et al. prepared highly luminescent N-doped CQDs by hydrothermal treatment of ethylenediamine.[27] The CQDs were prepared at 200^{o}C and exhibited blue fluorescence with a high photoluminescence quantum yield (PLQY) of 66.8%. Chen and co-workers reported a one-pot solvothermal synthesis of NCQDs by heating different carbon chains (1,2-ethylenediamine, 1,3-propanediamine, and 1,4-butanediamine) of diamines to compare the influence of nitrogen percentage and effect on the PLQY of NCQDs.[28] The reaction was carried out in glycol solution. The resultant CQDs had a relatively narrow size distribution of 6-10 nm, comprised of 20.23 wt% doped N content and exhibited a higher PL QY of 20.4%. However, the aforementioned CQDs have a relatively low PLQY efficiency mainly due to the relatively low percentage of nitrogen in CQDs. Similarly, Wei et al prepared NCQDs with an average diameter of 2.5 nm using diethylene triamine pentacetate acid as precursor. But the limitations to this

reports was high reaction temperature of 250^{o}C and its property of excitation independent emission. Thus, the bottom-up approach was widely used to prepare N-doped CQDs in recent years.

On the other hand, Huang et al prepared N-Doped CQDs varying reaction time (1-48h) by using urea and ethylenediamine as the precursors. Interestingly, the resultant CQDs exhibited multi-band emissions with an increase in reaction time with an efficient PLQY up to 49.6%.[29] Nevertheless, microwave assisted synthesis of NCQDs using isophorone diisocyanate reduced the reaction time from hours to minutes.[30] Yue et al showed a novel NCQD preparation which involves no corrosive acid, alkali or organic solvent. The particle size ranged from 2.2-5 nm in diameter with a PLQY of 11%. The low reaction time and uniform particle size attained from this method made the resultant N-doped CQDs as well as the method a promising candidate for large-scale production. For instance, Huang and co-workers reported a low temperature hydrothermal approach to prepare the N-doped CQDs at 140^{o}C with a QY of 22.6%. [31] They used polyethyleneimine as the nitrogen precursor and yielded the lowest particle size upto 3.8 nm with a nitrogen-carbon atomic ratio of 0.32.

(ii) Doping with sulphur. Compared to the extent of research to produce N-doped CQDs, CQDs containing a single S atom have been rarely reported. For instance, S-doped CQDs (SCQDs) were reported by Tang et al., who used cellulose and sulphuric acid as the precursors.[32] First, the cellulose was acid hydrolysed in the presence of sulfuric acid (64%, w/w) at 60 ^{o}C for 1 h. Then, transferred to autoclave and carbonized at 200^{o}C for 4h to synthesize the S-CQDs. The SCQDs exhibited a relatively high fluorescence QY of 32% with a particle size distribution of 2.5-6 nm. Gupta et al. reported microwave assisted synthesis of SCQDs using citric acid and sodium thiosulfate at 600 W for 6 min.[33] The SNCQDs were implied for sensing arsenic and glutathione. Recently, Yang et al. doped sulphur by thermolysis using 5-sulfosalicylic acid.[34] The reaction was performed using ethylene glycol as solvent and at 200^{o}C with a constant heating rate at 5^{o}C.

(iii) Doping with boron: In 2014, two consecutive groups reported synthesis of B-doped CQDs (BCQDs) using solvothermal treatment, but used different chemical precursors. Shen et al.[35] used phenylboronic acid and Shan et al.[36] used hydroquinone and boron tribromide as starting materials respectively. The phenylboronic acid was dissolved in ultrapure water and maintained under basic condition, followed by hydrothermal treatment

at 160^{o}C for 8h. BCQDs exhibited particle size distribution within the range of 2.5-6.5 nm with a quantum yield of 8.4%. However, Shan et al. BCQDs particle size distribution ranged between 2-22 nm with 14.8 % quantum yield. Further, Nanda et al. too followed hydrothermal method but used sucrose and boric acid as precursors.[37] Here the CQDs were prepared at a temperature of 180oC and standardized based on variation of treatment time. Thus, concluded that particle growth is directly proportional to reaction time. The particle size distribution was found to be within the range of 3.7-6 nm and exhibited highest quantum yield of 2.7%.

(iv) Doping with phosphorous: In view of the capability of phosphorous (P) to act as an n-type donor and form substitutional defects in sp^3 thin films, doping CQDs with P atoms is expected to alter the optical and electronic properties. Several groups successfully produced P-doped CQDs (PCQDs) from different phosphorus containing precursors in recent years. Feng and co-workers employed phosphorous tribromide (PBr_3) as a phosphorus source as the phosphorus precursor.[38] For this, PBr_3 and hydroquinone were first dissolved in acetone and then heated at 200^{o}C for 1 h using a blast oven. After cooling and rotary evaporation, the final P-doped CQDs were obtained. The diameters of the as-prepared CQDs had a wide distribution of 5-15 nm while exhibited a PLQY of up to 25% with excitation at 372 nm. Elemental analysis showed a composition of 65.4 wt% C, 24.2 wt% O and 8.5 wt% for the P-doped CQDs. Recently, Li et al reported synthesis of phosphorus doped carbon quantum dots using hydrothermal method.[39] Phytic acid was used as precursor to prepare the PCQDs at 240^{o}C. The particle size for the CQD ranged from 2.5-4.5 nm. The PCQDs with a phosphorous content of 8.52 wt% exhibited a quantum yield of 3.5%.

(v) Doping with metalloids: It is well known that boron is the left neighbour of carbon in the periodic table of elements. Thus, it is an obvious choice for doping carbon-based nanomaterials. Feng et al. prepared B-doped CQDs using BBr_3 and hydroquinone as the boron and carbon precursor, respectively. The resultant B-CQDs possessed a size distribution of 8-22 nm and was comprised of 69.4% C, 21.0% O, and 5.0% B and 3.6% bromine.It exhibited bright blue fluorescence with a QY of up to 14.8%. This work suggested that boron can also act as an active site for charge transfer in CQDs. Similarly, Wu et al. prepared silicon doped CQD (SiCQDs) using N-[3-(trimethoxysilyl)propyl]ethylenediamine as precursor.[40] The synthesis was achieved by

solvothermal treatment of precursor in glycerol at 260^{o}C for 12h. Here, SiCQDs exhibited a particle size of 6 nm and quantum yield upto 45% respectively.

Co-doping multiple heteroatoms

Co-doping multiple heteroatoms has begun to gain much attention because it can create a unique electronic structure, due to the synergistic effect between the doped heteroatoms in CQDs. The following sections summarize important efforts reported regarding co-doping of CQDs and its effect on PLQY.

(i) Doping with nitrogen and sulphur. N and S co-doped CQDs (NSCQDs) have been actively investigated by many research groups recently and found to be an ideal pathway for enhancing the PL properties. Currently, three different reports were done based on the synthesis of N, S co-doped CQDs. Kang et al. reported the synthesis of NSCQD by combustion flame technique.[41] Here, dodecanethiol and pyrrole were used as precursors and combustion time was maintained for 4 h. The NSCQDs exhibited an average particle size of 5 nm. Macfarlane et al. synthesized N, S co-doped CQDs via pyrolysis of N-Methylethanolammonium thioglycolate at 450^{o}C.[42] The particle size was within range of 6-10 nm with a QY of 12.5%. Liu et al. prepared the NSCQDs using L-cysteine and ammonium hydroxide as precursor.[43] The synthesis was performed by facile hydrothermal treatment of precursors at 100^{o}C for 12 h. Here, the particle size distribution was found to be within 5-10 nm with a QY of 17.2% respectively. Sulphur doping creates both surface defects as well as heavy atom effect when incorporated in nitrogen containing CQDs. This enhances the photoluminescence and selectivity property of CQDs.

(ii) Doping with nitrogen and phosphorus. Doping N and P atoms into CQDs (NPCQDs) is expected to produce the co-doped CQDs with new and unanticipated properties due to combined benefits from each of the doped atoms. Zhao et al, proposed the first strategy to produce N-P co-doped CQDs through a facile and low-cost hydrothermal process.[44] They prepared high PLQY CQDs using adenosine 5′-monophosphate as precursor. The precursors were uniformly dissolved in water and then placed into an oven at 180^{o}C for 8 h. The resulting N-P CQDs presented a uniform particle size distribution between 1.2 and 6.25 nm, and the PLQY was estimated to be 26.5% with a decay time of 4.3 ns. Recently, a different strategy of acid-base reaction heat method

was adopted by Dong et al., to synthesize NPCQDs from ethylene diamine, phosphoric acid and glucose using a green route.[45] The resultant N-P co-doped CQDs had a PLQY of 9.6% with a strong blue luminescence when excited at 340 nm. Here, NPCQDs exhibited a uniform particle size distribution between 4.24 and 6.33 nm, and a decay time of 7.03 ns. However, Liu and co-workers produced NPCQDs from hydrothermal treatment of triple-helical tropocollagen molecules.[46] The resulting N-P CQDs presented a uniform particle size distribution between 1.36 and 2.06 nm, and the PLQY was estimated to be 15% with a decay time of 6.88 ns. The synthesis here showed a difference in photophysical property by comparative study of CQDs prepared from assembled and unassembled triple-helical tropocollagen molecules. Cai et al. reported the hydrothermal synthesis of NPCQD with highest quantum yield upto 53.8%.[47] Here, sodium citrate and diammonium phosphate were used as precursors and reaction temperature and time was standardized to 170^{o}C and 6h respectively. As-prepared CQDs showed a particle size distribution in diameter of 2-5.5 nm range. More recently, a one-pot hydrothermal synthesis strategy to fabricate highly luminescent NPCQDs with PLQY up to 32% was reported by Hou et al.[48] The CQD was derived using m-phenylenediamine and methylenephosphonicacid as reactants. Particle size distribution of NPCQDs ranged between 3.74-7.83 nm in diameter. The CQDs exhibited two absorption peaks (294 nm and 457 nm) and a bright green fluorescence emission upon excitation at 365 nm. Furthermore, these various NPCQDs were implied as chemosensors for the detection of biomolecules and hazardous organic moieties in living cells based on confocal fluorescence. By far, N, P co-doped CQDs have begun to attract much attention due to their excellent fluorescence. Though the exact mechanisms still remain unclear, it is reasonable to believe that the co-doping technique can help to extend the C-dot applications in chemical sensing, biosensing, nanomedicine, and photocatalysis.

(iii) Doping with nitrogen and boron. Boron is the left and nitrogen is the right neighbour of carbon in the periodic table. Doping of these two neighbours in a carbon-based nanomaterial is of fundamental as well as of practical importance. But till date only Leng et al. have reported hydrothermal synthesis of N, B doped CQDs using ethylene diamine and 2-hydroxyphenylboronic acid as precursors.[49] The preparation required a temperature of 180^{o}C for 12 h. Here, CQDs exhibited yellowish-green fluorescence and possessed a quantum yield of 6.59%. The CQDs were used in sensing and visualizing of Cr(VI) ions in living cells.

(iv) Doping with metal and non-metals. In addition to the aforementioned doping elements, only metal atoms, metal-heteroatom co-doping is also reported to improve the fluorescence properties of CQDs. Metals such as Mg (Mg-N-codoped), Co (Co-N-co-doped) are reported to enhance the properties of CQDs when co-doped in combination with other elements such as N. For instance, Huang et al. reported the synthesis of Cu(I) doped CQDs using thermolysis method using disodium copper-EDTA complex as a copper source and ascorbic acid as a carbon source.[50] They demonstrated that doped Cu(I) was reduced from Cu(II) using ascorbic acid as the reducing agent during the thermolysis process at 250^{o}C. They have proposed that the absorption intensity of Cu(I) CQDs was higher than that of either CQDs or Na_2[Cu(EDTA)], which could be attributed to the presence of Cu-N dopants, which in turn would have produced Cu-to-graphite charge-transfer (CT) absorption. The particle size distribution was in the range of 3.2-4.9 nm. Recently, three different synthetic approaches were made to synthesize gadolinium doped CQDs for application in multimodal imaging. Chang and co-workers synthesized gadalonium, nitrogen and sulphur co-doped CQDs (GdNSCQD) using microwave irradiation.[51] Here, the precursors used were sodium citrate, gadolinium chloride, sodium sulphide and N-acetyl-L-cysteine. The preparation was done at 220oC with reaction time of 10 min. The QY of GdNSCQD was found to be 12.8% with r2/r1 ratio of 1.31 respectively. GdNSCQDs synthesized in this work possessed an average particle size of 4.3 nm. Yi et al. prepared GdCQDs followed thermolysis method and used gadopentetic acid, polyethylenimine, citric acid as precursors.[52] Due to the N doping by polyethylenimine, the PLQY for CQDs prepared under this synthesis was upto 40%. The CQDs exhibited a r2/r1 ratio of 1.14 with a particle size distribution range of 10-20 nm. On the other hand, Liu and co-workers reported a hydrothermal synthesis of GdCQDs using gadopentetate monomeglumine as a mono precursor.[53] Here, the temperature and time was standardization to 220^{o}C and 8 h, which yielded with the best QY of 7.1%. The CQDs emitted blue fluorescence when exposed to 365 nm wavelength. Similarly, hydrothermal synthesis of lanthanium doped CQDs were reported by Zhou and co-workers using adenosine disodium triphosphate (ATP) and lanthanium (III) chloride as precursors.[54] This synthesis proposes that ATP ionizes into negative ions after dissolving in water, then La^{3+} and ATP coordinate with each other to form ATP crosslinking. La^{3+} has a larger radius and higher coordination number than other transition metals. Finally, with the increase of temperature, the amino and hydroxyl groups may interact with phosphoric acid groups to undergo dehydration, condensation, and carbonization. The

surface of lattice structures of La-CQDs possesses abundant phosphate, hydroxy, carboxyl and amino groups that endowed the La-CQDs with attractive photoluminescence and excellent water dispersibility. Recently, Mohapatra and co-workers too synthesized nitrogen, boron, sulphur co-doped CQDs (BNSCQDs) using hydrothermal treatment.[55] The reaction temperature and time was standardized to 180^{o}C and 6 h with a quantum yield of 28% respectively. It was proposed that nitrogen doping introduces new types of surface states, which are able to facilitate a high yield of radiative recombination and sulphur enhances the effect of nitrogen atoms in doped CQD through a cooperative effect, whereas boron centre facilitates as an engine to delocalize the electrons in CQD surface. Li et al. prepared Mg–N co-doped CQDs and employed the prepared CQDs for the fluorescence-based detection of Hg^{2+} and cysteine.[56] Here, magnesium hydroxide, citric acid and ethylenediamine were used as precursors. The resultant CQDs had an average size of 5.2 nm and possessed a high PLQY (58.8%). Moreover, the HRTEM micrographs showed that some crystalline regions existed on the surface of the Mg-N co-doped CQDs, which is responsible for the bright PL emissions. In addition, to widen the application possibilities of CQDs, single-metal atoms such as Cu, silicon, Zn, Ge and Tb can be used as dopants. However, the associated increase in toxicity of metal doped CQDs limits their widespread use, and this concern is expected to minimize the impact of future work in this direction. But the high biocompatibility of multiple non-metal atom doped CQDs supports the photoluminescence enhancement and selective sensing capability of CQDs so as to be implied as multifunctional nanomaterials.

1.3 Fluorescence property of doped CQDs.

The PL mechanism of CQDs is beneficial for tuning their fluorescence properties that can explore their application in field of bioimaging and biosensing. Therefore, tremendous efforts have been integrated to investigate the PL mechanism of CQDs. Moreover, numerous reports have considered CQDs as efficient fluorescent probes for cellular imaging, real-time molecular tracking in both in vitro and in vivo imaging. Studies indicated that several factors such as quantum size effect, low cytotoxicity, surface state, molecule state and carbon-core state, good photostability, surface passivation/ functionalization and conjugate effect substantially influence PL properties of CQDs.

Parallel to pristine CQDs, doped CQDs have drawn widespread attention because of their exceptional PL properties and diverse applications which were not availed by pristine

CQDs. Thus, understanding of the PL mechanisms of doped CQDs is of research importance. Recently several dedicated efforts led to a better understanding of this critical aspect about heteroatom-doped CQDs. Further to explore the PL processes in OCQDs, NCQDs, and NSCQDs, a model was developed and reported by Yu and co-workers. [57] Here, they highlighted N-CQDs as a new class of CQDs with more electrons being trapped by the newly formed surface states (N state). Thus, supporting the fact that enhanced trapping can facilitate and improve radiative recombination. Therefore, NCQDs exhibit higher PLQY and broader excitation dependent emission spectra when compared to OCQDs. Similarly, NSCQDs based studies the proposed mechanism states that the introduction of S atoms results in an increase in the density of N state, cooperative effect and a corresponding decrease in the density of O state. [58-61] The increased density of N state as explained in above mentioned results further increases the radiative recombination supporting NSCQDs to exhibit a higher PLQY and broader excitation-independent emission compared to NCQDs.

Xu et al. proposed a comprehensive spectroscopic evaluation and a complementary theoretical study to study the PL mechanism of NSCQDs.[62] Interestingly, it was found that the enhanced PLQY and luminescence of NSCQDs was due to the heteroatom directed, oxidized carbon-based surface passivation. Crosslinking enhanced emission (CEE) effect is another important mechanism that benefits in understanding the increase in PL properties in polymer dots (PolyDs). CEE effect for PL mechanism in PloyDs was established by findings of Yang and coworkers. [63] The study shows that raise in PL properties of potential fluorescent centres (fluorophores) was resulted by CEE effect. In case of polyethylenimine associated CQDs, the excited electrons were mainly dropped to the ground state through a non-radiative process whereas in PolyDs the vibration and rotation of the amine-based fluorophores were restricted and resulted in an increase in the percentage of the radiative process by the CEE effect. Precisely, energy traps and the conjugated electronic structure are the main reason for enhanced PL properties in heteroatom-doped CQDs, including single and co-doped systems. Additionally, the surface passivation induced by heteroatoms modulates as an excitation energy trap, which increases the photoluminescence of CQDs.

1.4 Bio-application of doped CQDs.

CQD have proven itself to be an outstanding carbon material for application in the fields of bio-imaging, bio-sensing, theranostics and photodynamic therapy. The biological

applications of CQDs in these four important areas will favourably influence the future of diagnostics and therapy.

Biosensing

In current decade, the detection of various targets such as ions, small molecules and biomacromolecules using the biosensing property of CQDs has been extensively explored. CQDs provide an improved ultrasensitive sensitivity and selectivity in field of detection due to high PLQY, ease of surface modification, low toxicity, resistance to photobleaching and excellent water solubility. The fluorescence property of CQDs is implied to detect biologically important ions, both in cellular and environmental levels. Mercury ions (Hg^{2+}) are one of the most toxic heavy metal ions and serious threaten to environment and human health. Mercury ions exhibit strong toxicity and bioaccumulation, which leads to various diseases such as hyperspasmia, expiratory dyspnoea, renal failure etc. Zhang et al[64] reported NCQDs for selective and sensitive sensing of Hg^{2+} in the aqueous phase based on fluorescence quenching mechanism. The probe shows a limit of detection (LOD) of 0.23 mM within a linear range of 0 to 25 mM. On the other hand, Zhang et al. reported a "turn-on" fluorescence nanosensor for Hg^{2+} sensing.[65] Interestingly, its paper based naked eye detectable sensor with an extremely low LOD of 4 ppb. Our group too reported a highly selective sensor for Hg^{2+} ions based on its affinity towards sulphur. [61]NSCQDs were synthesized hydrothermally and implied for sensing Hg^{2+} ions in water and living cells with a LOD of 0.05 nM. Likewise for detection of Cu2+ ions, Jiang's group reported a cyclam-functionalized CQD sensor exhibiting (cyclam: 1,4,8,11-tetraazacyclotetradecane) high selectivity and sensitivity detection of Cu^{2+} by fluorescence resonance energy transfer (FRET) between the cyclam–Cu^{2+} complex and CQDs. [66] Wu et al. also proposed a type of NCQDs obtained using prawn shells as precursors, as a probe for Cu^{2+} with a LOD of 5 nM. [67] Pan et al. prepared CQDs exhibiting unusually analogous fluorescence intensity as shifting the excitation wavelength, and formulated a multidimensional sensing platform for the detection of multiple metal ions based on quenching mechanism of metal ions to the CQDs at three emission maxima. [68] Nie's group synthesized N-doped CQDs through a simple and green route and employed the prepared N-doped CQDs for the sensitive monitoring of histidine levels (detection limit of 150 nM) under the optimal conditions. [69] CQDs assembled gold nanoparticles (AuNPs) resulting in the detection of cysteine (Cys) in human serum was reported by Zhang and coworkers. [70] It was found to show a detection

limit of 4 nM in cellular environment. Qu's group designed a heterogeneous nanocomplex (CQDs–AuNCs) to sense excessive reactive oxygen species (ROS) in living cells with high contrast. [71] Similarily, CQD-based nanosensors were also implied for detection of a variety of molecular targets including methylparathion, phosphate, dipicolinic acid, sialyl Lewis[a] etc., proving their versatility in bioactive molecules.[72-74,55]A inner filter effect (IFE) based N-doped CQDs and p-nitrophenylphosphate co-system was developed by Wu et al. to sense alkaline phosphatase (ALP).[75] Xu et al. reported a sandwich system of aptamer-modified CQDs and aptamer-functionalized silica nanoparticle for sensing thrombin. The specificity of nanoprobe towards thrombin exhibited a LOD of 1 nM. [76]

Bioimaging

At present, CQDs are more promising contenders for bioimaging due to their unique combination of excellent water solubility, low toxicity, resistance to photobleaching, and intense luminescence with high quantum yield. In the past decade, numerous attempts utilizing CQDs for the non-specific or specific cellular imaging have been studied. CQDs show great potential as novel fluorescence tags for cellular imaging and in vivo imaging. In 2006, Sun et al. were the first to report fluorescence bioimaging capability of CQDs in E. coli ATCC 25922 cells. [77] Jiang et al. reported the preparation of three RGB CQDs from three different phenylenediamine isomers (oPD, mPD and pPD) and implied it in imaging MCF-7 cells. [78] Likewise, doped CQDs were developed from lychee seeds which were successfully applied for the fluorescence imaging of HepG2 cells. [79] Additionally, various doped CQDs with non-specific cellular affinity have been implied for imaging of various cell lines including HeLa cell, human lung cancer (A549), NIH-3T3 fibroblast cells and fungus. [80-83]

Ge et al. reported that red-emissive SCQDs with broad absorption in the region from 400 to 750 nm, prepared from polythiophenephenylpropionic acid, have excellent fluorescence imaging capability under the visible light excitation (350–600 nm) and photoacoustic imaging under the NIR irradiation (671 nm) in mice models.[84] For the targeted in vivo imaging purposes, specific ligands need to be anchored on the surface of CQDs. Chen et al. reported a novel, size-controlled synthesis of gadolinium doped CQDs for cancer cell targeting ability and observed through in vitro cellular imaging with appreciable results in T1-weighted MRI images.[85]

Theranostics

The integration of doped CQDs in pharmaceutical field has resulted in active developments in the diagnostic and therapy of tumors, termed as *theranostics of tumors*. Recent advancements in functional CQDs offered to improve the ability of imaging and drug delivery. Surface functionalized CQDs could target specific tumors either through the enhanced permeability and retention effect via microvasculature or by the specific binding with biomarkers. Feng et al reported NCQD conjugated cisplatin for imaging-guided drug delivery with enhanced in vivo cancer therapy.[86] The anionic polymer with dimethylmaleic acid moieties (PEG-(PAH/DMMA)) formed a complex with CQDs-Pt(IV) through electrostatic interactions. In a mildly acidic tumor extracellular microenvironment, PEG-(PAH/DMMA) could undergo charge conversion and lead to a high-affinity adsorption of CQDs-Pt(IV) to cancer cell membranes. A facile and green protocol for synthesizing DNA-CQD hybrids using genomic DNA isolated from E. coli. was reported by Chen's group. [87] In this system, DNA can serve as a vehicle to deliver drugs into organelles and cells. Gopinath et al. synthesized CQDs@EPI-G5-Ac85 hybrids and its application in tumour treatment. [88] Mohapatra et al. recently reported a BNSCQD based pH responsive theranostic drug delivery system for theranostic application in treating hepatic cancer. [89]

Photodynamic therapy

The first photodynamic therapy (PDT) agent named Photofrins was approved for clinical use in 1993. Since then, there has been a tremendous research in the use of PDT as a therapeutic treatment. Recently, CQDs have been reported for their excellent applicability in PDT for cancer treatment. Wang et al. developed a NSCQD-porphyrin conjugated system for treating HeLa cells. [90] The system followed a FRET initiated superoxide generation under excitation of 700 nm to exhibit two-photon photodynamic cancer therapy. Yang et al. synthesized magnesium and nitrogen co-doped CQD for treating HepG2 cells using PDT. Here, the doped CQD showed a PLQY of 84% and generated singlet oxygen on excitation with 660 nm laser. [91] Simultaneously, Zheng et al. prepared C3N4 doped NCQDs for enhanced photodynamic therapy against hypoxic tumor via water splitting.[92] The therapy was studied in vivo in mice models using a 630 nm He-Ne laser. Recently, Guo et al. engineered a copper and nitrogen co-doped CQD and studied its

photodynamic efficiency in both invitro and invivo models. The cell viability was found to reduce to 20% upon PDT (808 nm laser).[93]

1.5 Current state-of-the-art

The heteroatom doping strategy has great potential to tune the PL properties and open up large opportunities for various applications especially in the biomedical field. In spite of significant work in the field of doped CQD synthesis, still a large amount of precursor is needed to produce few milligrams of doped CQD with desired level of doping and excellent PLQY. These precursors are toxic organic compounds hence result in environmental hazards. So at present more importance is given to develop synthesis process which involves moderate reaction condition and improved product yield. One of the most controversial fundamental issues of CQDs is the PL mechanism. Further experimental verification and theoretical calculations are truly desired to provide a coherent picture. CQDs with a high QY comparable to traditional semiconductor QDs at longer wavelengths beyond the blue light region are yet to be synthesized on a large-scale through facile methods. More emphasis is given on carbon dots with bright fluorescence emissions emphasized in the red/near-IR spectral regions, thus more effective in tissue penetration, is desired. Also studies are under continuous progress on the exploitation of the surface functionalization in carbon dots for controlled coupling with bioactive species to enable specific targeting in cellular and in vivo imaging and related biomedical applications. For optical imaging of cells, carbon dots enter into cells mainly through passive endocytosis and label the perinuclear cytoplasm predominantly. For better accumulation of carbon dots in the cell, it is advisable to couple membrane translocation agents; and for specific labelling of organelles, ligands with targeting capability should be employed. In the field of cancer theranostics, the potentiality of CDs-based nanoprobes as a platform for dual- or multi-modal bioimaging agents including magnetic resonance imaging or photoacoustic imaging need to be further explored. New cancer therapies that combine CDs, with therapeutic agents such as PDT, PTT agents or anticancer agents are expected to receive growing efforts, which will lead to a greatly improved curative effect on tumor. Currently, pharmaceutical industries are extensively working on development of sustainable release nanoformulations due to its intrinsic benefits. The basic idea of sustained release is a promising way to decrease the side effects of molecular drugs by avoiding the fluctuation of concentration of the drug in human body and raise patient compliance by reducing frequency of dosage. Therefore, the use of nanoparticles to

encapsulate or conjugate anticancer drugs can improve targeted delivery, and enable towards betterment of therapeutic outcomes. So exclusively, there will be variation in release kinetics of drugs loaded in a gated and non-gated system. The stimuli responsive gated systems attribute for controlled release of various drugs at targeted site. In this regard smarter supramolecular nanomachines can be designed by integrating CQD with other matrix to finely control the drug release kinetics and/or to achieve multiple advantages such as control release, imaging and PDT/PTT on a single platform.

The main focus of this research work is to develop new fabrication methods for doped fluorescent carbon quantum dots for sensing biologically active molecules and ions. We aim to optimize the PL properties of the doped CQD with respect to precursor concentration. Utilising the improved emission properties of doped CQD we further want to construct smart theranostics nanoparticle for cancer treatment. To derive our aim we emphasis on the following issues, 1) Low temperature cost effective approach towards synthesis of doped carbon dots, 2) Introduction of abundant surface functional groups on the surface of CQD so as to ensure a better molecular recognition of the target analyte suitable targeted stimuli responsive release of therapeutic agent at cancer site, 3) Construction of suitable cancer nanotheranostics by integrating doped CQD with other matrices. We hypothesize that due to hetero atom doping as well as abundant surface functional groups, carbon quantum dots would show better light harvesting property along with rapid and selective molecular recognition which will open up new opportunities in in bioimaging and cancer theranostics. Hollow carbon nanospheres embedded with doped carbon quantum dots would not only safeguard a wide range of hydrophic anticancer drugs but also act as a fluorescence imaging probe against tuneable excitation wavelengths.

1.6 Objectives

The present research is aimed towards development of suitable synthetic approach to improve existing technologies for large scale production of carbon quantum dot based sensors and application in sensing of biomolecules and drug delivery. Our research objective is set as follows;

- To develop an easy and cost effective synthetic technique for large scale production of doped carbon quantum dot
- To investigate the effect of heteroatom doping on PL properties

- To explore the suitability of the developed doped CQD in sensing, bioimaging with a clearcut mechanism of molecular recognition
- To design a nanosystem with multiple imaging modalities to carry cancer drugs and regulate their stimuli responsive release mechanism while keeping their overall integrity unaffected
- To investigate the luminescence properties of carbon nanostructures when used in theranostic application
- To study the efficiency of the synthesized drug loading particles in vitro in model cancer cells

In relevance to this approach, a boron, nitrogen and sulphur doped carbon quantum dot has been developed for sensing glucosamine, cancer marker sialyl Lewis[a] and fluoride in cellular environment. Carbon quantum dot gated magnetic mesoporous silica nanoparticles have been developed for targeted and controlled delivery of 5-fluorouracil. Mesoporous hollow carbon nanospheres have been developed for light responsive delivery of anticancer drug gemcitabine and the overall performance in vitro has been evaluated.

1.7 References

1. X. Xu, R. Ray, Y. Gu, H. J. Ploehn, L. Gearheart, K. Raker and W. A. Scrivens, *J. Am. Chem. Soc.*, 2004, **126**, 12736-12737.
2. A. Loukanov, R. Sekiya, M. Yoshikawa, N. Kobayashi, Y. Moriyasu and S. Nakabayashi, *J. Phys. Chem. C*, 2016, **120**, 15867-15874.
3. H. Chen, Z. Wang, S. Zong, P. Chen, D. Zhu, L. Wu and Y. Cui, *Nanoscale*, 2015, **7**, 15477-15486.
4. O. S. Wolfbeis, *Chem. Soc. Rev.*, 2015, **44**, 4743-4768.
5. Y. Wang and A. Hu, *J. Mater. Chem. C*, 2014, **2**, 6921-6939.
6. H. Wang, J. Yi, D. Velado, Y. Yu and Shuiqin Zhou, *ACS Appl. Mater. Interfaces*, 2015, **7**, 15735-15745.
7. Y. Du and S. Guo, *Nanoscale*, 2016, **8**, 2532-2543.
8. S. Y. Lim, W. Shen and Z. Gao, *Chem. Soc. Rev.*, 2015, **44**, 362-381.
9. X. T. Zheng, A.rundithi Ananthanarayanan, K. Q. Luo and P. Chen, *Small*, 2015, **11**, 1620-1636.
10. J. Zhou, H. Zhou, J. Tang, S. Deng, F. Yan, W. Li and M. Qu, *Microchimica Acta*, 2017, **184**, 343-368.

11. K. A. S. Fernando, S. Sahu, Y. Liu, W. K. Lewis, E. A. Guliants, A. Jafariyan, P. Wang, C. E. Bunker and Y. P. Sun, *ACS Appl. Mater. Interfaces*, 2015, **7**, 8363-8376.
12. D. Tang, J. Liu, X. Wu, R. Liu, X. Han, Y. Han, H. Huang, Y. Liu and Z. Kang, *ACS Appl. Mater. Interfaces*, 2014, **6**, 7918-7925.
13. Y. Qiu, B. Zhou, X. Yang, D. Long, Y. Hao and P. Yang, *ACS Appl. Mater. Interfaces*, 2017, **9**, 16848-16856.
14. M. Zheng, S. Ruan, S. Liu, T. Sun, D. Qu, H. Zhao, Z. Xie, H. Gao, X. Jing and Z. Sun, *ACS Nano*, 2015, **9**, 11455-11461.
15. H. J. Jian, R. S. Wu, T. Y. Lin, Y. J. Li, H. J. Lin, S. G. Harroun, J. Y. Lai and C. C. Huang, *ACS Nano*, 2017, **11**, 6703-6716.
16. Z. Peng, X. Han, S. Li, A. O. A. Youbi, A. S. Bashammakh, M. S. E. Shahawi and R. M. Leblanc, *Coordination Chemistry Reviews*, 2017, **343**, 256-277.
17. Q. Xu, T. Kuang, Y. Liu, L. Cai, X. Peng, T. S. Sreeprasad, P. Zhao, Z. Yu and N. Li, *J. Mater. Chem. B*, 2016, **4**, 7204-7219.
18. P. Namdari, B. Negahdari and A. Eatemadi, *Biomed. Pharm.*, 2017, **87**, 209-222.
19. A. Zhao, Z. Chen, C. Zhao, N. Gao, J. Ren and X. Qu, *Carbon*, 2015, **85**, 309-327.
20. Y. Li, Y. Zhao, H. H. Cheng, Y. Hu, G. Q. Shi, L. M. Dai and L. T. Qu, *J. Am. Chem. Soc.*, 2012, **134**, 15-18.
21. Q. Xu, P. Pu, J. Zhao, C. Dong, C. Gao, Y. Chen, J. Chen, Y. Liu and H. Zhou, *J. Mater. Chem. A*, 2015, **3**, 542-546.
22. Z. Qian, X. Shan, L. Chai, J. Ma, J. Chen and H. Feng, *ACS Appl. Mater. Interfaces*, 2014, **6**, 6797-6805.
23. M. K. Barman, B. Jana, S. Bhattacharyya and A. Patra, *J. Phys. Chem. C*, 2014, **118**, 20034-20041.
24. J. Zhou, X. Shan, J. Ma, Y. Gu, Z. Qian, J. Chen and H. Feng, *RSC Adv.*, 2014, **4**, 5465-5468.
25. W. T. Wu, L. Y. Zhan, W. Y. Fan, J. Z. Song, X. M. Li, Z. T. Li, R. Q. Wang, J. Q. Zhang, J. T. Zheng, M. B. Wu and H. B. Zeng, *Angew. Chem.*, 2015, **54**, 6540-6544.
26. Y. P. Sun, X.Wang, F. S. Lu, L.Cao,M. J.Meziani, P. J.G. Luo, L. R. Gu and L. M. Veca, *J. Phys. Chem. C*, 2008, **112**, 18295-18298.
27. Z. Li, H. Yu, T. Bian, Y. Zhao, C. Zhou, L. Shang, Y. Liu, L. Z. Wu, C. H. Tung and T. Zhang, *J. Mater. Chem. C*, 2015, **3**, 1922-1928.
28. Z. Qian, J. Ma, X. Shan, H. Feng, L. Shao and J. Chen, *Chem. Eur. J.* 2014, **20**, 2254-2263.

29. D. Chen, W. Wu, Y. Yuan, Y. Zhou, Z. Wan and P. Huang, *J. Mater. Chem. C*, 2016, **4**, 9027-9035.
30. J. Tan, R. Zou, J. Zhang, W. Li, L. Zhang and D. Yue, *Nanoscale*, 2016, **8**, 4742-4747.
31. J. Ci, Y. Tian, S. Kuga, Z. Niu, M. Wu and Y. Huang, *Chem. Asian J.* 2017, **12**, 2916-2921.
32. G. Yang, X. Wan, Y. Su, X. Zeng and J. Tang, *J. Mater. Chem. A*, 2016, **4**, 12841-12849.
33. A. Gupta, N. C. Verma, S. Khan and C. K. Nandi, *Biosens. Bioelectron*., 2016, **81**, 465-472.
34. H. Yang, F. Li, C. Zou, Q. Huang and D. Chen, *Microchim Acta*, 2017, **184**, 2055-2062.
35. P. Shen and Y. Xia, *Anal. Chem*., 2014, **86**, 5323-5329.
36. X. Shan, L. Chai, J. Ma, Z. Qian, J. Chen and H. Feng, *Analyst*, 2014, **139**, 2322-2325.
37. H. K. Sadhanala and K. K. Nanda, *Carbon*, 2016, **96**, 166-173.
38. J. Zhou, X. Shan, J. Ma, Y. Gu, Z. Qian, J. Chen and H. Feng, *RSC Adv*., 2014, **4**, 5465-5468.
39. F. Yang, X. He, C. Wang, Y. Cao, Y. Li, L. Yan, M. Liu, M. Lv, Y. Yang, X. Zhao and Y. Li, *Applied Surface Science*, 2018, **448**, 589-598.
40. G. Gao, Y. W. Jiang, H. R. Jia, J. Yang and F. G. Wu, *Carbon*, 2018, **134**, 232-243.
41. Y. Han, D. Tang, Y. Yang, C. Li, W. Kong, H. Huang, Y. Liu and Z. Kang, *Nanoscale*, 2015, **7**, 5955-5962.
42. H. Li, C. Sun, R. Vijayaraghavan, F. Zhou, X. Zhang and D. R. MacFarlane, *Carbon*, 2016, **104**, 33-39.
43. Z. Song, F. Quan, Y. Xu, M. Liu, L. Cui and J. Liu, *Carbon*, 2016, **104**, 169-178.
44. Y. Su, M. Zhang, N. Zhou, M. Shao, C. Chi, P. Yuan and C. Zhao, *Microchim Acta*, 2017, **184**, 699-706.
45. X. Gong, Y. Liu, Z. Yang, S. Shuang, Z. Zhang and C. Dong, *Analytica Chimica Acta*, 2017, **968**, 85-96.
46. Y. Qiao, D. Luo, M. Yu, T. Zhang, X. Cao, Y. Zhou and Y. Liu, *Chem. Eur. J*., 2018, **24**, 2257-2263.
47. Q. Xu, B. Li, Y. Ye, W. Cai, W. Li, C. Yang, Y. Chen, M. Xu, N. Li, X. Zheng, J. Street, Y. Luo and L. Cai, *Nano Research*, 2018, **11**, 3691-3701.

48. Y. Yang, D. Huo, H. Wu, X. Wang, J. Yang, M. Bian, Y. Mab and C. Hou, *Sensors & Actuators: B. Chemical*, 2018, **274**, 296-303.
49. Y. Guo, Y. Chen, F. Cao, L. Wang, Z. Wang and Y. Leng, *RSC Adv*., 2017, **7**, 48386-48393.
50. Z. X. Liu, B. B. Chen, M. L. Liu, H. Y. Zou and C. Z. Huang, *Green Chem*., 2017, **19**, 1494-1498.
51. S. H. Chi, G. Gedda, W. M. Girma, J. K. Chen, Y. C. Ling, A. V. Ghule, K. L. Oue and J. Y. Chang, *Acta Biomaterialia*, 2016, **46**, 151-164.
52. Y. Pan, J. Yang, Y. Fang, J. Zheng, R. Song and C. Yi, *J. Mater. Chem. B*, 2017, **5**, 92-101.
53. X.Y. Ren, X.X. Yuan, Y.P. Wang, C.L. Liu, Y. Qin, L.P. Guo and L.H. Liu, *Optical Materials*, 2016, **57**, 56-62.
54. M. Zhang, W. Wang, P. Yuan, C.Chi, J. Zhang and N. Zhou, *Chemical Engineering Journal*, 2017, **330**, 1137-1147.
55. R. K. Das and S. Mohapatra, *J. Mater. Chem. B*, 2017, **5**, 2190-2197.
56. T. Liu, N. Li, J. X. Dong, H. Q. Luo and Nian Bing Li, *Sensors and Actuators B*, 2016, **231**, 147-153.
57. Y. Dong, H. Pang, H. B. Yang, C. Guo, J. Shao, Y. Chi, C. M. Li and T. Yu, *Angew Chem Int Ed*, 2013, **52**, 7800-7804.
58. J. Liang, Y. Jiao, M. Jaroniec and S. Z. Qiao, *Angew. Chem. Int. Ed*., 2012, 51, 11496.
59. S. A. Wohlgemuth, R. J. White, M. G. Willinger, M. M. Titirici and M. Antonietti, *Green Chem*., 2012, **14**, 1515-1523.
60. C. H. Choi, M. W. Chung, S. H. Park and S. I. Woo, *Phys. Chem. Chem. Phys*., 2013, **15**, 1802-1805.
61. S. Mohapatra, S. Sahu, N. Sinha and S. K. Bhutia, *Analyst*, 2015,**140**, 1221-1228.
62. Q. Xu, Y. Liu, C. Gao, J. Wei, H. Zhou, Y. Chen, C. Dong, T. S. Sreeprasad, N. Li and Z. Xia, *J. Mater. Chem. C*, 2015, **3**, 9885-9893.
63. S. Zhu, L. Wang, N. Zhou, X. Zhao, Y. Song, S. Maharjan, J. Zhang, L. Lu, H. Wang and B. Yang, *Chem. Commun*., 2014, **50**, 13845-13848.
64. R. Z. Zhang and W. Chen, *Biosens. Bioelectron*., 2014, **55**, 83-90.
65. C. Yuan, B. H. Liu, F. Liu, M. Y. Han and Z. P. Zhang, *Anal. Chem*., 2014, **86**, 1123-1130.
66. J. Chen, Y. Li, K. Lv, W. Zhong, H. Wang, Z. Wu, P. Yi and J. Jiang, *Sens. Actuators, B*, 2016, **224**, 298-306.

67. G. Gedda, C. Y. Lee, Y. C. Lin and H. F. Wu, *Sens. Actuators,B*, 2016, **224**, 396-403.
68. L. Pan, S. Sun, A. Zhang, K. Jiang, L. Zhang, C. Dong, Q. Huang, A. Wu and H. Lin, *Adv. Mater*., 2015, **27**, 7782-7787.
69. X. Zhu, T. Zhao, Z. Nie, Z. Miao, Y. Liu and S. Yao, *Nanoscale*, 2016, **8**, 2205-2211.
70. J. Deng, Q. Lu, Y. Hou, M. Liu, H. Li, Y. Zhang and S. Yao, *Anal. Chem*., 2015, **87**, 2195-2203.
71. X. Wang, K. Qu, B. Xu, J. Ren and X. Qu, *J. Mater. Chem*., 2011, **21**, 2445-2450.
72. J. Hou, J. Dong, H. Zhu, X. Teng, S. Ai and M. Mang, *Biosens. Bioelectron*., 2015, **68**, 20-26.
73. H. Chen, Y. Xie, A. M. Kirillov, L. Liu, M. Yu, W. Liu and Y. Tang, *Chem. Commun.*, 2015, **51**, 5036-5039.
74. 129 H. X. Zhao, L. Q. Liu, Z. De Liu, Y. Wang, X. J. Zhao and C. Z. Huang, *Chem. Commun*., 2011, **47**, 2604-2606.
75. G. Li, H. Fu, X. Chen, P. Gong, G. Chen, L. Xia, H. Wang, J. You and Y. Wu, *Anal. Chem*., 2016, **88**, 2720-2726.
76. B. Xu, C. Zhao, W. Wei, J. Ren, D. Miyoshi, N. Sugimoto and X. Qu, *Analyst*, 2012, **137**, 5483-5486.
77. Y.P. Sun, B. Zhou, Y. Lin, W. Wang, K. A. S. Fernando, P. Pathak, M. J. Meziani, B. A. Harruff, X. Wang, H. Wang, P. G. Luo, H. Yang, M. E. Kose, B. Chen, L. M. Veca and S.Y. Xie, *J. Am. Chem. Soc*., 2006, **128**, 7756-7757.
78. K. Jiang, S. Sun, L. Zhang, Y. Lu, A. Wu, C. Cai and H. Lin, *Angew. Chem., Int. Ed. Engl*., 2015, **54**, 5360-5363.
79. M. Xue, M. Zou, J. Zhao, Z. Zhan and S. Zhao, *J. Mater.Chem. B*, 2015, 3, 6783.
80. Y. Dong, H. Pang, H. B. Yang, C. Guo, J. Shao, Y. Chi, C.M. Li and T. Yu, *Angew. Chem., Int. Ed. Engl*., 2013, **52**, 7800-7804.
81. Z. L. Wu, P. Zhang, M. X. Gao, C. F. Liu, W. Wang, F. Leng and C. Z. Huang, *J. Mater. Chem. B*, 2013, **1**, 2868-2873.
82. R. Purbia and S. Paria, *Biosens. Bioelectron*., 2016, **79**, 467-475.
83. X. Zhang, S. Wang, C. Zhu, M. Liu, Y. Ji, L. Feng, L. Tao and Y. Wei, *J. Colloid Interface Sci*., 2013, **397**, 39-44.
84. J. Ge, Q. Jia, W. Liu, L. Guo, Q. Liu, M. Lan, H. Zhang, X. Meng and P. Wang, *Adv. Mater*., 2015, **27**, 4169-4177.
85. H. Chen, G. D. Wang, X. Sun, T. Todd, F. Zhang, J. Xie and B. Shen, *Adv. Funct. Mater*., 2016, **26**, 3973-3982.

86. T. Feng, X. Ai, G. An, P. Yang and Y. Zhao, *ACS Nano*, 2016, **10**, 4410-4420.
87. Z.C. Yang, M. Wang, A. M. Yong, S. Y. Wong, X.-H. Zhang, H. Tan, A. Y. Chang, X. Li and J. Wang, *Chem. Commun*., 2011, **47**, 11615-11617.
88. I. Matai, A. Sachdev and P. Gopinath, *ACS Appl. Mater. Interfaces*, 2015, **7**, 11423-11435.
89. R. K. Das, A. Pramanik, M. Majhi and S. Mohapatra, *Langmuir*, 2018, **34**, 5253-5262.
90. J. Wang, Z. Zhang, S. Zha, Y. Zhu, P. Wu, B. Ehrenberg and J. Y. *Chen, Biomaterials*, 2014, **35**, 9372-9381.
91. K. Yang, F. Li, W. Che, X. Hu, C. Liu and F. Tian, *RSC Adv.*, 2016, **6**, 101447-101451.
92. D. W. Zheng, B. Li, C. X. Li, J. X. Fan, Q. Lei, C. Li, Z. Xu and X. Z. Zhang, *ACS Nano*, 2016, **10**, 8715-8722.
93. X. L. Guo, Z. Y. Ding, S. M. Deng, C. C. Wen, X. C. Shen, B. P. Jiang and H. Liang, *Carbon*, 2018, **134**, 519-530.

Chapter – 2

Highly luminescent, heteroatom-doped carbon quantum dots for ultrasensitive sensing of glucosamine and targeted imaging of liver cancer cells

2.1 Introduction

Fluorescence sensing has been emerging as an efficient detection method because of its high sensitivity and spatiotemporal resolution.[1-5] The effectiveness of boronic acid as a receptor in chemosensors for a wide range of biologically important species has been extensively reported. The reversible covalent interaction of boronic acid with cis 1,2 or 1,3 diols to form five or six membered cyclic esters, respectively, has proven to be sufficiently strong and enables the binding of saccharides at mM or sub μM levels.[6,7] Based on this binding principle, a number of fluorescence sensors have been designed for detecting sugars,8,9 aminosugars,[10,11] cell surface glycans,[12-14] etc. However, organic fluorescence sensors are expensive, involve a multistep synthesis process and are normally unworthy for practical promotion and application. By virtue of favorable optical properties and surface functionality, carbon nanomaterial-based sensing systems have been successfully applied for glucose sensing.[15] For instance, Qiu et al. have reported a fluorescence sensor constituting a combination of anionic graphene quantum dots and bipyridinum salts for detection of sugars and other saccharides.[16] This method offers a simple mix-and-detect protocol for rapid detection of glucose and other saccharides, but it lacks selectivity. Later, two different protocols were published where boronic acid functionalized carbon dot and graphene quantum dots have been used for selective sensing of glucose.[17,18] Although boronic acid is well-known to bind diol readily to act as a carbohydrate receptor, several boronic acid-based sensors failed to recognise D-glucosamine, other aminosugars, glycans, etc. due to their low selectivities.

On the other hand, glucosamine, an aminosugar, has been used over the years as a dietary supplement for the treatment of osteoarthritis in spite of its uncertain pharmacokinetics and pharmacodynamics.[19-21] In addition to its chondroprotective action, glucosamine has been believed to exert anticancer action for more than five decades. It shows growth inhibitory activity in cancer cells via affecting proteasomal activity.[22] There are also numerous contradictory findings on the efficiency of D-glucosamine in treating rheumatoid arthritis and gastric ulcers.[23-26] The development of luminescent quantum dot-based D-glucosamine sensors with a high sensitivity and selectivity will provide novel approaches for early clinical diagnosis of most D-glucosamine related diseases. Thus, it is of both biological and biomedical significance to construct sensing devices for probing D-glucosamine at normal cellular concentrations (1-2 mM). To date, very few fluorescence sensors have been reported for D-glucosamine, including monoaza-18-crown-6 ether and boronic acid as the

receptor units,[27] metal complexes,[28] graphene oxide, 8-aminoquinoline fluorophore[29] and the coumarin aldehyde system.[11] However, these fluorophores are associated with multiple shortcomings such as lack of selectivity, incompatibility in cellular environments and delayed response. As discussed in the previous section, boron doped graphene oxide/carbon quantum dots are emerging as a promising photoluminescence sensor for glucose and related biomolecules. Although boronic acid acts as recognition units for cis-diol, incorporation of boron in the graphitic network lowers luminescence behaviour due to presence of excess holes, which ultimately results in non-radiative decay. Furthermore, the excitonic band shows a blue shift after doping with boron, indicating that BGQD or BCQD based sensors can be operational only in the UV region, which limits their practical biological applications. It has been reported that compared to carbon quantum dots, N and S doped carbon dots show enhanced optical properties due to the introduction of new energy states, which trap electrons and, thus, are able to facilitate a high yield of radiative recombination.[30,31] Utilising the improved luminescence behaviour of electron-rich N-doped carbon dots, and chemical sensing of the boronic acid group towards cis-diol, a carbon quantum dot based sensing platform can be designed. Furthermore, generation of boronic acid along with nitrogen and sulphur on the quantum dot surface would increase the selectivity towards glucosamine.

In the present study, we have reported a boronic acid modified C-N-S quantum dot for selective and sensitive detection of glucosamine. It is proposed that due to the interaction of two cis-diol units and amine group with boronic acid and carbonyl groups, structurally rigid N-S doped carbon quantum dots are created, which restricts the intramolecular rotation of luminescence centres and enhances PL intensity. This protocol has been screened for the detection of analogous molecules such as glucose, dopamine, diethyl amine and sialyl Lewis^a. For the first time, a paper-strip sensor for naked eye detection of glucosamine is demonstrated. Furthermore, the synthesized BNSCQD has been explored for labelling liver cancer cells overexpressed with cell surface glycans, such as sialyl Lewis^a.

2.2 Experimental

Materials

D-Glucosamine, 3'-sialyl-Lewis^a tetrasaccharide, p-amino benzoic acid, dopamine, 3-aminophenylboronic acid monohydrate and deionized water were purchased from Sigma Aldrich. L-Aspartic acid and D-glucose was supplied by Finar chemicals. Diethyl amine and

citric acid were procured from Nice chemicals. Thiourea and absolute ethanol were purchased from Merck Ltd and Changshu Yangyuan chemicals, respectively.

Synthesis of boronic acid modified N,S co-doped carbon quantum dots (BNSCQD)

Citric acid (100 mg), thiourea (50 mg) and different amounts of 3-amino phenyl boronic acid (0.5 wt% (BNSCQD-1), 2 wt% (BNSCQD-2), 3 wt% (BNSCQD-3) and 5 wt% (BNSCQD-4)) were dissolved in a 30 mL mixture of deionized water:ethanol (2:1). Then, the transparent solution was transferred to a Teflon lined autoclave (Berghof, Germany) and heated at 180 °C for 6 h. After cooling, an orange solution was obtained, implying the formation of C-dots. The obtained dispersion was filtered through 0.22 μ filter paper to remove larger particles. The unreacted organic impurities were isolated from yellowish brown carbon dot solution by repeated washing with DCM, followed by centrifugation at 80,000 rpm. The obtained dispersion was dialysed against deionized water using a dialyzer with a molecular weight cut-off of 1000 Da for 24 h. Finally, the deep orange coloured aqueous solution containing BNSCQD was obtained. BNSCQD were recovered by lyophilisation.

Characterization

Photoluminescence spectra were collected on a Horiba FluoroMax-4 fluorimeter. Microstructural analysis and elemental mapping were done using a high resolution transmission electron microscope (FEI Technai G2 30ST) operated at 300 kV. The presence of surface functional groups was investigated using FTIR in an IRAffinity-1S, Shimadzu, spectrophotometer. Surface composition of BNSCQD was verified by XPS using an AlKa excitation source in a PHI 5000 Versa Prob II (FEI Inc.) instrument. The Raman spectrum of the as-prepared samples was recorded on a Renishaw invia Raman spectrometer (UK model). Particle size and mean zeta potential at different pH values were measured using a Nano ZS 90, Malvern instrument. Live-cell images were captured under a Leica TCS SP8 confocal microscope with laser excitations at 405, 488 and 546 nm.

Fluorescence sensing of glucosamine

Sensing of glucosamine was conducted in phosphate buffer saline (PBS). In a typical run, BNSCQD (15 mL, 3.3 mg mL^{-1}) was dispersed in PBS solution, followed by addition of different concentrations of the D-glucosamine molecule. PL spectra were recorded after an incubation period of 30 min at 37 °C. The sensitivity and selectivity for glucosamine was

confirmed by comparing other biomolecule stock solutions in a similar way at a concentration of 60 mM.

Paper-based sensor strip for the detection of glucosamine

First, cellulose based filter paper was cut into circles with a diameter of 3 mm and then immersed into an ethanol solution of BNSCQD (1 mg mL^{-1}). The paper strips were immersed in BNSCQD solution for 20 min, followed by air drying for 5 h. Each batch contained a set of eight circular filter papers. The papers were then air-dried and immobilized on the adhesive side of a cellotape. The exposed side of those strips was treated with aqueous solutions containing different concentrations of glucosamine. The change in fluorescence intensity was investigated using a digital camera and a fluorescence lamp. Furthermore, the LOD for paper-based glucosamine sensing under UV (340 nm) and visible (420 nm) light were analysed using ImageJ software.

Cytotoxicity

HepG2, PC 3, L929 and 3T3 cells were harvested and the cell concentration was adjusted to 3 x 10^3 cells per mL. Cells were plated in a 96 well flat bottom culture plate (180 mL per well) and incubated with various concentrations (0.5, 5, 10, 20, 50 mg mL^{-1}) of 20 mL of BNSCQD. All cultures were incubated for 72 h at 37 °C and 5% CO_2 in a humidified incubator. Viable cell concentration was checked by the MTT (3-(4,5-dimethyl-2- thiazolyl)-2,5-diphenyl-2H-tetrazolium bromide) assay.

Intracellular uptake and live cell imaging

All cell lines (3 x 10^4) cell lines were seeded into 24 well plates and incubated in 400 mL DMEM containing 10% FBS and 1% antibiotic (penicillin, streptomycin) at 37 °C inside the incubator with 5% CO_2. After 24 h of incubation, media were removed and replaced with fresh DMEM without serum containing BNSCQD at a concentration of 30 mg mL^{-1} for each type of cell. After incubation for 3 h, media was removed and washed three times with 1 x PBS. Thereafter, cells were fixed with 2% paraformaldehyde (PFA) for 15 min at RT, followed by washing with 1 x PBS and viewed under a confocal microscope (Leica TCS SP8) with excitation at 405, 488, and 546 nm.

2.3 Results and discussion

Bottom up synthesis from molecular precursors is a well-known approach for the synthesis of carbon quantum dots (Scheme 1). Although the exact reaction mechanism has not been clarified to date, previous research reports show that an optimised reaction time,[32,33] reaction temperature[34,35] and ratio of precursors are necessary to get heteroatom doped carbon quantum dots with the best fluorescence properties. In the earlier reports published from our laboratory, the reaction time and temperature have been optimised, suggesting that typically hydrothermal treatment of carbon, nitrogen and sulphur precursors at 180 °C for 6 h gives carbon dots with the highest FLQY.[25] Keeping the reaction time constant at 6 h, the effect of temperature and precursor ratio on luminescence quantum yield has been presented in Table 1. When the temperature of the reaction was varied between 160 °C and 240 °C, it was observed that quantum dots with highest QY were obtained at 180 °C. Optimising the precursor ratio it was observed that the maximum fluorescence intensity and quantum yield (28%) was obtained with a precursor ratio of citric acid : thiourea : m-aminophenyl boronic acid = 0.5 : 0.5 : 0.3 (Table 1),which is better than the FLQY of the boron doped carbon quantum dot reported earlier.[35]

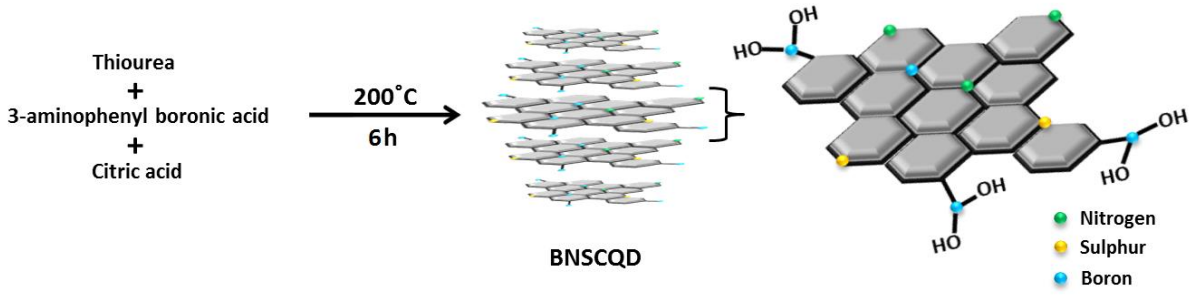

Scheme 1 One-step synthesis of boronic acid modified BNSCQD

Table 1 Quantum yield of various as-synthesized carbon quantum dots

CQDs	Quantum yield
BCQD	5.12
BNCQD	10.28
BNSCQD-1	4.64
BNSCQD-2	16.71
BNSCQD-3	28.39
BNSCQD-4	11.53
BNSCQD-3(160°C)	16.3
BNSCQD-3(180°C)	28.39
BNSCQD-3(200°C)	24.55
BNSCQD-3(220°C)	21.62
BNSCQD-3(240°C)	17.43

TEM and Raman study

The TEM image shows uniform BNSCQDs with diameters of 3-4.5 nm (Fig. 1). The size of B-doped NSCQDs is much smaller than that of the NSCD prepared using our previous method.[30] The high resolution TEM image shows a lattice spacing of 0.36 nm, which is in agreement with the basal plane of graphite. The STEM-EDAX (Fig. 2A) indicates that BNSCQDs are mainly composed of carbon, nitrogen, oxygen, sulphur and boron. The EDS mapping (Fig. 2B) shows that there is uniform distribution of N, S, and B throughout.

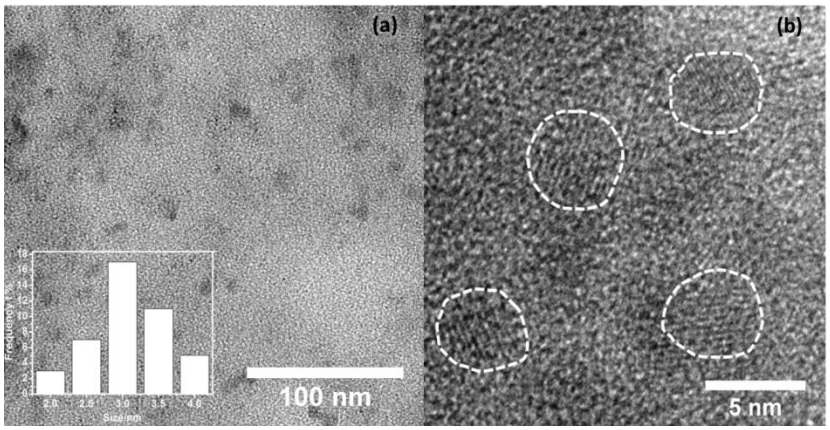

Fig. 1 (a) TEM image of BNSCQD; inset: the particle size distribution, (b) high-resolution TEM image

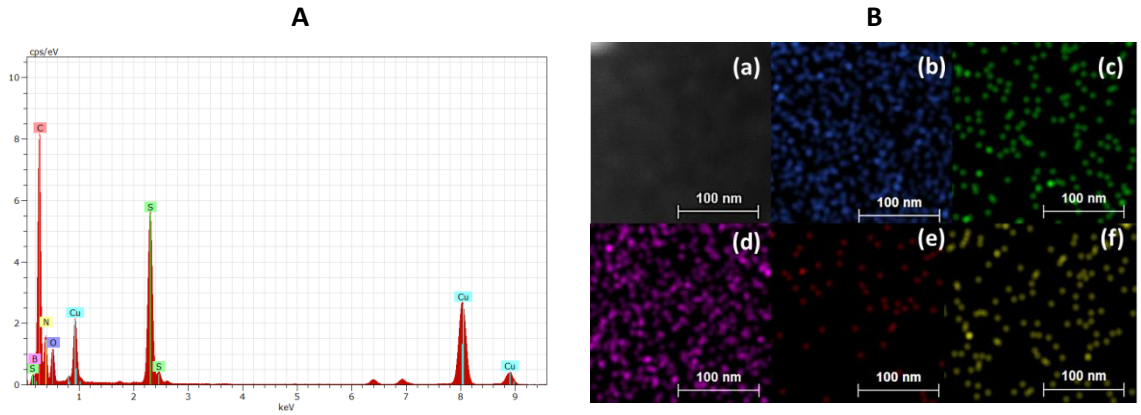

Fig. 2 (A) SEM-EDAX spectrum of BNSCQD-3, (B) (a) STEM image, elemental mapping showing the presence of (b) carbon, (c) nitrogen, (d) sulphur, (e) boron, (f) oxygen in BNSCQD

Raman and FTIR study

Fig. 3A shows the Raman spectra, where well-defined D peak (~ 1346 cm^{-1}) and G peak (~ 1589 cm^{-1}) are common peaks for each BNSCQD matrix. It was found that with an increase in boron content from 0.5 wt% to 3 wt%, the I_D/I_G ratio increased from 0.61 to 0.87. This suggests heterogeneous boron doping in the hexagonal symmetry of graphene alignment of CQD. The presence of various surface functional groups in assynthesized CQDs was also verified by FTIR spectra. The FTIR spectrum (Fig. 3B) of BNSCQD exhibits peaks at 1393,

1186, 1082 and 1040 cm^{-1}, which are attributed to B–O stretching, B–O–H bending, C–B stretching and B–O–H deformation.

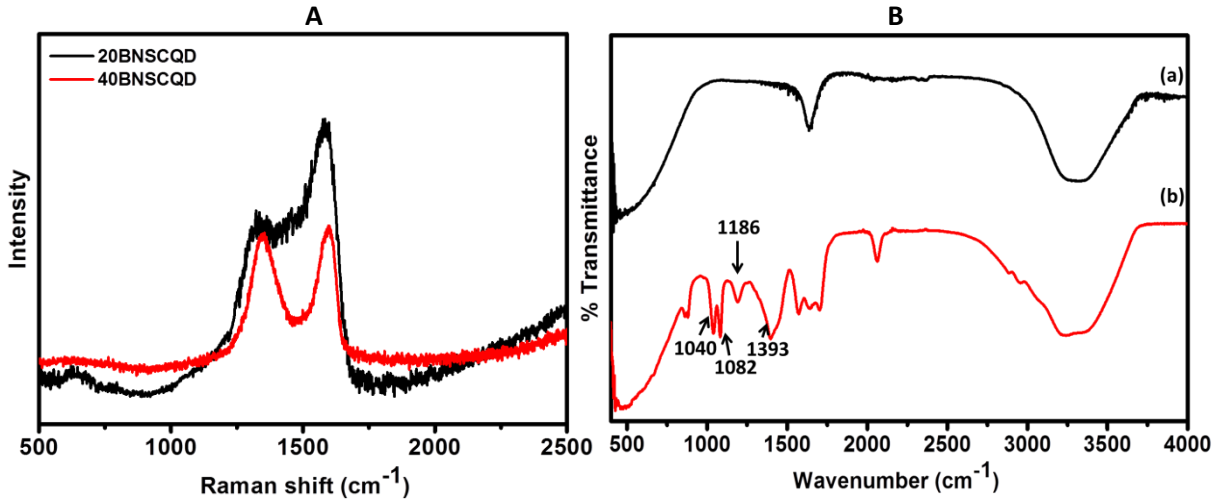

Fig. 3 (A) Raman spectra of BNSCQD with different boron content and (B) FTIR spectra of (a) 3-phenylboronic acid, (b) BNSCQD

XPS study

XPS gives further insight into the presence of surface functional groups in BNSCQD. Fig. 4a presents the XPS survey spectrum of BNSCQD having peaks at 160–170, 188–193, 284–292, 398–406, and 534 eV, which correspond to the binding energies of B1s, S2p, C1s, N1s, and O1s with their atomic percentages 2.86, 4.41, 33.32, 16.66 and 61.67, respectively. The high resolution scan C1s region (Fig. 4b) shows carbons present in five different environments, corresponding to C–B at 283.8 eV, sp^2 carbon in graphene at 284.2 eV, sp^3 C (C–S, C–N and C–O) at 285.8 eV, C=O at 287.8 eV and C–O/C–N at 286.3 eV. In Fig. 4c, B1s core-level peaks appear at 189.4, 190.2, 190.5 and 191.3 eV, which are assigned to the BC_3, BC_2O, B–N and BCO_2 bonds, respectively.[18] Deconvolution of the B1s region indicates that a lower fraction of boron has been incorporated in the carbon quantum dot skeleton, whereas a larger fraction of boron atoms are present on the surface in the form of boronic acid. The high resolution scans of the S2p region (Fig. 4e) can be fitted to three peaks at 162.9, 164.1 and 168.8 eV representing the $S2p_{3/2}$, $S2p_{1/2}$ of the C–S–C covalent bond and oxidized sulphur S=O bonding. The high resolution scan at the N1s region (Fig. 4d) can be fitted into four peaks at 398.2, 399.4 and 400.1 eV indicating the presence of pyridinic, N–H as well as pyrrolic nitrogen in the prepared CQDs. FTIR and XPS analyses indicate that boronic acid groups are intact on the surface of the BNSCQD even after hydrothermal carbonization. In addition to this, the presence of –COOH, CQO and phenolic C–OH groups on the surface of BNSCQD imparts excellent water solubility to the doped C-dot; at the same time, the

presence of surface boronic acids and –NH groups offers a possibility for interactions with glucosamine and similar biomolecules.

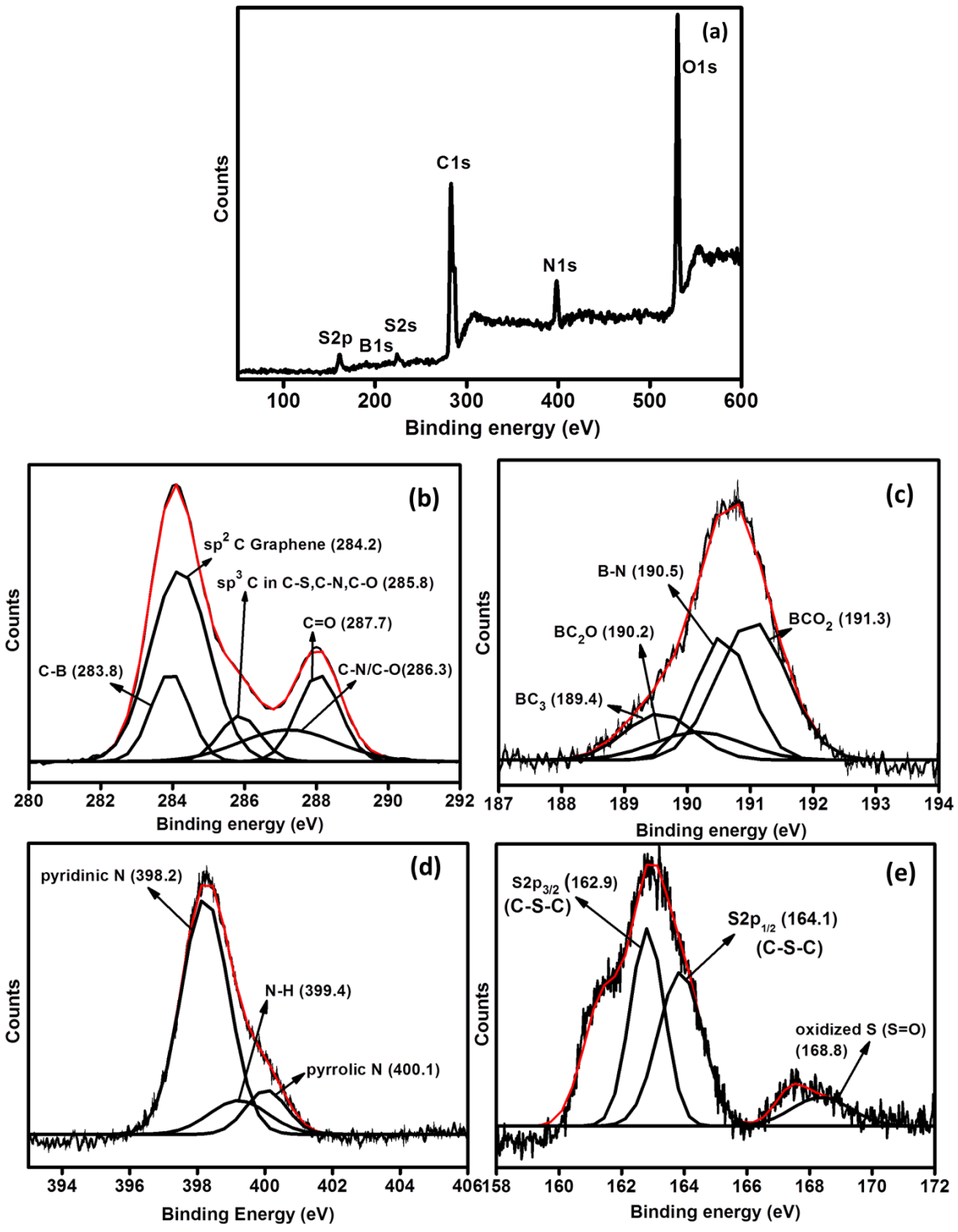

Fig. 4 (a) XPS survey spectrum of BNSCQD-3, high resolution scans of (b) C1s, (c) B1s, (d) N1s and (e) S2p

Photoluminescence property of BNSCQD

To analyse the enhanced luminescence properties of BNSCQD, the excitation and emission properties of BCQD, BNCQD and BNSCQD have been compared (Fig. 5). The excitation spectrum of BNSCQD shows three bands positioned at 260, 320 and 440 nm. The first two bands correspond to π–π* and n–π* transitions from aromatic sp^2 domains and nonbonding orbitals, respectively, while the other transition centred at 440 nm is due to trapping of excited state energy by surface states, which results in a strong emission. From the luminescence spectra collected over a wide excitation range from 240 to 470 nm, it is interesting to note that when the excitation wavelength is varied between 240–280 nm (π–π*) and 310–330 nm (n–π*), there is only a change in intensity of the peak but no shift in peak position occurs (Fig. 6). However, when the excitation is varied from 330 to 560 nm, there is a regular trend in λ_{em} indicating excitation dependent emission. The enhanced fluorescence properties of BNSCQD compared to BCQD are due to incorporation of N and S and in accordance with the result reported by Yu et al.[36] The nitrogen doping introduces new types of surface states, which are able to facilitate a high yield of radiative recombination. The presence of sulphur enhances the effect of nitrogen atoms in doped CD through a cooperative effect. Unlike previously reported BCQDs, where the excitation dependent emission has been observed over the UV region only, in our case, BNSCQD shows multicolour emission under excitation in the visible range. Such a unique property of the BNSCQD fluorescent probe offers several visible advantages in sensing and bioimaging.

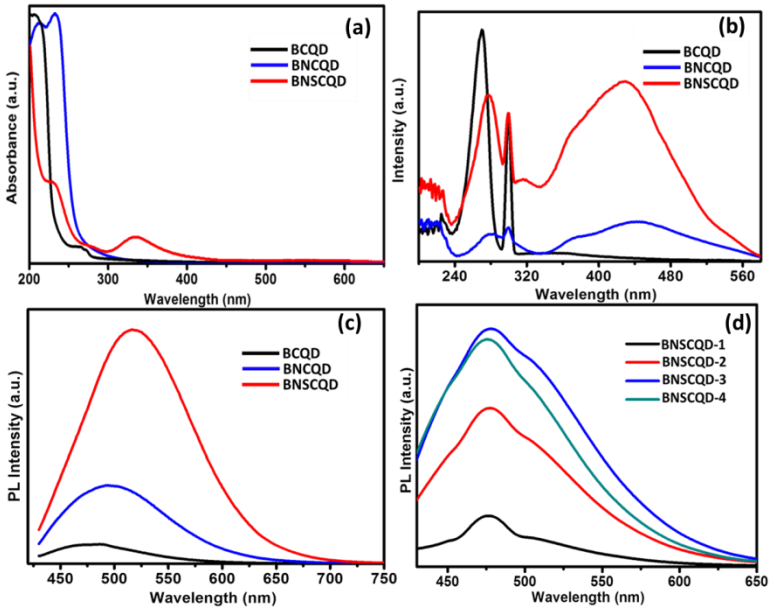

Fig. 5 (a) UV-vis absorbance spectrum, (b) PL excitation profile, (c) PL emission (λ_{ex} = 420 nm) spectra of doped carbon quantum dots (d) PL emission spectra (λ_{ex} = 420 nm) of BNSCQD with different boron contents

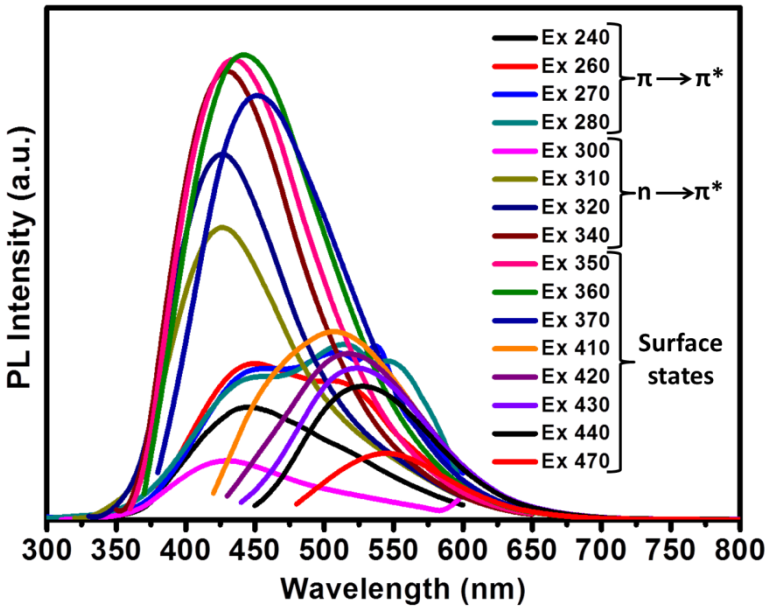

Fig. 6 PL emission spectra of BNSCQD-3 at various excitations

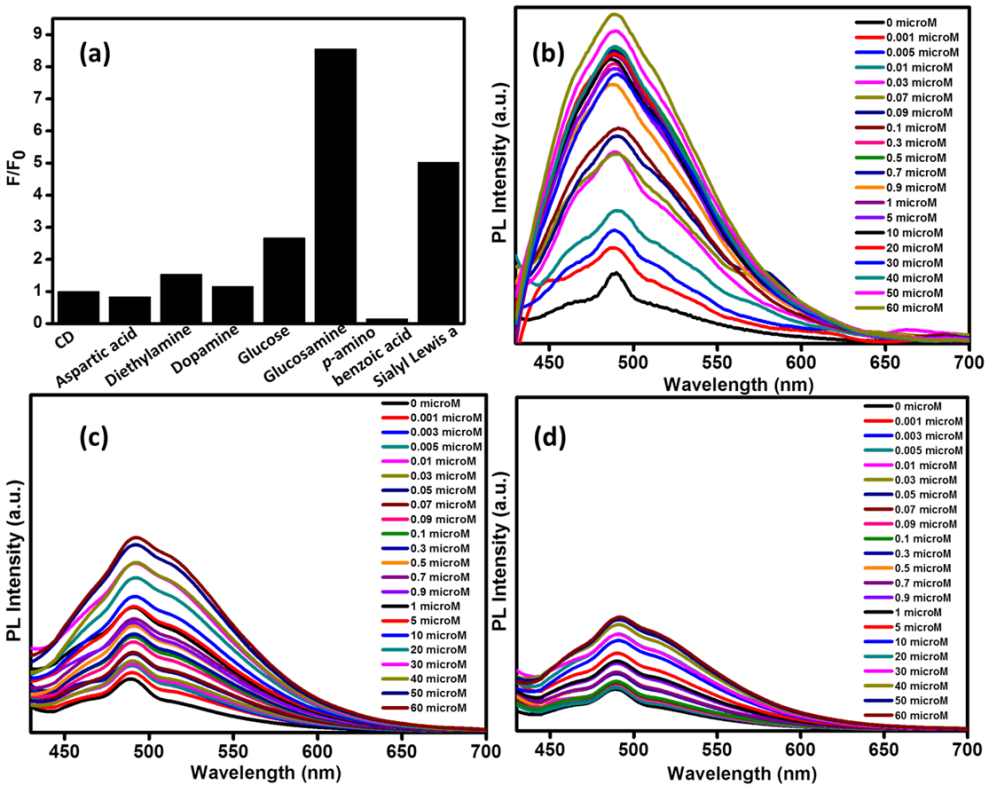

Fig. 7 (a) PL response of BNSCQD-3 to different analytes (60 mM), Characteristic PL turn on of BNSCQD with different concentrations of (b) glucosamine, (c) sialyl Lewis[a] and (d) glucose

Selective sensing by BNSCQD

First, the response of the BNSCQD probe to glucose and glucosamine was investigated. With the increase in concentration of both the analytes from 1 nM to 60 µM, the emission at 507 nm turns on. However, the enhancement in PL was much more pronounced in the case of

glucosamine as compared to glucose (Fig. 7). As selectivity is a critical parameter for the performance of the fluorescence chemosensor, we compared the response of BNSCQD towards glucose, diethylamine, dopamine and sialyl Lewis[a]. The relative order of turn on fluorescence emission of analytes is glucosamine > sialyl Lewis[a] > glucose > DEA > dopamine. Such a type of turn on fluorescence is consistent with the turn on sensing of glucose at a concentration higher than 0.1 mM reported by Qiu et al.[18] However, in our case, glucosamine shows the best turn on behavior at a concentration of 30 nM. Under the optimized conditions at pH 7.4 the limit of detection (LOD) for glucosamine was found to be 0.75 nM (Fig. 8), whereas that of sialyl Lewis[a] and glucose is found to be 0.2 µM and 0.7 µM respectively. To the best of our knowledge such a low detection limit offered by a BNSCQD fluorophore for glucosamine and sialyl Lewis[a] is the lowest compared to the respective quantum dot based fluorophores reported to date (Table 2).[37–41]

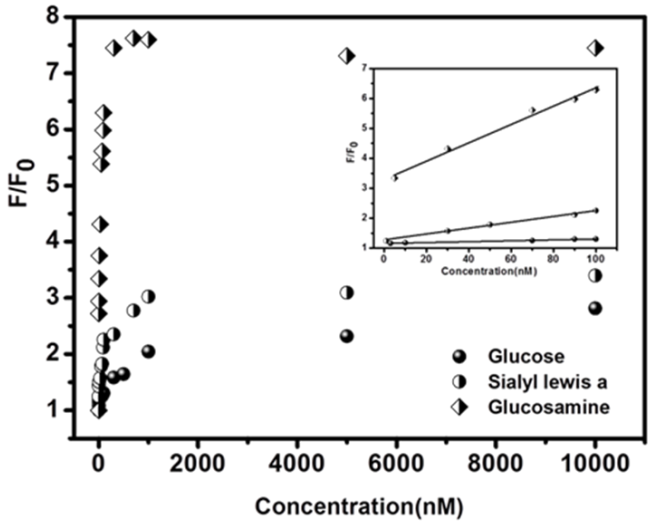

Fig. 8 Relative fluorescence (F/F0) vs. different concentration of analytes in PBS; inset: linear response

Table 2 Detection limits for QD based fluorophore and related biomolecules

Sensor	Analyte	Detection limit	Reference
Polymer-CD-VPBA	Glucose	0.1 mM	36
Boronic acid-CD	Glucose	1.5 µM	17
Boron doped GQD	Glucose	0.06 mM	18
Molecular imprinted GQD	Dopamine	0.1 nM	37
Aminoquinoline-GO	Glucosamine	5.5 µM	28
CD-Cu^{2+}	Guanine	6.7 nM	38
AgNP-CdSe-BA	Glucose	1.86 mM	39
lucigenin/thiourea dioxide	Dopamine	14.7 nM	40
BNSCQD	Glucosamine Sialyl Lewis a	0.75 nM 0.2 µM	Present work

PL response mechanism of BNSCQD towards glucosamine and sialyl Lewis^a

The response of the BNSCQD probe follows the order glucosamine > sialyl Lewis^a > glucose >DEA > dopamine. A very sensitive and enhanced response has been achieved in the case of glucosamine, advancing the sensing to a detectable level even at a concentration of 0.75 nM. It has been well established that cis-5,6 diol units of glucose reversibly bind with the boronic acid group to form a boronate ester. In the case of BNSCQD, the coexistence of nitrogen and sulphur along with boronic acid not only provides excellent luminescence properties when excited under visible light, but also adds on recognition sites for more specific sensing of amine containing saccharides. The synergistic effect of boronic acid-cis di-ol,6 keto-primary amine[11] and boron–nitrogen interaction results in a strong sensing towards glucosamine (Scheme 2a). On the other hand, thiophene has recently been reported to interact with secondary amines.[42] In our case although diethylamine shows a positive interaction with the BNSCQD sensor, the extent of turn on sensing is less when compared to that of sialyl Lewis^a. In case of sialyl Lewis^a, the combined interaction of boronic acid-cis di-ol and thiophene-secondary amine results in better sensing than diethyl amine and/or glucose (Scheme 2b). Such types of interactions induce aggregation among BNSCQD fluorophores, which positively restricts intramolecular rotation of luminescence centres, rigidifies structural conformations and blocks nonradiative emission channels. Hence, radiative decay is populated, enhancing the luminescence properties.

Scheme 2 Plausible binding sites for (a) glucosamine (b) sialyl Lewis^a with BNSCQD

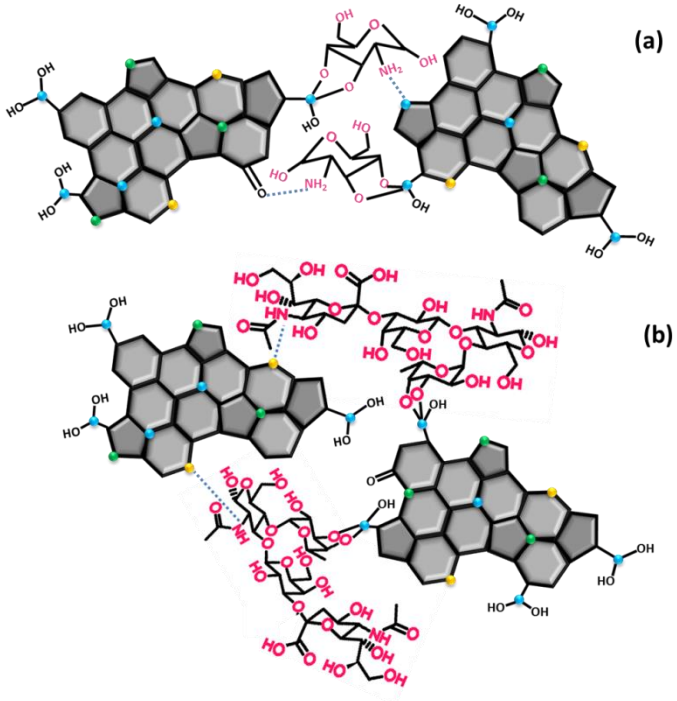

This proposed mechanism (Scheme 2) was also supported by measurement of particle size and DLS upon binding with glucosamine (Table 3). In addition to this, it was observed that there is no such change in turn on intensity of glucosamine in the presence of sialyl Lewis[a] or glucose (Fig. 9), which implies that there is no competitive binding of glucose or sialyl Lewis[a] with glucosamine. It was observed that there is a substantial increase in particle size when the glucosamine concentration varies between 10 nM and 60 µM, indicating induced aggregation among quantum dots through glucosamine. Furthermore, the proposed mechanism is also supported by the change in zeta potential of BNSCQD with and without glucosamine (Fig. 10). The zeta potential of BNSCQD at pH 4.0 is -26.1 mV. However it rises sharply to -12.5 mV upon addition of glucosamine. Zeta potential of glucosamine at pH 4 is only -5 mV. This supports the bonding of glucosamine onto the BNSCQD surface.

Table 3 Change in hydrodynamic size of BNSCQD on addition of different concentrations of glucosamine

BNSCQD (µg/mL)	Glucosamine (µM)	Particle size (nm)	Average no. of particles agglomerated
4	0	11.34	0
4	0.01	20.78	2
4	0.1	88.12	8
4	1	115.72	10
4	10	109.82	10
4	60	135.9	12

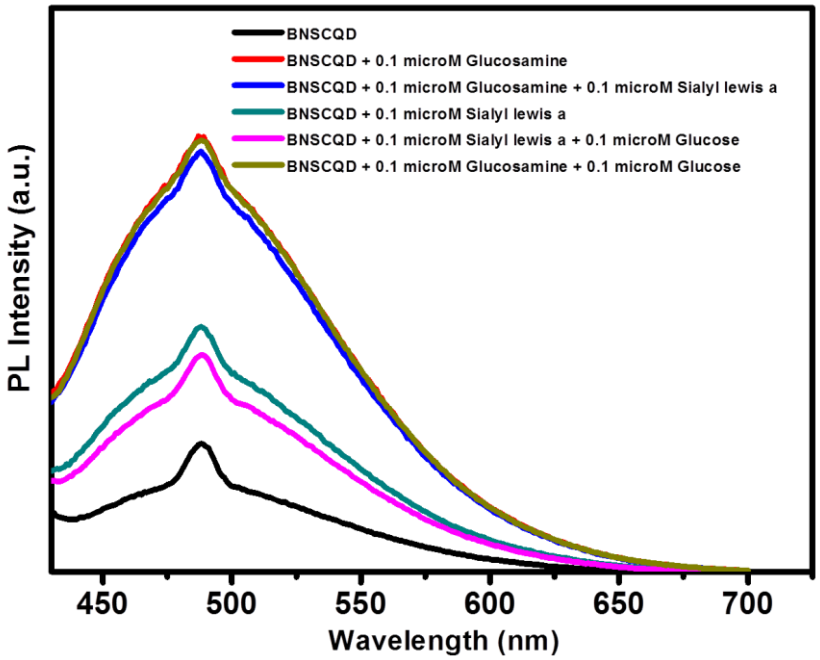

Fig. 9 Fluorescence spectra showing the competitive binding of glucosamine, glucose, sialyl Lewis[a] in presence of one another

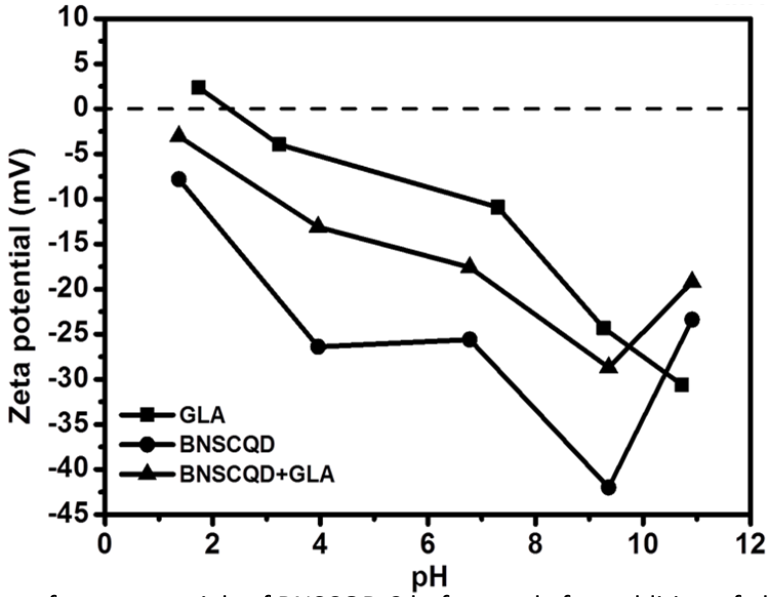

Fig. 10 Comparison of zeta potentials of BNSCQD-3 before and after addition of glucosamine

Effect of pH

The effect of pH on the intensity of the emission band was evaluated in order to explore the working pH range of the developed sensor. In accordance with the observation reported by Spagnuolo et al.[43] and Xia et al.,[17] for change in pH from the lower to the higher side, there is an increase in turn on intensity for glucose, sialyl Lewis[a] and glucosamine. At pH 7.4 the probe shows a 30% increase in intensity at 500 nm. Fig. 11a shows the correlation between reaction time and variation in glucosamine amount on PL sensing. It was found that the interactions can reach a balance at 0.5 h of reaction for different concentrations of analyte (Fig. 11b).

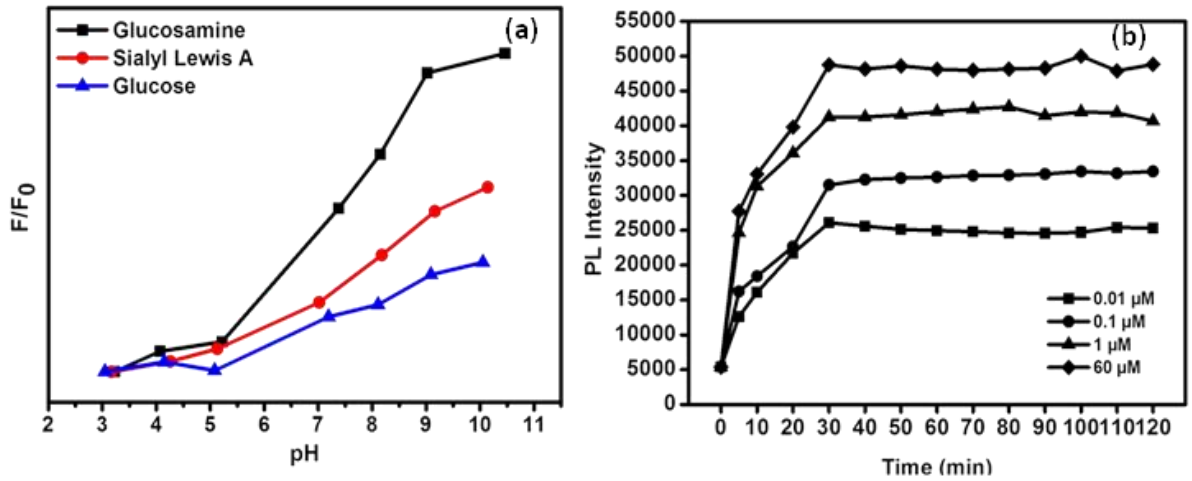

Fig. 11 (a) Effects of pH on the detection of analytes (F/F0 vs. pH). (b) Change in fluorescence intensity with respect to glucosamine concentration and time of incubation

Application of BNSCQD for naked eye detection of glucosamine

Inspired by the detection performance of BNSCQD for glucosamine in PBS, we proceeded to evaluate the detection potential of BNSCQD in a paper-based sensor strip. The BNSCQD embedded paper strip was exposed to glucosamine solution for 30 min and dried before the fluorescence measurement. The luminescence intensity of the paper-based sensor upon exposure to day light, LED (420 nm) and UV (340 nm) has been shown in Fig. 12. As the concentration of glucosamine increases, the intensity of emission increases with a good linear correlation from 0 to 60 µM. The detection limit for the paper based strip with an excitation at 340 nm and 420 nm was found to be 1.3 µM and 2.5 µM, which is parallel to the solution based PL turn on sensing (Fig. 12b and c). This indicates that the paper-based sensor is as good as the solution based sensor, even with a larger dynamic range.

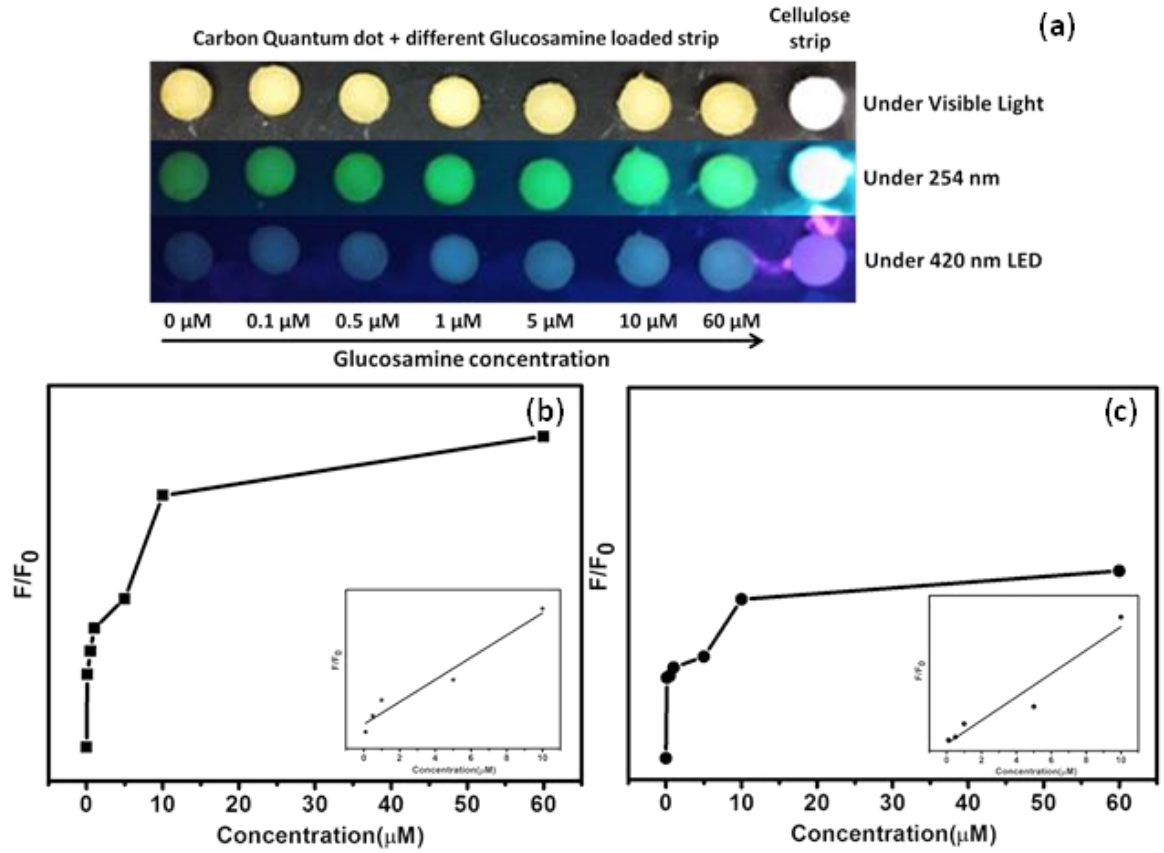

Fig. 12 (a) Fluorescence images of the paper-based sensor for visual detection of glucosamine at different concentrations under different wavelengths, relative fluorescence (F/F_0) vs. different concentration of glucosamine on strip under lights of wavelength (b) 340 nm and (c) 420 nm.

Imaging of liver cancer cells through glycan receptor

The cytotoxicity of BNSCQD was evaluated using HepG2 cells, L929, PC 3 and 3T3 cells by an MTT assay. There was no significant decrease in cell viability upon the addition of sensor up to 50 mg mL^{-1} in any of the cells (Fig. 13). Furthermore, to establish our sensor selectivity in targeted cell imaging, we labelled all the above mentioned cell types with BNSCQD. Interestingly, HepG2 cells showed stronger fluorescence due to maximum uptake of BNSCQD fluorophores compared to PC 3 and L929 cells (Fig. 14 and Fig. 15). The higher uptake of the probe in HepG2 cells is in accordance with the fact that HepG2 cells have much more fucosylated oligosaccharide antigens, such as sialyl Lewis[a] on the surface than L929, 3T3 and PC3 cells.[44,45] Since the phenylboronic acid groups are on the surface of BNSCQD, they readily bind to the cancer associated oligosaccharide antigens and promote the particle uptake of the cancer cells. The fluorescence intensity profiles from confocal microscopy also support the results (Fig. 16). In addition, with setting up the excitation wavelength at 405 nm, 488 nm and 546 nm, the emission colour changes to blue-green-red indicating the multicolour emission properties of the BNSCQD fluorophore under excitation in the visible range. These cell labelling outcomes suggest that our sensor can be used in biomedical imaging and clinical analysis.

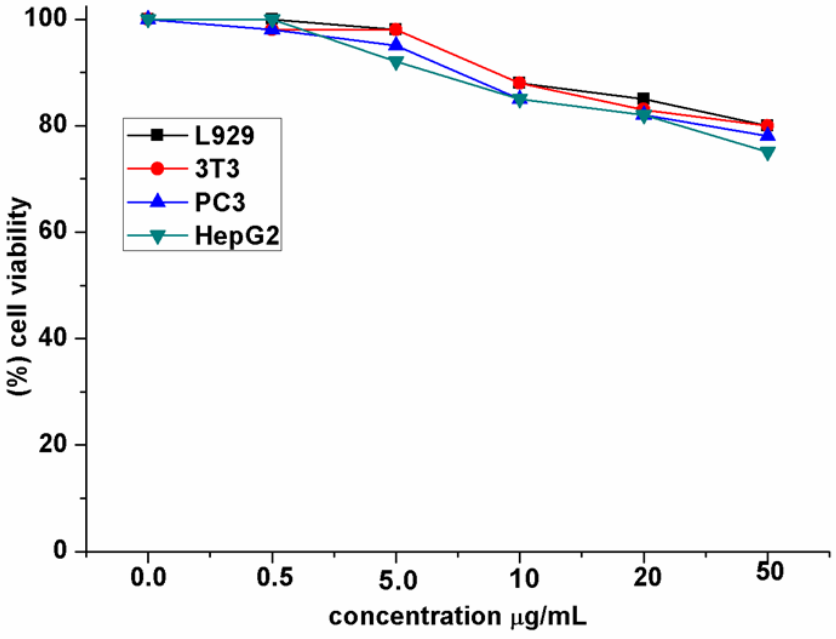

Fig. 13 Viability of different cell lines after incubation with BNSCQD for 72 h

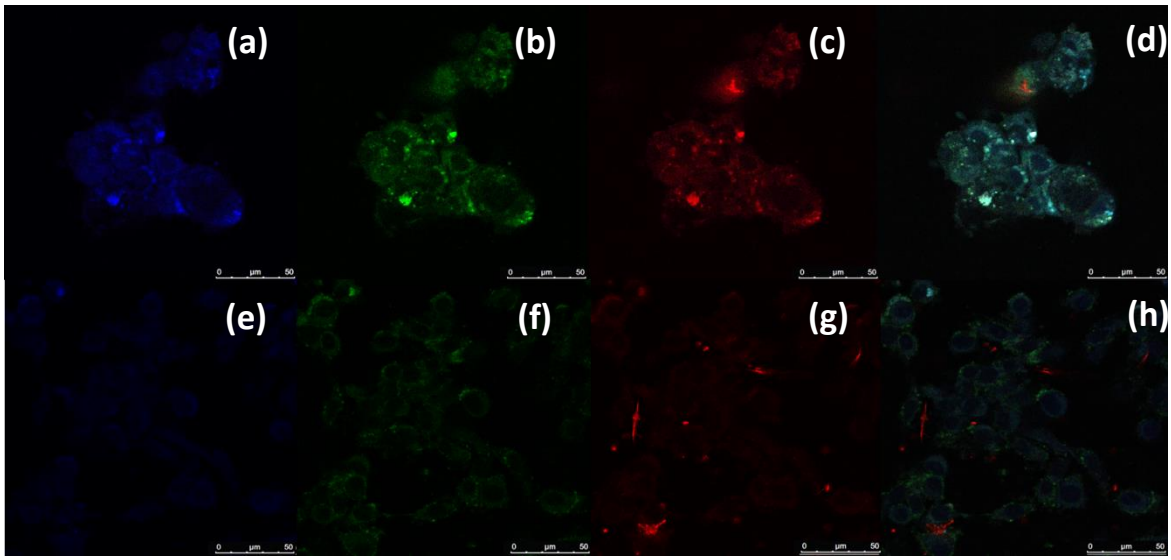

Fig. 14 Viability The fluorescence images of HepG2 cells stained with BNSCQD-3 under excitation wavelength (a) 405, (b) 488 and (c) 560 nm, L929 cells stained with BNSCQD-3 under excitation wavelength (e) 405, (f) 488 and (g) 546 nm and (d) and (h) are the merged images

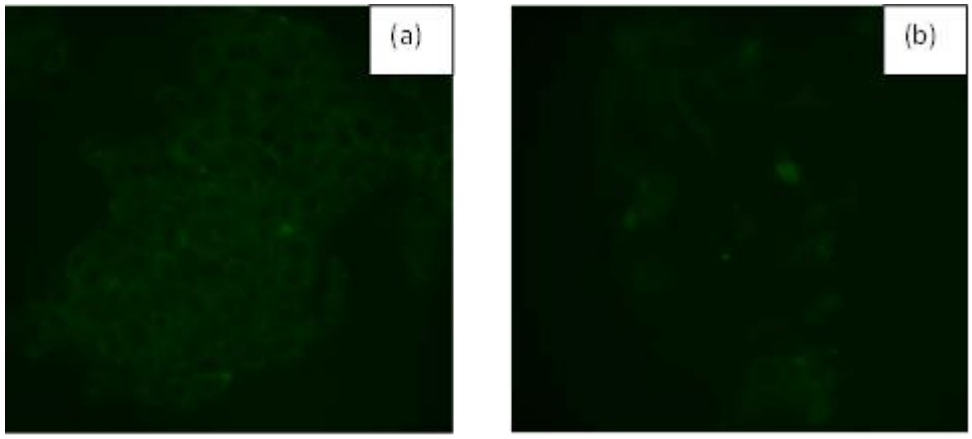

Fig. 15 Fluorescence image showing uptake of BNSCQD nanoparticles in (a) 3T3 and (b) PC 3 cells

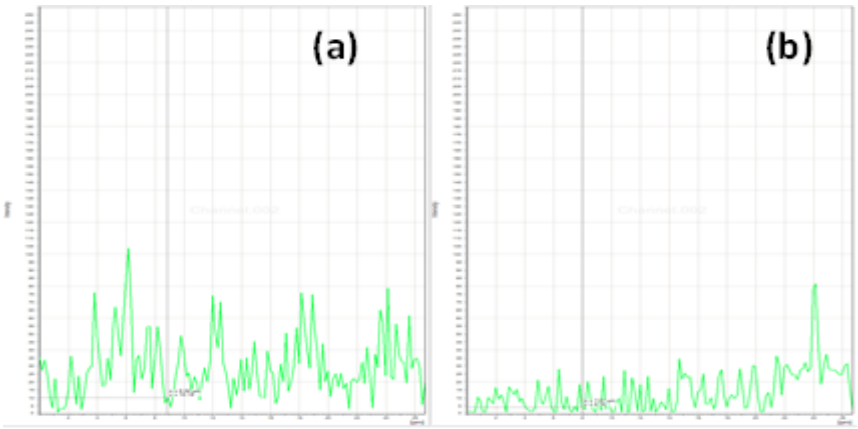

Fig. 16 Confocal fluorescence intensity profile for (a) HepG2 cells and (b) L929 cells

2.4 Conclusion

In this chapter,

- We have reported a novel fluorescent probe with a strong and sensitive OFF–ON response toward glucosamine, glucose and the oligosaccharide sialyl Lewis[a].
- The detection was achieved at a physiological pH in PBS. The BNSCQD probe strongly binds to glucosamine at nanomolar levels with a detection limit of 0.75 nM.
- To the best of our knowledge, this is the only quantum dot based sensor operating in the visible region for the detection of glucosamine at the nanomolar level.
- In addition, such CQDs can be spread on a cellulose paper strip to fabricate a sensor strip for visual detection of glucosamine with a detection limit of 2.5 mM. Such a paper-based sensor provides a novel strategy for the design of selective probes for other targets with advantages of easy handling, incorporation into devices, simplicity and cost effectiveness.
- Furthermore, this probe can be incorporated in a drug delivery system to get multiple advantages of receptor targeting and bioimaging on a single platform.

2.5 References

1. M. Y. Berezin and S. Achilefu, *Chem. Rev*., 2010, **110**, 2641–2684.
2. C. Wu and D. T. Chiu, *Angew. Chem., Int. Ed*., 2013, **52**, 3086–3109.
3. J. Yao, M. Yang and Y. Duan, *Chem. Rev*., 2014, **114**, 6130–6178.
4. O. S. Wolfbeis, *Chem. Soc. Rev*., 2015, **44**, 4743–4768.
5. A. B. Chinen, C. M. Guan, J. R. Ferrer, S. N. Barnaby, T. J. Merkel and C. A. Mirkin, *Chem. Rev*., 2015, **115**, 10530–10574.
6. X. Sun, W. Zhai, J. S. Fossey and T. D. James, *Chem. Commun*., 2016, **52**, 3456–3469.
7. X. Wu, Z. Li, X. X. Chen, J. S. Fossey, T. D. James and Y. B. Jiang, *Chem. Soc. Rev.*, 2013, **42**, 8032–8048.
8. N. Y. Edwards, T. W. Sager, J. T. McDevitt and E. V. Anslyn, *J. Am. Chem. Soc*., 2007, **129**, 13575–13583.
9. J. Zhai, T. Pan, J. Zhu, Y. Xu, J. Chen, Y. Xie and Y. Qin, *Anal. Chem*., 2012, **84**, 10214–10220.
10. Z. Zhong and E. V. Anslyn, *J. Am. Chem. Soc*., 2002, **124**, 9014–9015.
11. T. Tran, Y. Alan and T. E. Glass, *Chem. Commun*., 2015, **51**, 7915–7918.

12. X. D. Xu, H. Cheng, W. H. Chen, S. X. Cheng, R. X. Zhuo and X. Z. Zhang, *Sci. Rep*., 2013, **3**, 2679, DOI: 10.1038/srep02679.
13. H. Liu, Y. Li, K. Sun, J. Fan, P. Zhang, J. Meng, S. Wang and L. Jiang, *J. Am. Chem. Soc*., 2013, **135**, 7603–7609.
14. S. K. Wang and C. M. Cheng, *Chem. Commun*., 2015, **51**, 16750–16762.
15. K. Yum, J. H. Han, T. P. McNicholas, P. W. Barone, B. Mu, J. H. Kim, R. M. Jain and M. S. Strano, *ACS Nano*, 2012, **6**, 819–830.
16. Y. H. Li, L. Zhang, J. Huang, R. P. Liang and J. D. Qiu, *Chem. Commun*., 2013, **49**, 5180–5182.
17. P. Shen and Y. Xia, *Anal. Chem*., 2014, **86**, 5323–5329.
18. L. Zhang, Z. Y. Zhang, R. P. Liang, Y. H. Li and J. D. Qiu, *Anal. Chem*., 2014, **86**, 4423–4430.
19. H. Gray, P. Hucheson and R. Slacin, *J. Allergy Clin. Immunol*., 2004, **114**, 459–460.
20. C. T. Vangsness, W. Spiker and J. A. Erickson, *Arthroscopy*, 2009, **25**, 86–94.
21. J. Erickson and T. Messer, *J. Hand. Surg. Am*., 2013, **38**, 1638–1640.
22. B. Q. Liu, X. Meng, C. Li, Y. Y. Gao, N. Li, X. Niu, Y. Guan, H. Q. Wang, B. Q. Liu, X. Meng, C. Li, Y. Y. Gao, N. Li, X. F. Niu, Y. Guan and H. Q. Wang, *Exp. Mol. Med*., 2011, **43**, 487–493.
23. J. Y. Reginster, A. Neuprez, M. P. Lecart and N. Sarlet, *J. Rheumatol*., 2012, **32**, 2959–2967.
24. S. Wandel, P. Juni, B. Tendal, E. Nuesch, P. Villiger, N. J. Welton, S. Reichenbach and S. Trelle, *BMJ*, 2010, **314**, c4675.
25. S. G. Petersen, N. Beyer, M. Hansen, L. Holm, P. Aagaard, A. L. Mackey and M. Kjaer, *Arch. Phys. Med. Rehabil*., 2011, **92**, 1185–1193.
26. S. Santhosh, R. Anandan, T. K. Sini and P. T. Mathew, *J. Gastroenterol. Hepatol.*, 2007, **22**, 949–953.
27. C. R. Cooper and T. D. James, *Chem. Commun*., 1997,**42**, 1419–1420.
28. F. Zaubitzer, A. Buryak and K. Severin, *Chem. Eur. J.*, 2006, **12**, 3928–3934.
29. R. Cheng, Y. Liu, S. Ou, Y. Pan, S. Zhang, H. Chen, L. Dai and J. Qu, *Anal. Chem.*, 2012, **84**, 5641–5644.
30. S. Mohapatra, S. Sahu, N. Sinha and S. K. Bhutia, *Analyst*, 2015, **140**, 1221–1228.
31. Q. Xu, Y. Liu, C. Gao, J. Wei, H. Zhou, Y. Chen, C. Dong, T. S. Sreeprasad, N. Li and Z. Xia, *J. Mater. Chem. C*, 2015, **3**, 9885–9893.

32. W. Wei, C. Xu, L. Wu, J. Wang, J. Ren and X. X. Qu, *Sci. Rep*., 2014, **4**, 3564, DOI: 10.1038/srep03564.
33. H. K. Sadhanala and K. K. Nanda, *Carbon*, 2016, **96**, 166–173.
34. Q. Xu, P. Pu, J. Zhao, C. Dong, C. Gao, Y. Chen, J. Chen, Y. Liu and H. Zhou, *J. Mater. Chem. A*, 2015, **3**, 542–546.
35. X. Shan, L. Chai, J. Ma, Z. Qian, J. Chen and H. Feng, *Analyst*, 2014, **139**, 2322–2325.
36. Y. Dong, H. Pang, H. B. Yang, C. Guo, J. Shao, Y. Chi, C. M. Li and T. Yu, *Angew. Chem., Int. Ed.*, 2013, **52**, 1–6.
37. H. Wang, J. Yi, D. Velado, Y. Yu and S. Zhou, *ACS Appl. Mater. Interfaces*, 2015, **7**, 15735–15745.
38. X. Zhou, A. Wang, C. Yu, S. Wu and J. Shen, *ACS Appl. Mater. Interfaces*, 2015, **7**, 11741–11747.
39. S. Pang, Y. Zhang, C. Wu and S. Feng, *Sens. Actuators, B*, 2016, **222**, 857–863.
40. Y. Tang, Q. Yang, T. Wu, L. Liu, Y. Ding and B. Yu, *Langmuir*, 2014, **30**, 6324–6330.
41. W. Gao, L. Qi, Z. Liu, S. Majeed, S. A. Kitte and G. Xu, *Sens. Actuators, B*, 2017, **238**, 468–472.
42. Y. Fu, L. Shi, D. Zhu, C. He, D. Wen, Q. He, H. Cao and J. Cheng, *Sens. Actuators, B*, 2013, **180**, 2–7.
43. C. S. Lopez, M. A. Huvelle, M. L. Uhrig, F. C. Leskowb and C. C. Spagnuolo, *Chem. Commun*., 2015, **51**, 4895–4898.
44. W. Yang, S. Gao, X. Gao, V. V. Karnati, W. Ni, B. Wang, W. B. Hooks, J. Carson and B. Weston, *Bioorg. Med. Chem. Lett.*, 2002, **12**, 2175–2177.
45. W. Yang, H. Fan, X. Gao, S. Gao, V. V. Karnati, W. Ni, W. B. Hooks, J. Carson, B. Weston and B. Wang, *Chem. Biol*., 2004, **11**, 439–448.

Chapter – 3

Dopamine integrated B, N, S doped CQD nanoprobe for rapid and selective detection of fluoride ion

3.1 Introduction

Among the emerging biologically and environmentally significant anions fluoride has risen as an attractive sensing target owing to its association with a diverse array of biological, medical, and technological processes.[1-6] Apart from its crucial role in maintaining dental caries, fluoride ions are used as pharmaceutical agents to treat osteoporosis.[7] Although fluoride is easily absorbed by the body but it is excreted slowly. As a result, overexposure to fluoride can lead to acute gastric, kidney disorder, urolithiasis and even death.[8,9] Also frequent exposure to fluoride ions causes oxidative stress and damage to mitochondria and decreases mitochondrial respiratory chain efficiency leading to neurodegenerative diseases.[10-13] Fluorescence sensing has been emerging as an efficient detection method because of its high sensitivity, spatiotemporal resolution.[8,9,14] In past few years considerable effort has been made to develop a fluorescence sensor for the detection F^- in aqueous medium and intracellular environment. Till now a variety of fluoride sensors have been reported where most of these sensors rely on strong interactions between Lewis-acidic boron and fluoride, [15-17] silicon which features particularly the stable bonding between Si-F bond,[13,18] Fe^{3+} and F^- forming stable FeF_6^{3-} ,[19] hydrogen bonding pyrazole H and fluoride and many other types of interactions involving fluoride as a participant or a disrupter and has been discussed in two excellent reviews by Yoon et al. and Duan et al. [4,20] The binding of fluoride in aqueous medium has always been challenging because of the high hydration enthalpy of the fluoride ion. Therefore very few reports are there on turn-on fluorescence sensing fluoride in absolutely aqueous medium.[21-23] However, most of these sensors lack selective recognition of fluoride over oxygen containing anions like $H_2PO_4^-$, CH_3COO^-, CO_3^{2-}, and PO_4^{3-}, suffer from low detection limit, poor photo as well as chemical stability and lacks intracellular application. To develop a more suitable F^- chemosensor applicable for environment and biological systems is desirable. On the other hand, with fascinating photoluminescence properties, carbon dots (C-dots) and graphene oxide (GO) nanoparticles both are becoming an important class of imaging probes and a versatile platform for engineering multifunctional nanosensors.[24-26] In order to transfer C-dots from proof-of-concept studies toward real world applications such as in vivo bioimaging and biosensing, careful design and engineering of C-dot probes is becoming increasingly important. So far our knowledge only two papers are published on direct application of fluorescence graphene oxide nanoparticles for sensing fluoride in aqueous medium where the limit of detection can go up to 10^{-12}M. For instance, Jiang et al. demonstrated GO based nanosensor where the fluorescence of GO was quenched

by the AgNPs, and trace F^- can recover the fluorescence of the quenched photoluminescent GO via cleavage of cyclic ester between phenyl boronic acid and diol.[27] Gao and coworkers have developed a different strategy where fluorescence property of N-GO was completely quenched by Fe^{3+} ion and subsequently turned on by addition of F^-.[19] Although these sensors showed remarkable potential for ultrasensitive visual detection of fluoride, the suitability of these sensors in cellular environment or in presence of other metal ions has not been discussed. Moreover, these sensors require UV excitation for monitoring fluoride which is not preferable in biological samples.

In this work, we demonstrate a highly sensitive visible light operated fluorescence sensing system in absolutely aqueous medium and also in living cells. For this purpose a novel highly luminescent heteroatom doped (B, N, S) carbon quantum dot has been synthesized in a single step hydrothermal treatment. This quantum dot holds boronic acid groups on its surface which is a well-known functional group for selective recognition of 1,2-diol or 1,3-diol via formation of five- or six-membered cyclic esters. By combining B,N,S co-doped carbon quantum dot with dopamine a fluorescence probe has been developed where the fluorescence intensity of carbon dot is quenched by electron transfer between carbon quantum dot and dopamine. An efficient sensing of fluoride has been achieved by turning on the quenched fluorescence by addition of fluoride.

3.2 Experimental

Materials

Sodium fluoride, sodium acetate, sodium carbonate, sodium nitrate, disodium hydrogen phosphate, sodium sulphate, dopamine, 3-aminophenylboronic acid monohydrate, potassium bromide and deionized water were purchased from Sigma Aldrich. Sodium iodide, and sodium chloride was supplied by Finar chemicals. Citric acid was procured from Nice chemicals. Thiourea and absolute ethanol were purchased from Merck Ltd. and Changshu Yangyuan chemicals respectively. The experiments were carried out in phosphate buffer saline (PBS) solution. Initial experiments were done with 10 µL of BNSCQD (2 mg mL^{-1}) and variable concentrations of freshly prepared dopamine solution (0.1 – 1.7 µM) in 4 mL PBS solution.

Preparation of sensor (BNSCQD-Dopamine)

As reported in our earlier work, BNSCQD was synthesized using 3-amino phenyl boronic acid, Citric acid and thiourea as precursors. The obtained dispersion was filtered through .22µm filter paper to remove larger particles. The unreacted organic impurities were isolated from yellowish brown carbon dot solution by repeated washing with DCM followed by centrifugation at 80000 rpm. The obtained dispersion was dialysed against deionized water using a dialyzer with a molecular weight cut off 1000Da for 24h. Then, 10 µL (5 µg mL^{-1}) BNSCQD was pipetted out and diluted with 3 mL of deionized water. To this a standard amount of 20 µL (1.7 µM) dopamine was added. Finally the solutions were prepared in batches and incubated at 37 °C for 10 minutes, for implying towards fluoride sensing.

Fluorescence sensing of Fluoride

The experiments were carried out in phosphate buffer saline (PBS) solution. Initial experiments were done with 10 µL of BNSCQD (2 mg mL^{-1}) and different concentration of freshly prepared dopamine solution (0.1 – 1.7 µM) in 4 mL PBS solution. In a typical run, BNSCQD with 1.5 µM dopamine solution was used as the sensing medium and titrated against various concentrations (0.01 – 5 nM) of fluoride ion (NaF). The raise in fluorescence intensity was found to be promising in detecting F^- ions at low concentrations in aqueous medium (Figure 3b). The Stern-Volmer plot shows the florescence response of sensor solution versus equivalents of fluoride ion (PBS), the intercept or detection limit was found to be 0.76 pM. To confirm the response time, the PL response was noted at different time intervals. PL spectra were recorded after an incubation period of 30 min at 37 ˚C. The sensitivity and selectivity for fluoride was confirmed by comparing other anions stock solutions in a similar way at a concentration of 5 nM. The recovery percentage of fluoride content was monitored using tap water, lake water, human serum and toothpaste as samples (Table 1). The amount of F^- was maintained at $1x10^2$ and $2.2x10^2$ pM respectively.

Characterization

Photoluminescence spectra were collected on a Horiba FluoroMax-4 fluorimeter. The phase formation and crystallographic state of the material were investigated using an Expert Pro Phillips X-ray diffractometer. Morphological, microstructural analysis and elemental mapping were done using a high resolution transmission electron microscope (FEI Technai G2 30ST) operated at 300 kV. The presence of surface functional group was investigated

through FTIR recorded by an IRAffinity-1S, Shimadzu, spectrophotometer. Surface composition of BNSCQD was verified by XPS using AlKα excitation source in PHI 5000 Versa Prob II (FEI Inc) instrument. The Raman spectrum of as-prepared samples was recorded on a Renishaw invia Raman spectrometer (UK model). Particle size and mean zeta potential at different pH values were measured using Nano ZS 90, Malvern instrument. Live-cell images were captured under Leica TCS SP8 confocal microscope with laser excitations at 405, 488 and 546 nm.

Fluoride sensing in living cell

HT 29 celllines (3×10^4) cell lines were seeded into 24 well plates and incubated in 400 µL DMEM containing 10% FBS and 1% antibiotic (penicillin, streptomycin) at 37°C inside the incubator with 5% CO_2. After 24 h of incubation, media were removed and replaced with fresh DMEM without serum containing BNSCQD at concentration 30 µg/mL for each type of cell. After incubation for 3h, media was removed and washed three times with 1XPBS. Thereafter, cells were fixed with 2% paraformaldehyde (PFA) for 15 min at RT followed by washing with 1×PBS and viewed fluorescence microscope.

3.3 Results and discussion

Optimization of BNSCQD-Dopamine probe and sensing mechanism

B, N, S codoped carbon quantum dots with intense luminescence and PLQY 28% has been prepared by optimizing the precursor ratio, citric acid: thiourea: m-aminophenyl boronic acid = 0.5: 0.5: 0.3 following the synthetic procedure reported in our previous paper.[28] The aqueous dispersion of carbon dots remains stable up to 1 month without any significant change which was verified by taking PL and absorption spectra after different time intervals (Fig. 1).

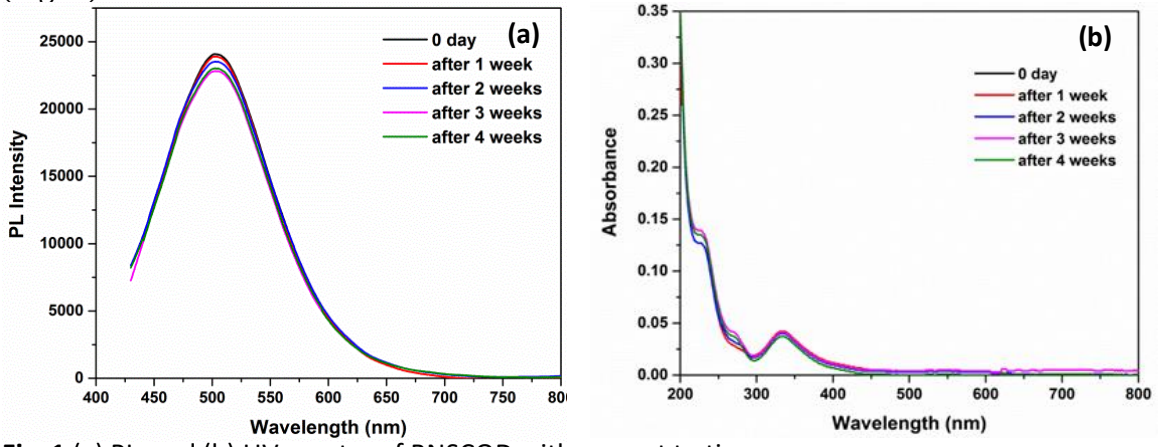

Fig. 1 (a) PL and (b) UV spectra of BNSCQD with respect to time.

Fluorescence study of sensor

It was observed that addition of dopamine into aqueous solution of BNSCQD at neutral pH led to PL quenching of C-dot at excitation 420 nm. Fig. 2a shows the luminescence spectra of BNSCQD with various concentrations of dopamine. The PL intensity of BNSCD gradually decreases with dopamine in dopamine concentration range 0 to 1.7 µM. Fig. 2b shows the plot of F/F_0 versus dopamine concentration which shows a linear fit with a correlation coefficient of 0.987. Addition of dopamine to the aqueous solution of BNSCQD leads to significant quenching of fluorescence with an obvious blue shift of the maximum emission wave length from 500 nm to 480 nm due to strong interaction of BNSCQD with dopamine. However the fluorescence was recoverable on addition of fluoride. A good linear relationship between the relative emission intensity I/I_0 and F^- was observed in a wide concentration range 0 to 5 nM suggesting that BNSCQD can potentially be used for sensing F^- in a low concentration range.

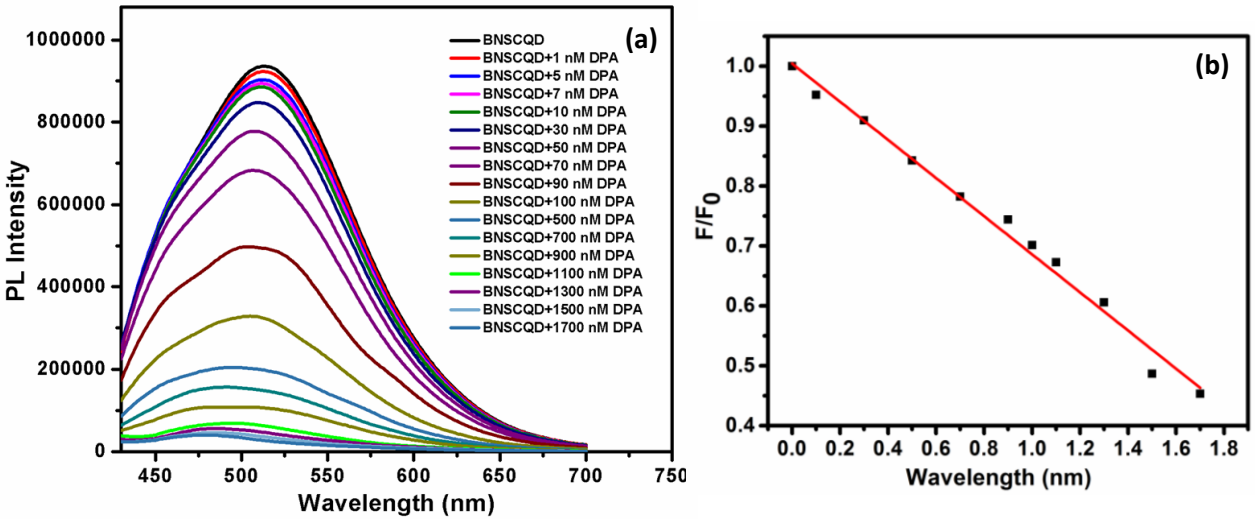

Fig. 2 (a) Change in the fluorescence spectra of BNSCQD on gradual addition of dopamine and (b) Fluorescence quenching of BNSCQD solution as a function of dopamine concentration.

Zeta potential

It was well evidenced that carbon dots can act as electron donors as well as acceptors in the excited state through a photoinduced electron transfer (PET) mechanism.[29] Purkayastha et al. have elaborately studied the electron transfer between carbon dot and dopamine.[30] Dopamine has isoelectric point 9.7. At low pH dopamine–hydroquinone is predominant and acts as an electron donor to the CQD acceptor, whereas, at higher pH dopamine–quinone is formed and acts as an electron acceptor where the CQD acts as the donor. At neutral pH an equiproportion of dopamine–hydroquinone and dopamine–quinone results in a plateau in

fluorescence quenching. We anticipate the similar kind of electron transfer process incase of our BNSCQD probe. The interaction of BNSCQD with dopamine is facilitated through boronic acid-diol interaction to form cyclic ester. The formation of BNSCQD-dopamine complex can be confirmed from remarkable reduction of zeta potential from -34 mV to -28 mV (Fig. 3). In addition to this the particle size of the BNSCQD was decreased upon addition of dopamine indicating breaking of hydrogen bonding among boronic acid modified carbon dots upon formation of cyclic boronate esters which is a fast reaction.[31,32]

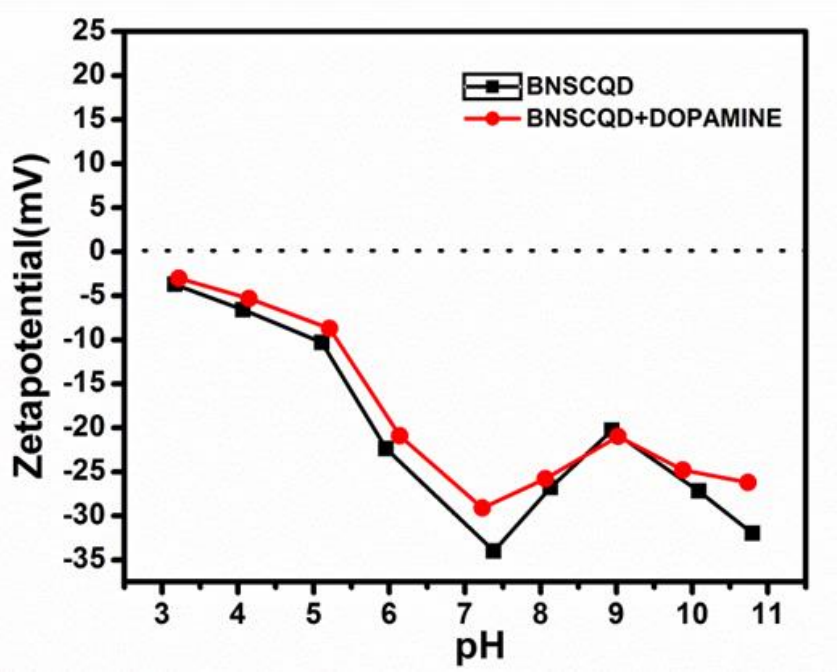

Fig. 3 Change in ZP of BNSCQD upon addition of dopamine.

Photoinduced electron transfer

The fluorescence quenching of excited state BNSCQD may be a result of Fluorescence Resonance Energy Transfer (FRET) or photoinduced electron transfer. The emission spectrum of BNSCQD and absorption spectrum of DOPA do not overlap (Fig. 4a) which rules out the possibility for FRET between BNSCQD and dopamine. The simultaneous change of intensity of BNSCQD and dopamine makes a possibility of electron transfer between quantum dot and dopamine. From comparison of fluorescence spectra of dopamine, BNSCQD and BNSCQD+dopamine under excitation at 280 nm, it is clear that the fluorescence quenching of BNSCQD is not accompanied by the simultaneous gain of fluorescence by dopamine, instead fluorescence of both are quenched to some extent (Fig. 4b), which indicates a possible electron transfer process as reported by Yan et al.[33] Such kind of electron transfer from BNSCQD to quinone form of dopamine is consistent with the

photoinduced electron transfer from semiconductor quantum dot to dopamine reported by Medintz et al.[34] Following photoexcitation, the QD conduction-band electron is transferred to the lowest unoccupied molecular orbital of a quinone acceptor, resulting in PL quenching, and the electron is then shuttled back to the QD valence band. The surface boronic acids on BNSCQD are mainly responsible for molecular recognition of dopamine by BNSCQD. It can be anticipated that as dopamine comes in contact with boronic acid modified CQD a BNSCQD-dopamine complex is formed through fast formation of tetrahedral boronate ester as shown in scheme 1. The appearance of this electron acceptor dopamine near the QD provides a favourable non-radiative channel for increased QD quenching.

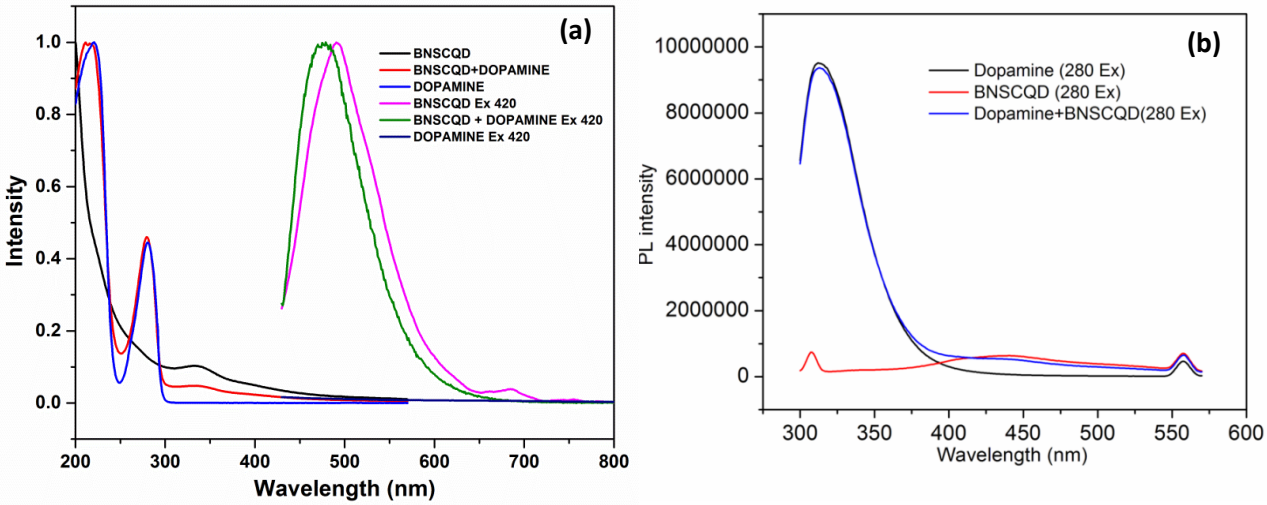

Fig. 4 (a) Absorption and emission spectra of dopamine and BNSCQD, (b) PL of Dopamine, BNSCQD and BNSCQD+Dopamine at Ex 280 nm showing the possibility of electron transfer process.

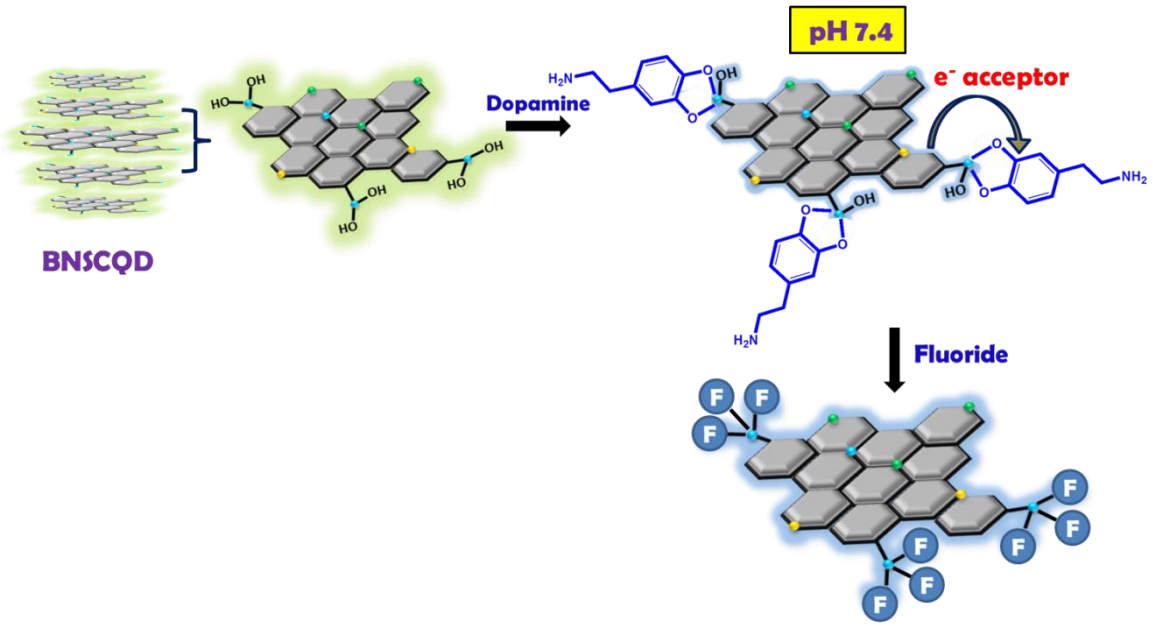

Scheme 1 Schematic presentation of sensing of fluoride by BNSCQD-dopamine sensor.

To verify the impact of surface boronic acid one control experiment was performed. When dopamine was added to the equal concentration of NSCD (without boron doping) the extent of fluorescence quenching was much less as compared to the PL quenching in case of BNSCQD (Fig. 5). This implies that the interaction between surface boronic acid and di-ol of dopamine leading to tetrahedral boronate ester, is the driving force to bring dopamine in close contact with BNSCQD, which ultimately results in an efficient electron transfer process. The dynamic experiments evidenced that the reaction of dopamine and BNSCQD takes 30 minutes to complete and intense green colour of BNSCQD turns blue (scheme 1). It is well established that fluoride can easily break cyclic boronate esters via fluoride-boron interactions. Boron has an empty p orbital that can easily accept an external lone pair electron and thus F^- strongly interact with boron atom. Therefore we design a turn-on fluorescence sensor for the construction of visual nanoprobe towards F- detection utilizing the advantage of boron-fluoride interaction.

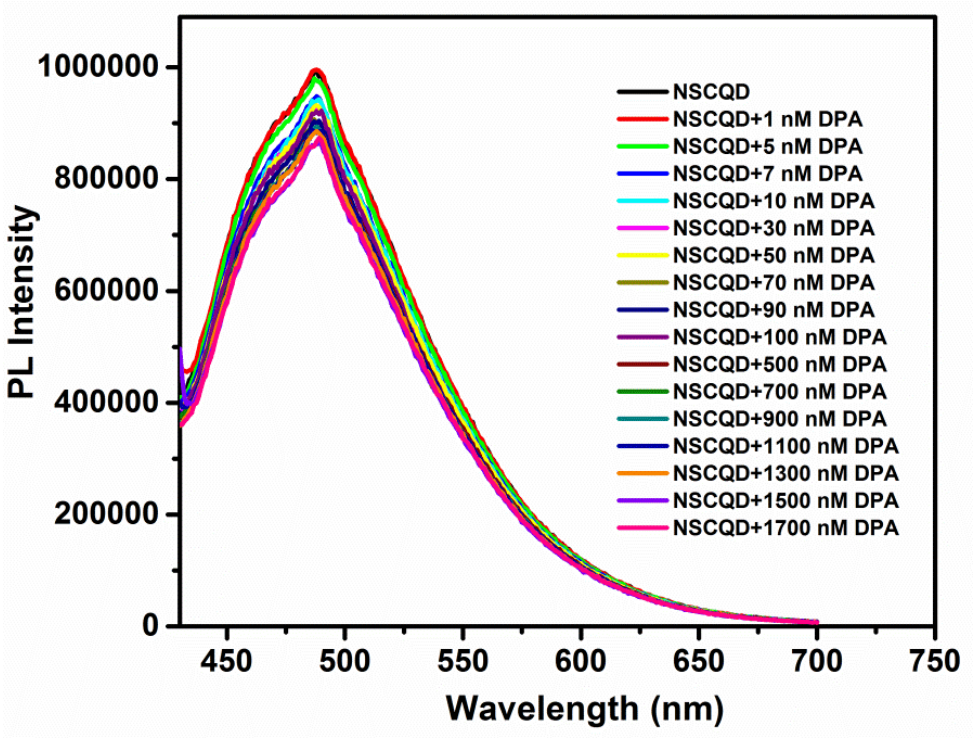

Fig. 5 Change in PL of NSCQD in presence of dopamine.

Fluorescence based fluoride sensing

When fluoride is added to the BNSCQD-DA nanoprobe the fluorescence was dramatically increased due to two reasons. (1) Interruption in photoinduced electron transfer. The binding of fluoride anion to the central boron atom generate the tetrahedral trifluoroboron complex which promtote sp^2-sp^3 transition of boron and weaken the formation

of BNSCQD-dopamine complex which ultimately perturbs photoinduced electron transfer and enhances the fluorescence of BNSCQD (Scheme 1). (2) Incorporation of fluorine in BNSCQD adds extra luminescence. The enhancement in intensity of F-BNSCQD w.r.t. BNSCQD is because F atom has lone-pair electrons and BNSCQD has a large π-conjugated system as well as surface functional groups. The incorporation of F into the π-conjugated scaffold can promote the formation of p-π conjugation, which increases the electron density on the HOMO. These active electrons were more easily irradiated and subsequently resulted in a high fluorescent intensity. During excitation, more electrons are jumped to the LUMO, which subsequently results in enhanced fluorescence intensity. The successful binding of F into the BNSCQD structure was also indicated by the red shift of emission peak in the fluorescent spectra (Fig. 6). We then validated the above sensing mechanism and its sensitivity for the detection of the fluoride ion. At optimal conditions the variation of fluorescence intensity of BNSCQD-dopamine sensor in the presence of different concentration of fluoride is presented in Fig. 6. A linear response of fluorescence intensity versus F- concentration is obtained in the range 0 to 5 nM with a limit of detection 0.7 pM (Fig. 7) which has been calculated based on our previously reported protocol.[35]

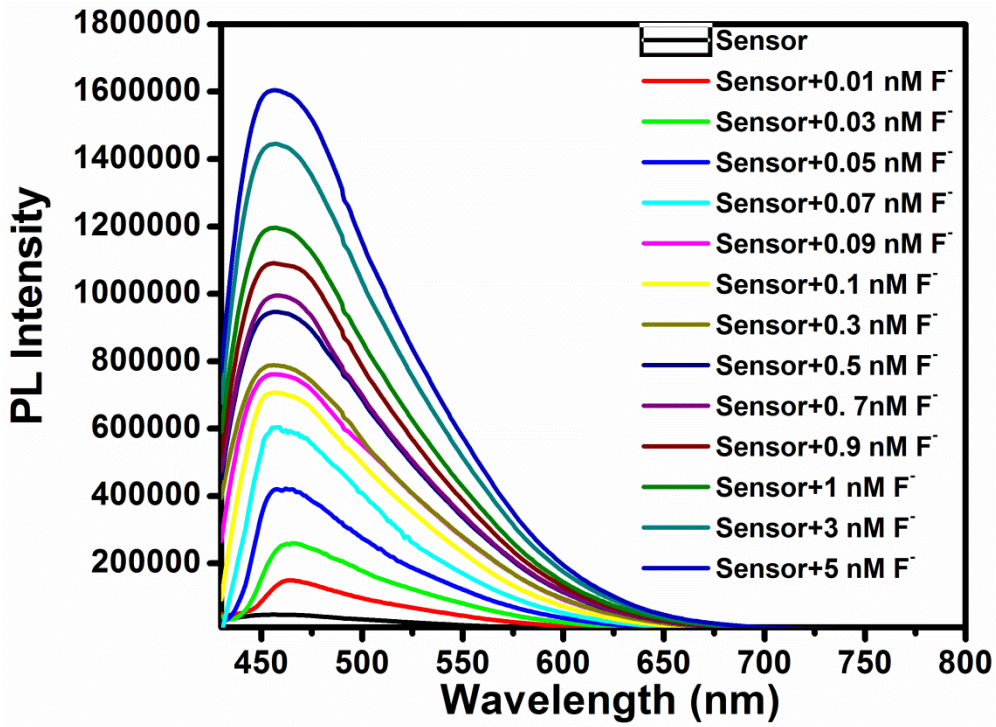

Fig. 6 Change in PL spectrum of BSCQD-DOPA sensor on gradual addition of fluoride.

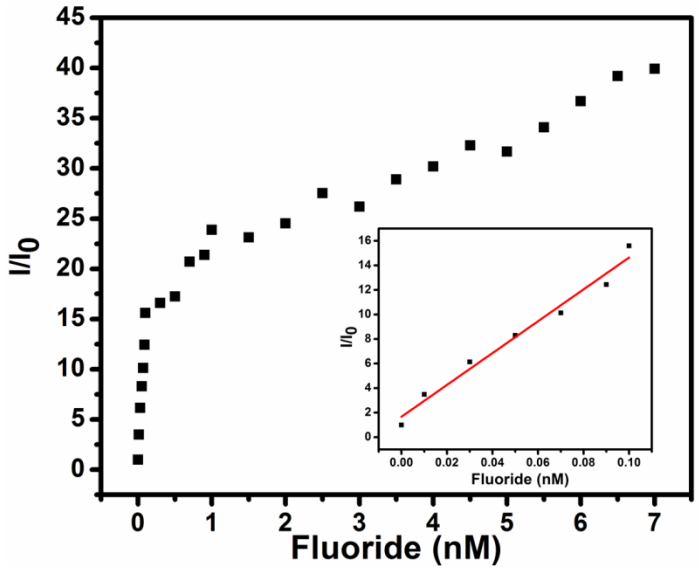

Fig. 7 Change in luminescence intensity of BNSCQD-Dopamine on addition of fluoride, inset shows the linear range.

The effect of pH on the intensity of emission band was evaluated in order to explore the working pH range of the developed sensor. Therefore, the interaction between BNSCQD-dopamine and fluoride at different pH values (pH 4-9) was studied. When the pH of the medium was 9, there was maximum turn-on response (F/F_0) towards fluoride (Fig. 8a). This may be attributed to the lowest intensity of BNSCQD-dopamine probe at pH 9. At alkaline pH dopamine exclusively exists in its quinone form which is an excellent electron acceptor. Binding of fluoride ion on BNSCQD stops electron transfer process and hence the fluorescence is regained. To investigate the response time of the sensor towards fluoride ion we measured fluorescence intensity as a function of time in the concentration range 20 pM to 1µM upon addition of fluoride ion. The fluorescence intensity reached a maximum value after 30 min and reaches plateau after 45 mins (Fig. 8b). Even at longer incubation time there is no decay in fluorescence signal.

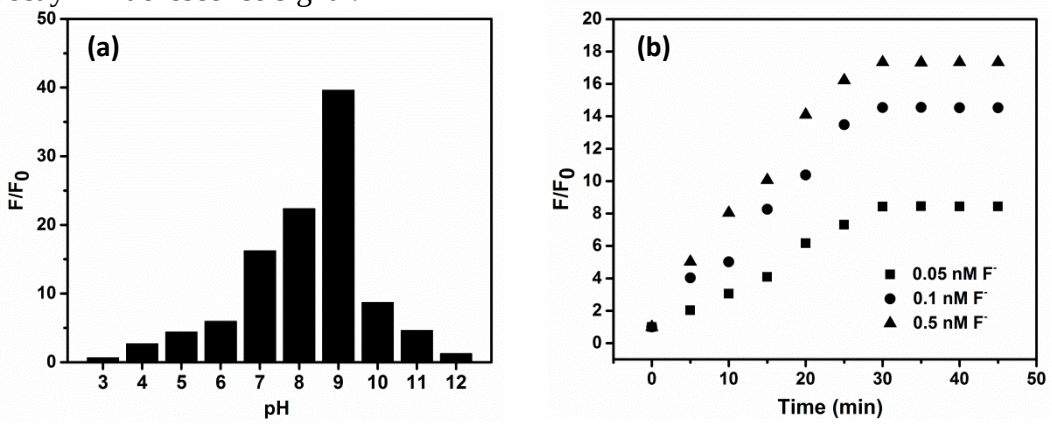

Fig. 8 (a) Pl turn-on intensity of BNSCQD-DOPA upon addition of fluoride at different pH (b) response time

Selectivity

The selectivity of fluoride is further examined in presence of other cations and anions. Fig 9a shows the increase in fluorescence intensity of BNSCQD-dopamine probe in presence of different anions. Out of all anions tested addition of fluoride gives remarkable gain in FL response whereas other anions lead to weaker fluorescence recovery verifying the outstanding selectivity of BNSCQD-dopamine towards F-. Even the presence of the ions such as Cl-, Br-, I-, HCO_3^-, CH_3COO^-, CO_3^{2-}, HPO_4, NO_3^-, SO_4^{2-} at higher concentration (0.5 nM) has little interference on fluorescence recovery by fluoride anion (Fig. 9b. Highest selectivity of our probe towards fluoride over other probes can be attributed to the highest lewis basicity of the F^- anion over other anions and smallest radius of F- ions facilitating strong binding of fluoride with boron atom of our probe forming boron trifluoride. (Scheme1).

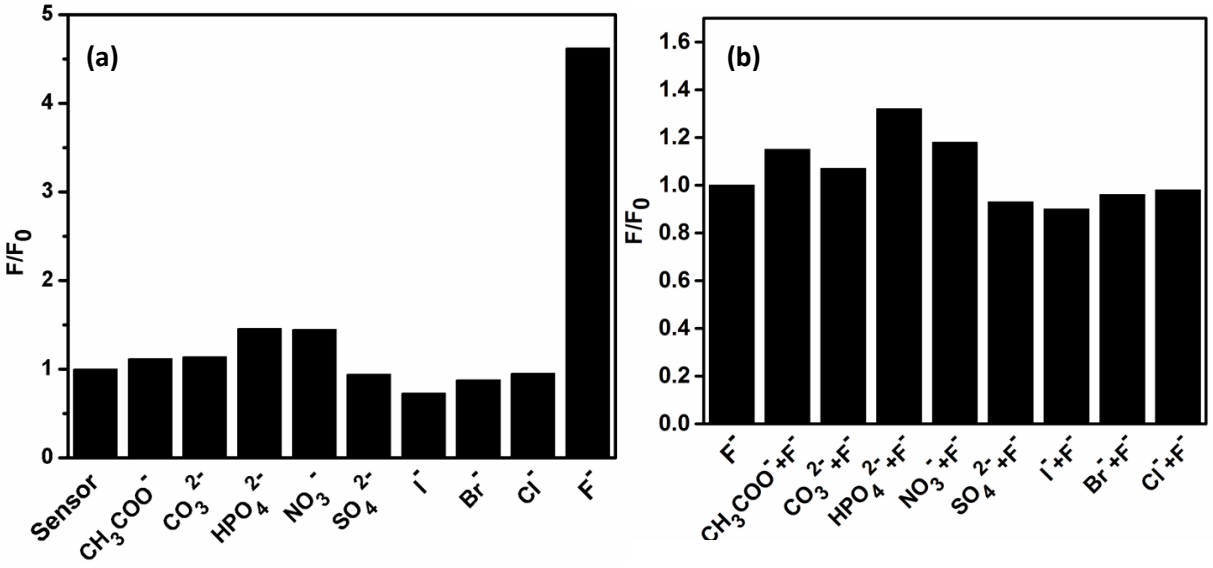

Fig. 9 (a) Fluorescence turn-on intensity of BNSCQD-DOPA probe in presence of fluorides and other anions (b) Effect of other anions presence on FL turn-on intensity of fluoride.

Binding of fluoride on BNSCQD

To verify the above hypothesis we studied the XPS binding energies of fluorinated BNSCQD. The survey spectrum XPS supports the binding of fluoride ion on the surface of BNSCQD. Fig 6a presents the XPS survey spectrum of BNSCQD having peaks at 160–170, 188–203, 284–292, 398–406, 534 and 682-684 eV which correspond to the binding energies of S2p, B1s, C1s, N1s, O1s and F1s with their atomic percentages 0.26, 3.41, 81.61, 0.61 and 3.88 respectively. In Fig 6b, F1s core-level peaks appear at 684.1 and 685.3 eV, which are assigned to the semi-ionic CF and BF_2 bonds respectively. Deconvolution of the B1s region (Fig. 10) indicates three peaks at 190.2, 192 and 196.8 eV representing BC_2O, BCO_2 and BF

bonds. The high resolution scan of B1s region indicates that larger fraction of boron has participated in the formation of BF bond in presence of fluoride ion. The high resolution scan at the N1s region (Fig. 10d) can be fitted into four peaks at 398.1, 399.4 and 400.1 eV indicating the presence of pyridinic N–H as well as pyrrolic nitrogen in the CQDs. The average life time of the exciton of BNSCQD fluorophore is 6.5 ns. Addition of dopamine even at low concentration (500 nM) to BNSCQD shortens its PL life time to 3.2 ns. Addition of fluoride increases PL life time to 4.8 ns (Fig.11).

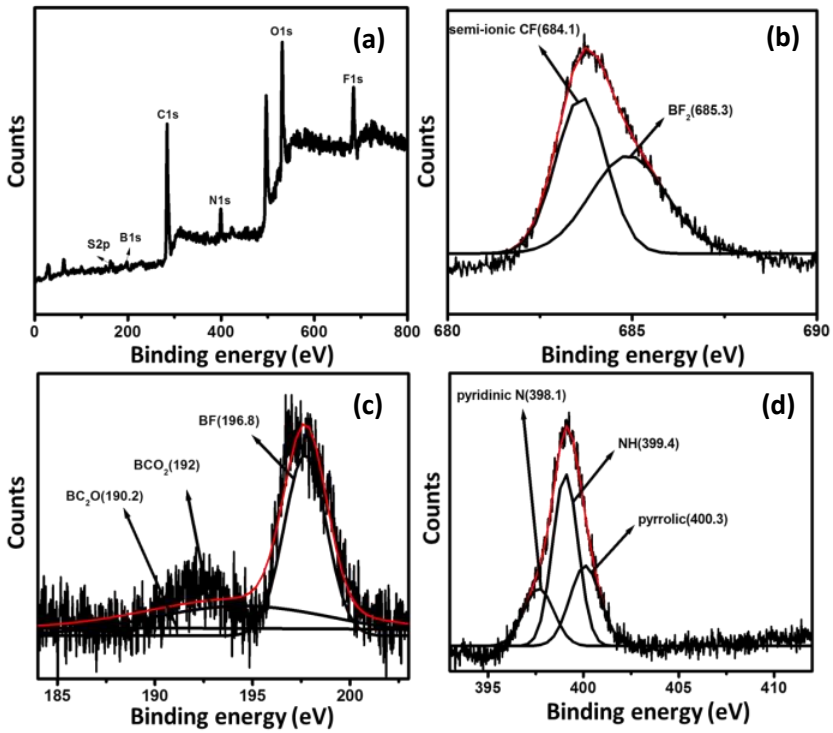

Fig. 10 XPS survey spectrum of fluorinated BNSCQD, (b), (c) and (d) are high resolution scans of F, B and N binding energy region.

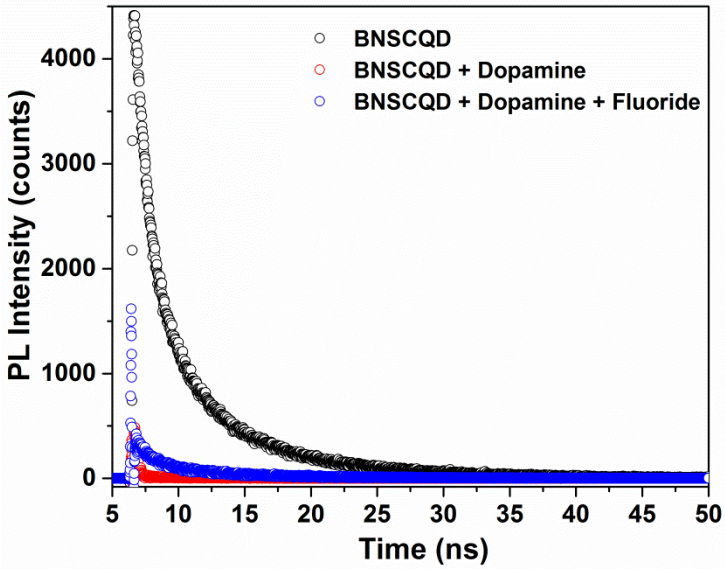

Fig. 11 Comparison of excited state fluorescence life time of BNSCQD, BNSCQD-dopamine, BNSCQD-F

Fluoride sensing in real samples

To evaluate the efficiency of this sensing system in real samples, we verified the sensing of the fluoride ions in samples such as tap water, toothpaste and three human serum samples. As presented in table 1 the performance of the sensor is quite well in all samples. The assayed concentration of fluoride is in good agreement with added amount with a variation of recovery percentage in between 97 to 100% in water and human serum samples. In case of soda and toothpaste the recovery percentage is more due to prevalent fluorides in the samples. As per EPA the permissible limit of fluoride is 10^2 µM. With a LOD of 0.7 pM the present sensing system can be used to detect fluoride in water quality monitoring and biological system.

Table 1 Recovery percentage of fluoride assayed using BNSCQD-DOPA sensor.

Sample	**Added F^- (pM)**	**F^- from assay**	**(pM) Recovery %**
Tap water	110.7	108	97.1
	222.07	217	97.6
Soda water	110.7	117	105.2
	222.07	233	104.7
toothpaste	110.7	128	115.3
	222.07	260	117.2
Human Serum 1	110.7	107	96.6
	222.07	219	98.8
Human Serum 2	110.7	110	99.5
	222.07	218	98.3
Human Serum 3	110.7	114	103.3
	222.07	224	100.7

Table 2 Comparison of performances of different graphene oxide/CD based fluoride sensors.

Sensor	LOD (x 10^6 pM)	Linear Range (x 10^6 pM)	Reference
PEG-FITC-Si	1	0 - $1x10^3$	37
GO/FC-A	0.3	2 - 90	38
Carbon dot	110	0 - $2.67x10^4$	23
Fe_3O_4@SiO_2@CQD	0.06	1 - 20	39
GO-Fe(III)	$1x10^{-6}$	0 - 1800	40
CDTe-MPA-QD-Eu^{+3}	265	0 - 2650	27
Cd-Au-Ca^{+3}	21	0 - 450	41
BNSCQD -dopamine	$0.76x10^{-6}$	$0.01x10^{-3}$ - $5x10^{-3}$	present work

Imaging of Fluoride ion in living cells

The cytotoxicity of the BNSCQD-dopamine nanosensor was evaluated in HT29 cells by MTT assay (Fig 12A). It was observed that in our experimental condition there 22% drop in cell viability after 72h of incubation. Hence, the sensor is nontoxic and biocompatible and can be explored for bioimaging of F^- inside the living cell. In the absence of fluoride ion hardly any green fluorescence was observed under excitation at 488 nm. However, when the cells were supplemented with different concentrations of fluoride, the green signal surrounding the nuclear region becomes prominent. Further with increase in fluoride concentration the intensity of the green signal increases indicating the ability of our nanoprobe to show turn-on behavior in the presence of fluoride (Fig. 12B).

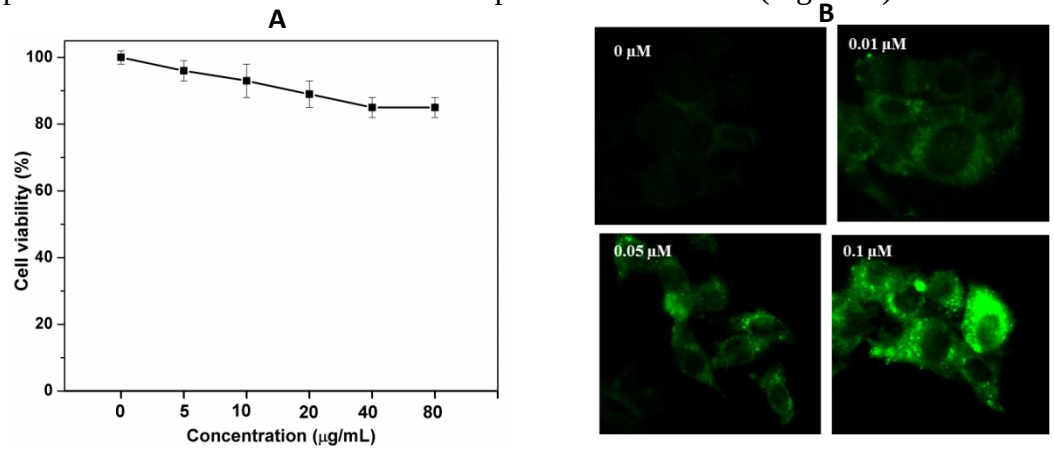

Fig. 12 (A) Cell viability in HT29 cells , (B) Fluorescence imaging of HT-29 cells incubated with 0, 0.01, 0.05, and 0.1 µM NaF for 30 min at 37ºC under 5% CO_2.

3.4 Conclusion

In this chapter,

- We have successfully developed a heteroatom doped carbon quantum dot integrated with dopamine probe for selective and sensitive detection of fluoride probe in purely aqueous medium.
- The intense fluorescence intensity of CQD is quenched due to photo induced electron transfer by dopamine.
- Addition of fluoride enhanced fluorescence intensity due to interruption in PET as well as contribution of extra lone pair of electron to CQD network.
- This CQD sensor was successfully used in real samples and human serum samples. Cellular toxicity test showed that BNSCQD possess low toxicity.
- Our fluorescence sensor can efficiently be used to monitor fluoride contamination inside the cell.

3.5 References

1. P. Adler, *Fluorides and Health*, World Health Organization Geneva **1970**; b) E.W. Rice, R. B. Baird, A. D. Eaton, L. S. Clesceri, Standard Methods for the Examination of Water and Wastewater, American Public Health Association, *American Water Works Association*, Water Environment Federation **1998**.
2. S. Jagtap, M. K. Yenkie, N. Labhsetwar and S. Rayalu, *Chem. Rev*., 2012, **112**, 2454-2466.
3. B. Pan, J. Xu, B. Wu, Z. Li and X. Liu, *Environ. Sci. Tech*., 2013, **47**, 9347-9354.
4. Y. Zhou, J. F. Zhang and J. Yoon, *Chem. Rev*., 2014, **114**, 5511-5571.
5. Y. Li, Y. Duan, J. Zheng, J. Li, W. Zhao, S. Yang and R. Yang, *Anal. Chem*., 2013, **85** 11456-11463.
6. B. Sui, B. Kim, Y. Zhang, A. Frazer, K. D. Belfield, *ACS Appl. Mater. Interfaces*, 2013, **5**, 2920-2923.
7. J.D.B. Featherstone, *Commun. Dent. Oral Epidemiol*., 1999, **27**, 31-40.
8. J. Yao, M. Yang and Y. Duan, *Chem. Rev.*, 2014, **114**, 6130-6178.
9. O. S. Wolfbeis, *Chem. Soc. Rev*., 2015, **44,** 4743-4768.
10. P. M. Basha and S. M. Saumya, *Cell Mol Neurobiol*., 2013, **33**, 453-464.
11. R. Blaylock, *Fluoride*, 2004, **37**, 301-314.

12. P. Li, Y. P. Xue, W. B. Zhang, F. Teng, Y. Sun, T. J. Qu, X. X. Chen, X. G. Cheng, B. Song, W. J. Luo and Q. Yu, *Toxicology*, 2013, **308**, 138-145.
13. S. Zhang, J. Fan, S. Zhang, J. Wang, X. Wang, J. Dua and X. Peng, *Chem. Commun*., 2014, **50,** 14021-14024.
14. A. B. Chinen, C. M. Guan, J. R. Ferrer, S. N. Barnaby, T. J. Merkel and C. A. Mirkin, *Chem. Rev*., 2015, **115**, 10530-10574.
15. X. Wu, X. X. Chen, B. N. Song, Y. J. Huang, W. J. Ouyang, Z. Li, T. D. James and Y. B. Jiang, *Chem. Commun*., 2014, **50**, 13987-13989.
16. V. M. Suresh, A. Bandyopadhyay, S. Roy, S. K. Pati and T. K. Maji, *Chem. Eur. J*., 2015, **21**, 10799-10804.
17. X. Chen, S. Yu, Liang Yang, J. Wang and C. Jiang, *Nanoscale*, 2016, **8**, 13669-13677.
18. G. Jha, N. Anoop, A. Rahaman and M. Sarkar, *Phys. Chem. Chem. Phys*., 2015, **17**, 3525-3533.
19. T. K. Mandal, Y. Hou, Z. Gao, H. Ning, W. Yang and M. Gao, *Adv. Sc*., 2016, 1600217-1600223.
20. Y. Jiao, B. Zhu, J. Chen and X. Duan, *Theranostics*, 2015, **5,** 173-187.
21. M. Bineci, M. Baglan and S. Atılgan, *Sens. Actuators B*, 2016, **222**, 315-319.
22. P. Singhal, B. G. Vats, S. K. Jha and S. Neogy, *ACS Appl. Mater. Interfaces*, 2017, **9**, 20536-20544.
23. M. Shamsipur, A. Safavi, Z. Mohammadpour and A. R. Zolghadr, *Sens. Actuators B*, 2015, **221**, 1554-1560.
24. C. Ding, A. Zhu and Y. Tian, *Acc. Chem. Res*., 2014, **47**, 20-30.
25. Q. Xu, T. Kuang, Y. Liu, L. Cai, X. Peng, T. S. Sreeprasad, P. Zhao, Z. Yue and N. Li, *J. Mater. Chem. B*, 2016, **4**, 7204-7219.
26. S.Y. Lim, W. Shen and Z. Gao, *Chem. Soc. Rev*., 2015, **44**, 362-381.
27. X. Chen, S. Yu, L. Yang, J. Wang and C. Jiang, *Nanoscale*, 2016, **8**, 13669-13677.
28. R. K. Das and S. Mohapatra, *J. Mater. Chem. B*, 2017, **5,** 2190-2197.
29. S. T. Yang, X. Wang, H. Wang, F. Lu, P. G. Luo, L. Cao, M. Meziani, J. H. Liu, Y. Liu, M. Chen, Y. Huang and Y. P. Sun, *J. Phys. Chem. C*, 2009, **113**, 18110-18114.
30. S. Mondal, M. Chatti, A. Mallick and P. Purkayastha, *Chem. Commun*., 2014, **50**, 6890-6893.
31. Y. Li, Y. Xie and Y. Qin, *Sens. Actuators B*, 2014, **191**, 227-232.

32. M. Zhong, Y. Teng, S. Pang, L. Yan and X. Kan, *Biosens. Bioelectron*., 2015, **64**, 212-218.

33. J. L. Chen, X. P. Yan, K. Meng and S. F. Wang, *Anal. Chem.*, 2011, **83**, 8787-8793.

34. I. L. Medintz, M. H. Stewart, S. A. Trammell, K. Susumu, J. B. Delehanty, B. C. Mei, J. S. Melinger, J. B. B. Canosa, P. E. Dawson and H. Mattoussi, *Nat. Mater*., 2010, **9**, 676-684.

35. S. Mohapatra, S. Sahu, N. Sinha and S. K. Bhutia, *Analyst*, 2015, **140**, 1221-1228.

36. F. Zheng, F. Zeng, C. Yu, X. Hou and S. Wu, *Chem. Eur. J*., 2013, **19**, 936 -942.

37. C. Wang, S. Yang, M. Yi, C. Liu, Y. Wang, J. Li, Y. Li, R. Yang, *ACS Appl. Mater. Interfaces*, 2014, **6**, 9768-9775..

38. S. Mohapatra, S. Sahu, S. Nayak, S. K. Ghosh, *Langmuir*, 2015, **31**, 8111-8120.

39. P. Singh, A. A. Prabhune, C. S. P. Tripathi, D. Guin, *ACS Sus. Chem. Eng*., 2017, **5**, 982-987.

40. X. Tian, J. Wang, Y. Li, C. Yang, L. Lu and Y. Nie, *Sens. Actuators B*, 2018, **262**, 522-530.

Chapter – 4

Magnetic Mesoporous Silica Gated with Doped Carbon Dot for Site-Specific Drug Delivery, Fluorescence, and MR Imaging

4.1 Introduction

In 2006, National Institute of Health has coined the term "nanomedicine" which precisely means nanoparticle-based therapeutics composed of a variety of organic or inorganic nanomaterials for treatment, diagnosis, and control of diseases like cancer.[1,2] Stemming from the integrated concept of nanotechnology with molecular biology and medicine, nanoparticle-based drug formulations have been proved as a powerful tool for imaging, diagnosis, and therapy.[3-5] Among various nanomaterials reported for medical applications, mesoporous silica (MS)-based nanosystems provide a unique opportunity to constitute a robust nanocontainer for the encapsulation of therapeutic cargoes. The porous framework of MS allows the inorganic platform to house appreciable amounts of cargoes without destabilization of the silica framework. At the same time, the chemical functionalization with different organic molecules can allow diffusion-controlled drug release under specific conditions.[6-8] The ability of mesoporous channels to regulate the molecular transport functions will be greater if they are equipped with a switchable gating mechanism. The gate opens on application of an external stimulus such as light, pH, changes in redox potential, and so forth.[9] The pioneering work in the field of gated nanosystem consisting of MS and supramolecular nanovalves was reported by Stoddart and Zink, where the authors have used β-CD as a valve to constitute mechanized MS.[10-12] Following this work, a range of stimuli-responsive drug delivery systems have been designed by grafting various materials on the surface of the MS as "gate keeper" including polymers,[13] magnetic nanoparticles, [14] quantum dots,[15] and metal nanoparticles[16] to prevent premature drug release and regulate molecular transport properties. These bulky groups/particles serve as gatekeepers for the encapsulated cargo. The removal of the bulky blocking groups via cleavage of chemical bonds initiates the cargo release. However, in such molecular machines, sometimes all pores are not covered perfectly which results in nonuniform drug loading and unpredictable drug release. To overcome such technical problems, nanovalves can be used where the cap is attached through a noncovalent interaction such as electrostatic interaction, hydrogen bonding, donor−acceptor, and ion−dipole interaction so that the drug release can be precisely controlled upon the application of external stimuli.

On the other hand, early diagnosis and effective treatment of cancer remains challenging because of the lack of prompt diagnostic and therapy technology.[17,18] Hence, targeted fluorescent biomarkers have found great utility in the specific visualization of cancer cells, which enables early-stage detection of cancers instead of relying on advanced

morphological changes alone.[19-21] Recently carbon quantum dots are rising stars in the field of biosensing and bioimaging because of their excellent luminescence property, photostability, biocompatibility, and water solubility.[22-26] Moreover, the unique property of multicolour emission offers many visible advantages in bioimaging and has been proved as a suitable alternative for heavy metal-based quantum dots.[27-30] However, the development of targeted imaging agents by tethering marker molecules on to the surface of carbon dots still remains challenging for constructing a perfect "smart" theranostic agent, which can be served as a multiple functional platform integrating imaging and targeting capabilities.[31-34] In this context, there are very few reports on self-targeted carbon quantum dots. Sun et al. have synthesized CD-Asp from glucose and L-aspartic acid which has targeting capacity toward brain cancer glioma.[35] Very recently, our research group has reported the self-targeting fluorescence imaging capacity of boronic acid-modified B-, N-, S-doped carbon quantum dots toward liver cancer cells.[36] However, in addition to targeted imaging, these functional CQD can be incorporated into a carrier matrix to avail multiple facilities from a single construct and only a few literature studies are available in this direction.[37-40] Designing such hybrids would offer multiple applications. Furthermore, in addition to fluorescence imaging, other imaging modalities can be incorporated into the MS matrix. For example, nowadays T1-T2 dual-mode contrast agents have attracted increasing attention in the magnetic resonance imaging technique. Such types of contrast agents have the ability to acquire complementary and self-confirmed information and hence reliable interpretation of data.[41-44]

In this chapter, we have developed gadolinium oxide-iron oxide (GdIO) core@mSiO2@BNSCQD nanoparticles as a carrier for anticancer drug 5-fluorouracil (5-Fu) and simultaneous fluorescence as well as MR imaging. We anticipate that GdIO@mSiO2 nanoparticles act as a carrier for anticancer drug 5-Fu and a T1/T2 dual contrast agent, and at the same time, BNSCQD capped at the mesochannel plays multiple roles such as (1) directing the nanodrug toward the cancer cells overexpressed with sialyl Lewis^a (SL^a), (2) gate-keeping agent for the mesoporous vehicle, and (3) switching on the fluorescence signal at the target site when the drug is released. This novel nano system is the first report amalgamating a combination of MS nanoparticle-based drug delivery system where pH and cell surface receptor-responsive targeted fluorescence and MR imaging moieties are integrated into one system.

2.2 Experimental

Chemicals

Gadolinium(III) 2,4-pentanedionate, iron(III) acetylacetonate, oleyl amine, and 1,2-dodecanediol, trimethoxy3-aminopropyl silane (APTS) benzyl ether have been procured from Sigma-Aldrich. Cetyl-trimethylammonium bromide (CTAB) was procured from Spectrochem, India. All other reagents and solvents were used without further purification. Millipore water (18.2 MΩ cm) was used throughout the experiment. Synthesis of GdIO Nanoparticles. GdIO nanoparticles were synthesized through the solvothermal method. Briefly, iron(III) acetylacetonate (353 mg, 1 mmol), gadolinium(III) 2,4-pentanedionate hydrate (54 mg, 0.1 mmol), oleyl amine (0.6 mL), oleic acid (0.6 mL), 1,2-dodecanediol (300 mg), and benzyl ether (15 mL) were mixed and stirred for 15 min at room temperature. Then, the total mixture was transferred to a Teflon-lined stainless steel autoclave and heated for 10 h at 190 °C. After cooling to room temperature, excess ethanol was added to precipitate the nanoparticles. The product was collected using a magnetic separator, washed using ethanol, and dried in a vacuum desiccator.

Synthesis of GdIO@SiO_2

Oleic acid-stabilized monodisperse GdIO nanoparticles (7.5 mg) dispersed in 0.8 mL of chloroform were added to 5 mL of aqueous solution containing 0.1 g of CTAB. After vigorous stirring for 25 min, the microemulsion was heated at 70 °C for 40 min to induce evaporation of chloroform in the solution, which generated aqueous phase +dispersed nanoparticles. The resulting aqueous solution (0.5 mL) was diluted with 10 mL of deionized water. Then, 0.3 mL of NH_4OH solution and 0.05 mL of tetraethylorthosilicate were successively added to the diluted aqueous solution containing the GdIO nanoparticles. The resulting mixture was stirred for 30 min, and then aged overnight. The precipitate was collected by centrifugation and thoroughly washed with water and ethanol. Finally, GdIO nanoparticles embedded in silica spheres (GdIO@SiO_2) were dried in hot air oven at 50 °C overnight.

Synthesis of Amine Modified GdIO@mSiO_2

The exterior surface of GdIO@SiO_2 mesoporous particles was modified with amine groups using APTS. GdIO@SiO_2 (100 mg) spheres were refluxed in 30 mL dry toluene containing 0.3 mL of APTS under N_2 atmosphere for 24 h. Then, the amine-modified GdIO@SiO_2

particles were washed with acidic ethanol to remove CTAB. After the removal of the surfactant, the sample is named amine-modified GdIO@$mSiO_2$ nanospheres.

Synthesis of GdIO@$mSiO_2$@BNSCQD

BNSCQD was synthesized hydrothermally as per our recently published paper.36 The amine-modified GdIO@$mSiO_2$ nanospheres (20 mg) were dispersed in 20 mL of phosphate-buffered saline, and the solution was sonicated for 2 min. Ten millilitres of BNSCQD (10 μg/mL) solution was added to functionalize GdIO@$mSiO_2$. The mixture was stirred at room temperature for 6 h followed by centrifugation, washing with phosphate-buffered saline several times. The free BNSCQD in the supernatant were estimated by measuring the PL spectrum (λ_{ex} = 420 nm).

5-Fu Loading and Release

The amine-modified GdIO@$mSiO_2$ (20 mg) was first incubated in phosphate-buffered saline (10 mM, 25 mL, pH 7.4) of 5-Fu (25 mg) for 24 h at room temperature. The particles were centrifuged, washed with PBS buffer, and dried under high vacuum to produce the 5-Fu loaded nanoparticles. The drugloaded GdIO@$mSiO_2$ particles were sealed with boronic acid functionalized carbon quantum dot (BNSCQD) by mixing BNSCQD (10 μg/mL) with the 5-Fu loaded nanoparticles (36 μg/mL) in phosphate-buffered saline (10 mM, pH 7.4). The solution was stirred for 6 h, followed by centrifugation and repeated washing with phosphate-buffered saline (10 mM, pH 7.4). The BNSCQD-capped GdIO@mSiO2 loaded with 5-Fu was then dispersed in 25 mL of phosphate-buffered saline at different pH (4.3, 5.5, and 6.8). The release of the drug and carbon dot were monitored for 96 h. Aliquots were taken from the suspension, and the amount of 5-Fu was examined by UV spectroscopy (λmax = 266 nm) and the release of BNSCQD was examined by the PL spectrum (λex = 420, λem = 490nm).

Cytotoxicity Assays

HepG2, PC3, and 3T3 cells (3×10^3 cells) were seeded separately into 96-well plates and incubated in 200 μL Dulbecco's modified Eagle's medium (DMEM) containing 10% FBS for 24 h (37 °C, 5% CO_2). After incubation, cells were treated with different concentrations of GdIO@$mSiO_2$@BNSCQD and 5-Fu@GdIO@$mSiO_2$@BNSCQD (0.5, 5, 10, 20, 50, 100, and 200 μg/mL) in fresh DMEM without serum for another 24 h. Following treatment, cells were washed with 1× PBS, and 100 μL of MTT solution (1 mg/mL in PBS buffer) was added to each well. After 3 h of incubation, MTT solution was removed and replaced with 200 μL

of DMSO. Absorbance was read at 570 nm using a microplate reader. The experiment was performed three times independently.

In vitro Imaging Studies

Cells (3×10^4) were seeded separately into 24-well plates and incubated in 400 μL of DMEM containing 10% FBS and 1% antibiotic (penicillin, streptomycin) at 37 °C inside the incubator with 5% CO_2. After 24 h of incubation, media were removed and replaced with fresh DMEM without the serum containing samples 1, 2, and 3 separately at concentration 30 μg/mL. After incubation for 3 h, the media were removed and washed with 1× PBS three times. Thereafter, the cells were fixed with 2% paraformaldehyde (PFA) for 15 min at RT followed by washing with 1× PBS and viewed under fluorescence (Leica) with excitation at 405, 488, and 546 nm.

Characterization

The phase formation and crystallographic state of the as-synthesized material were studied using an Expert Pro Phillips X-ray diffractometer. The morphology, microstructural analysis, and elemental mapping were performed using a scanning electron microscope (SEM; Hitachi COM-S-4200) and a high resolution transmission electron microscope (HRTEM; FEI TechnaiG2 30ST) operated at 300 kV. The magnetic properties of GdIO@mSiO_2@BNSCQD and GdIO@mSiO_2 nanospheres were determined using a SQUID-VSM instrument (EverCool SQUID VSM DC Magnetometer) at 25.0 ± 0.5 °C. Nitrogen adsorption−desorption isotherms were measured at a liquid nitrogen temperature (77 K) using a Quantachrome surface area analyser. The specific surface areas and total pore volume were calculated by the Brunauer−Emmett−Teller (BET) and BJH methods, respectively. The mean hydrodynamic sizes were measured by laser light scattering using a particle size analyser (Nano ZS90, Malvern). The surface composition of the drug-loaded particles was investigated by analysing X-ray photoelectron spectroscopy (XPS) data using an Al Kα excitation source in a PHI 5000 VersaProb II (FEI Inc.) instrument. The Raman spectrum of as-prepared samples was recorded on a Renishaw inVia Raman spectrometer (UK model). UV absorption measurements were carried out on a Shimadzu 220 V (E) UV−vis spectrophotometer to measure the 5-Fu and BNSCQD concentrations. Photoluminescence spectra were collected on a Horiba Quantamaster fluorimeter. The T1 and T2 relaxation times of the nanoparticle were measured using a clinical magnetic resonance imaging (MRI) scanner (MAGNETOM

Symphony, Siemens) at a magnetic field of 1.5 T. Live-cell images were captured under a Leica TCS SP8 confocal microscope with laser excitations at 405, 488, and 546 nm.

DAPI Staining for Nuclear Morphology

HepG2, PC3, and 3T3cells were seeded separately into 24-well plates and incubated in 400 μL DMEM containing 10% FBS and 1% antibiotic (penicillin, streptomycin) at 37 °C inside the incubator with 5% CO2. After 24 h of incubation, cells were treated with 30 μg/mL of the sample in DMEM without serum and further incubated for different time periods (0.5, 1, 2, 4, and 6 h). Then, the cells were fixed with 2% PFA followed by washing with 1× PBS. To observe the nuclear changes inside the cell, 0.5 μg/mL of DAPI was added to each well. Cells were examined under a confocal microscope (Olympus).

Relaxometric Measurements

The relaxation time (T1) of GdIO@mSiO2@BNSCQD NPs were measured with varying the Gd concentration (0.02−0.1 mM) using a clinical MRI scanner (MAGNETOM Symphony, Siemens) at a magnetic field of 1.5 T. T1-weighted 2D-spin echo sequence (T1-trim software) was used to image GdIO@mSiO2@BNSCQD in various media. The repetition time (TR) was fixed at 6000 ms with echo times (TE) ranging from 244 to 3000 (244, 350, 450, 700, 1200, 2400, and 3000). The flip angle was maintained at 150°, and the band width was maintained at 100 Hz. The spatial resolution parameters were as follows: field of view (FOV) = 340 × 340 mm2, matrix = 256 × 256, and slice thickness = 3.0 mm. T2-weighted images were obtained with a spin echo multisection pulse sequence having fixed TR of 4000 ms with various echo times (TE) ranging from 105 to 291 (105, 116, 128, 139, 151, 163, 174, 186, 198, and 291). The spatial resolution parameters were as follows: FOV = 340 × 340 mm2, matrix = 256 × 256, and slice thickness = 3.0 mm. The MRI signal intensity (SI) was measured using in-built software. T2 values were obtained by plotting the SI of each sample over a range of TE values. T2 relaxation times were then calculated by fitting a first-order exponential decay curve to the plot. The fitting equation can be expressed as

$SI = S\, e^{-TT} + B$ and $SI = S\, e^{-TT} + B$

where SI is the signal intensity, TE is the echo time, S0 is the amplitude, and B is the offset. The relaxivity values r2 and r1 were determined from the slope of the linear plots of the relaxation rate R2 (1/T2, s^{-1}) against Fe concentrations (mM) and relaxation rate R1 (1/T1, s^{-1}) against Gd concentrations (mM).

$R_2 = R_2^0 + r$[Fe] and $R_1 = R_1^0 + r$[Gd]

2.3 Results and discussion

As shown in Figure 1, the GdIO core is coated with a MS shell which acts as a nanoreservoir for anticancer drug 5-Fu. The outermost surface of MS is functionalized with 3-aminopropyltrimethoxy silane to generate surface amine groups. The negatively charged BNSCQD were anchored to the openings of aminopropyl group-functionalized MSPs through electrostatic interaction and are utilized as caps for trapping the guest molecules within the pores. When partially ionized carboxylic acid or boronic acid, species on the C-dots were transformed into protonated groups (COOH) at low pH, C-dots are released from the surface of the MS container, leading to the opening of the gates and hence releasing the anticancer drug. The availability of cell surface glycan SLa is much higher in liver cancer cells (HepG2) than noncancerous cells. Thus, upon coming in contact with SLa at acidic pH (4−5), the BNSCQDs are released and attached to SLa receptorbecause of the interaction of boronic acid groups with cis diol. On the basis of the novel GdIO core, MS shell, and BNSCQD as gatekeeper, multiple functions such as drug delivery, T1 and T2 magnetic resonance imaging, stimuli responsive gate opening, and cell imaging are facilitated together as a proof of concept demonstration of combinatorial cancer therapy.

XRD

The synthesis of monodisperse GdIO nanoparticles has been adopted from a reported method. The XRD pattern (Fig.1) of GdIO shows four diffraction peaks at 30°, 35.4°, 43.6°, and 62.4° corresponding to reflection planes at (220), (311), (400), (440), respectively. These diffraction peaks could be indexed to cubic ferrite Fe_3O_4 having inverse spinel structure (JCPDS 82-1533). There is slight shift in peak positions because of the incorporation of Gd.

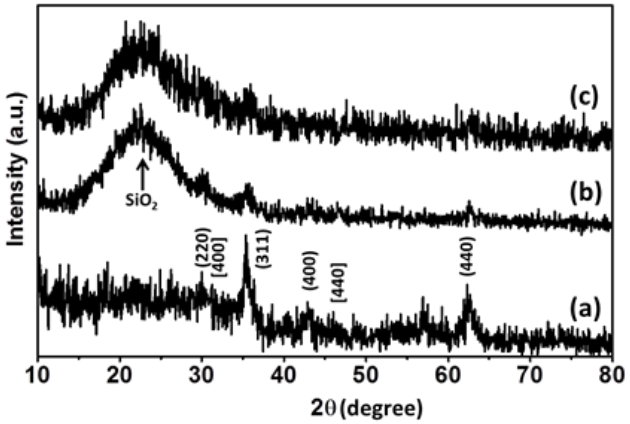

Fig. 1 XRD pattern of GdIO, GdIO@mSiO$_2$, GdIO@mSiO$_2$@BNSCQD.

TEM

TEM images show the formation of cubic Fe_3O_4 particles of size 15 nm (Fig. 2a). The HRTEM images showed that the assynthesized nanoparticles are nearly monodispersed and crystalline. The lattice fringes correspond to the cubic spinel structure of Fe3O4 (Fig. 2b). The measured lattice spacing calculated from the points in the SAED pattern represents planes from both Fe_3O_4 and Gd_2O_3 (Fig. 2c). The STEM elemental mapping shows uniform distribution of Gd throughout the Fe_3O_4 matrix (Fig. 2d). The GdIO@$mSiO_2$ core shell particle has been prepared following a sol-gel method. The oleic acid-coated GdIO were made hydrophilic by coating with CTAB as the secondary surfactant. CTAB-coated GdIO acted as a seed for the growth of the $mSiO_2$ shell. Field emission SEM (FESEM) and TEM images show that the GdIO@$mSiO_2$ is spherical, uniform, and monodisperse and has a mean average size of 40 ± 2 nm (Fig. 3a, b). From the STEM image the core-shell structure of GdIO@$mSiO_2$ is well observed (Fig. 3c). To investigate the composition of the GdIO@$mSiO_2$ structure, we conducted STEM element mapping. The results indicate that Gd and Fe are mainly collected at the core which is surrounded by Si and O shells. The outer MS shell has an average diameter 20 nm.

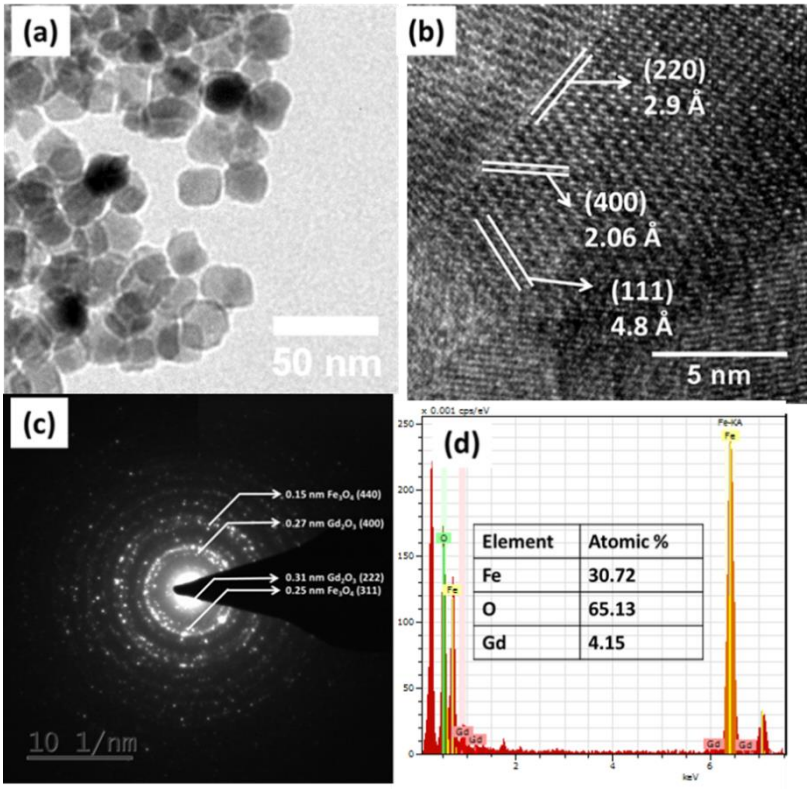

Fig. 2 TEM image of (a) GdIO, (b) HRTEM, (c) SAED pattern and (d) STEM-EDAX of GdIO.

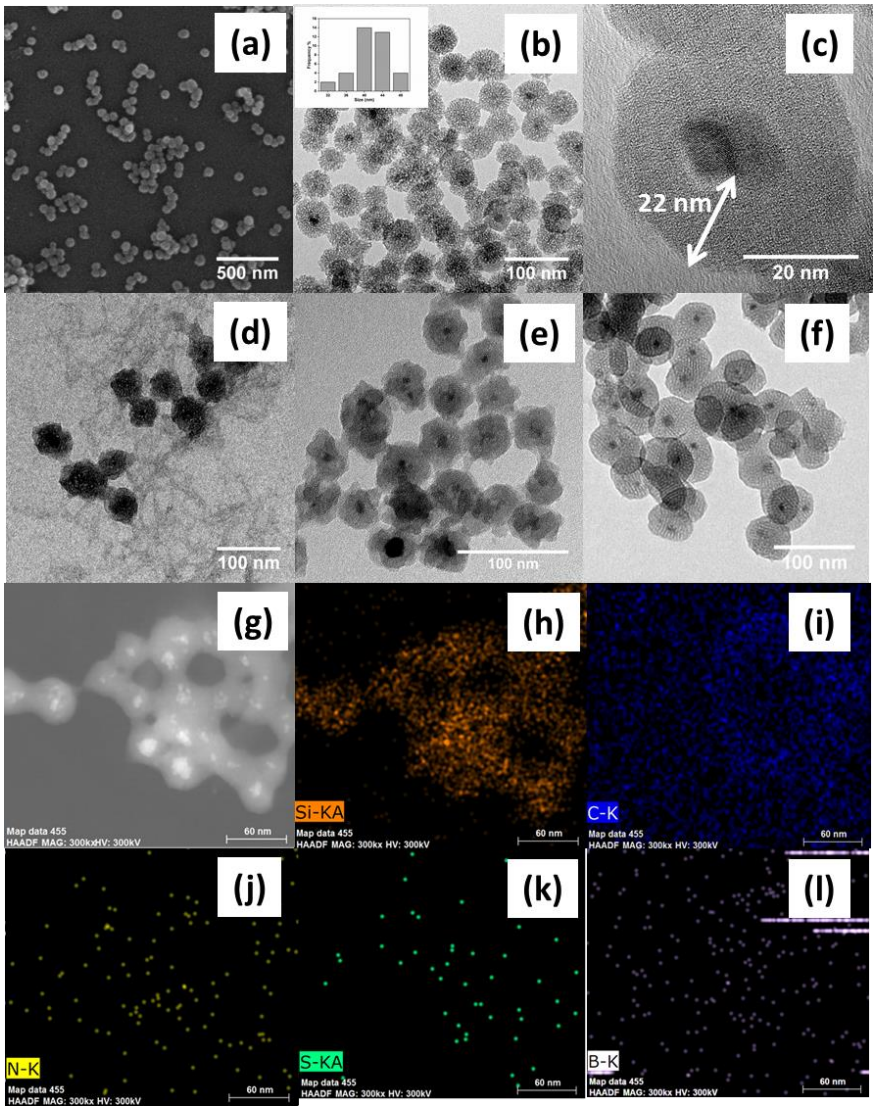

Fig. 3 (a) FESEM image of GdIO@mSiO$_2$, (b) and (c) TEM images of GdIO@mSiO$_2$, (d) and (e) TEM images of GdIO@mSiO$_2$@BNSCQD, (f) TEM images of GdIO@mSiO$_2$@BNSCQD after release of drug and BNSCQD (g) STEM image and (h)-(i) elemental mapping of GdIO@mSiO$_2$@BNSCQD.

N_2 adsorption - desorption study

Nitrogen adsorption-desorption curves of GdIO@mSiO$_2$ and GdIO@mSiO$_2$@BNSCQD are presented in Fig. 4A. Both curves present type IV isotherm which is typical of mesoporous materials. The BET surface area of GdIO@mSiO$_2$ is 410.95 m^2/g. From the BJH curve the pore diameter of GdIO@mSiO$_2$ is 3.6 nm. To realize the surface charge alteration capability of mesopores under lysosomal environment, the outermost surface is modified with amine groups; the amine-tethered GdIO@mSiO$_2$ composite was obtained by using a surface condensation of GdIO@mSiO$_2$ with APTES which has been confirmed from Fourier-transform infrared spectroscopy (FTIR) (Fig. 4B). A clear peak at 3250 cm^{-1} confirms the presence of surface amine groups. The surface amine groups were utilized to graft B, N, S-

doped carbon quantum dot (BNSCQD). The synthesis, characterization, and PL properties of BNSCQD are already discussed in chapter 2.[36]

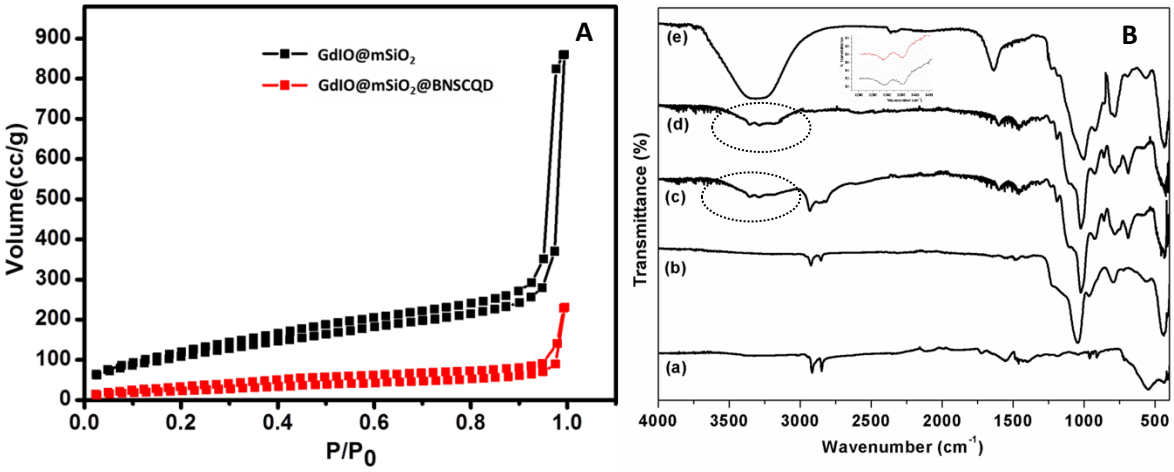

Fig. 4 A. N_2 adsorption-desorption isotherm of (a) GdIO@mSiO$_2$, (b) GdIO@mSiO$_2$@BNSCQD and B. FTIR of (a) GdIO@CTAB, (b) GdIO@CTAB@SiO$_2$, (c) GdIO@CTAB@SiO$_2$@APTES, (d) GdIO@mSiO$_2$@APTES, (e) GdIO@mSiO$_2$@APTES@BNSCQD.

Particle size and zeta potential

The mean average diameter of BNSCQD is 4.5 nm, which indicates that they are suitable enough to cap 3.6 nm pores of GdIO@mSiO$_2$. We intuitively verified the capping of the BNSCQD on GdIO@mSiO$_2$. As the surface charge of GdIO@mSiO$_2$ and BNSCQD are +24 mV and −35 mV, it is expected that BNSCQD can cap GdIO@mSiO$_2$ on the basis of electrostatic interaction. In fact zeta potential of GdIO@mSiO$_2$ drops from +24 to −15 mV after capping with BNSCQD (Fig. 5). Because of the blockage of pores after the loading of carbon dots, the surface area of GdIO@mSiO$_2$ nanoparticles decreased to 90.1 m^2/g.

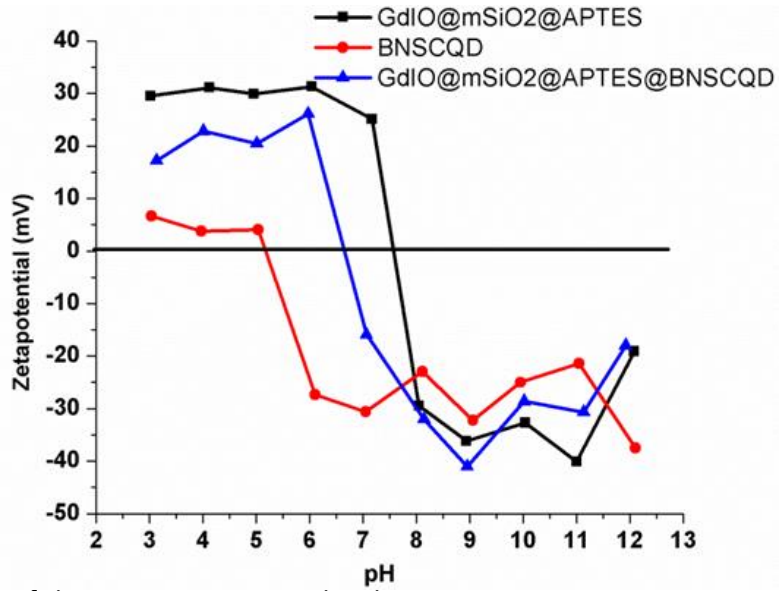

Fig. 5 Comparison of change in zeta potential with respect to pH.

The presence of BNSCQD was also confirmed from FTIR and XPS. In the FTIR (Fig. 4B), a strong peak at carbonyl region (1733-1550 cm^{-1}) indicates the presence of COOH and $-CONH_2$ which are not found in case of $GdIO@mSiO_2$. The XPS survey spectrum of $GdIO@mSiO_2$@BNSCQD shows the presence of Fe, Gd, Si, C, N, S, O, and B.

XPS analysis

The high-resolution scan of N 1s shows binding energies corresponding to three types of nitrogens such as pyridinic N (398.4 eV), pyrrolic (399.6 eV), and NH^{3+} (401.3 eV) (Fig. 6). Furthermore, the high-resolution scan of C 1s shows binding energies corresponding to five types of carbon such as C-B (284.1 eV), sp^2 carbon of graphene (285.2 eV), sp^3 C−S, C−N, C−O (285.7 eV), C=O (286.4 eV), and O−C=O (288.4 eV). The quantification of BNSCQD on $GdIO@mSiO_2$ was accomplished from thermogravimetric analysis which corresponded to a maximum immobilization efficiency of approximately 32 mg/g.

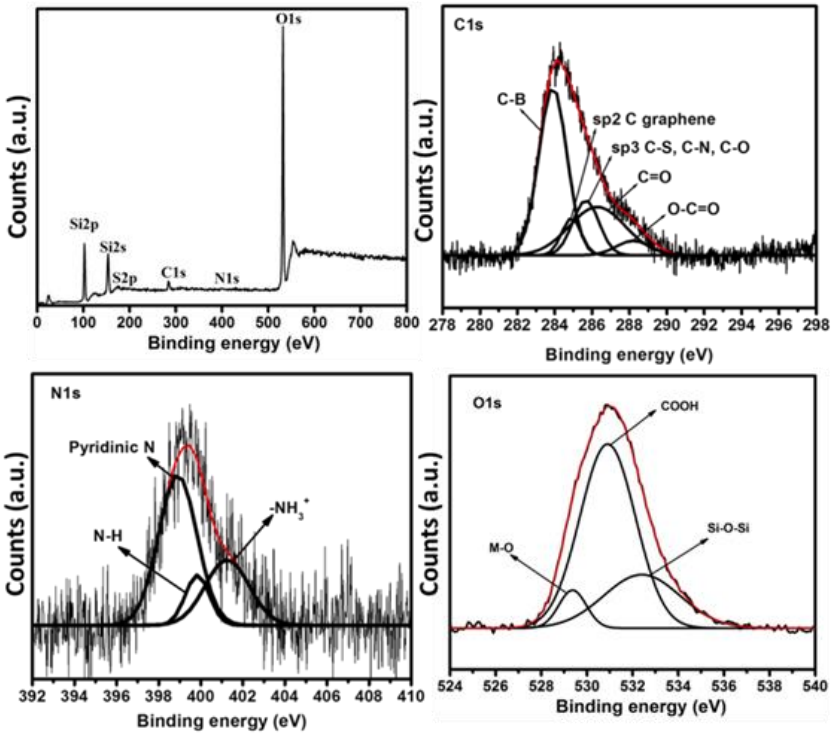

Fig. 6 XPS of $GdIO@mSiO_2$@ BNSCQD (a) survey, (b) C1s, (c) N1s and (d) O1s.

Photoluminescence study

Fig. 7a shows a comparison of the fluorescence spectra of $GdIO@mSiO_2$ and $GdIO@mSiO_2$@BNSCQD at λ_{ex} 340 nm. In case of $GdIO@mSiO_2$@BNSCQD, there is a strong fluorescence signal in between 370 and 500 nm which originates from BNSCQD, whereas in the case of uncapped $GdIO@mSiO_2$ a fluorescence signal of negligible intensity is

observed in that region because of the presence of Gd in the core. It was well demonstrated in chapter 2 that the incorporation of N and S in BNSCQD enhances luminescence properties via the introduction of new types of surface states which facilitate a high yield of radiative recombination. In addition GdIO@mSiO$_2$@BNSCQD also shows fluorescence when excited at the NIR region (Fig. 7b). The PL quantum yield of BNSCQD is 24%, whereas that of the GdIO@mSiO$_2$@BNSCQD nanostructure is 18.7%. Both samples BNSCQD and GdIO@mSiO$_2$@BNSCQD emit an intense green signal when excited under UV light (Figure 5c).

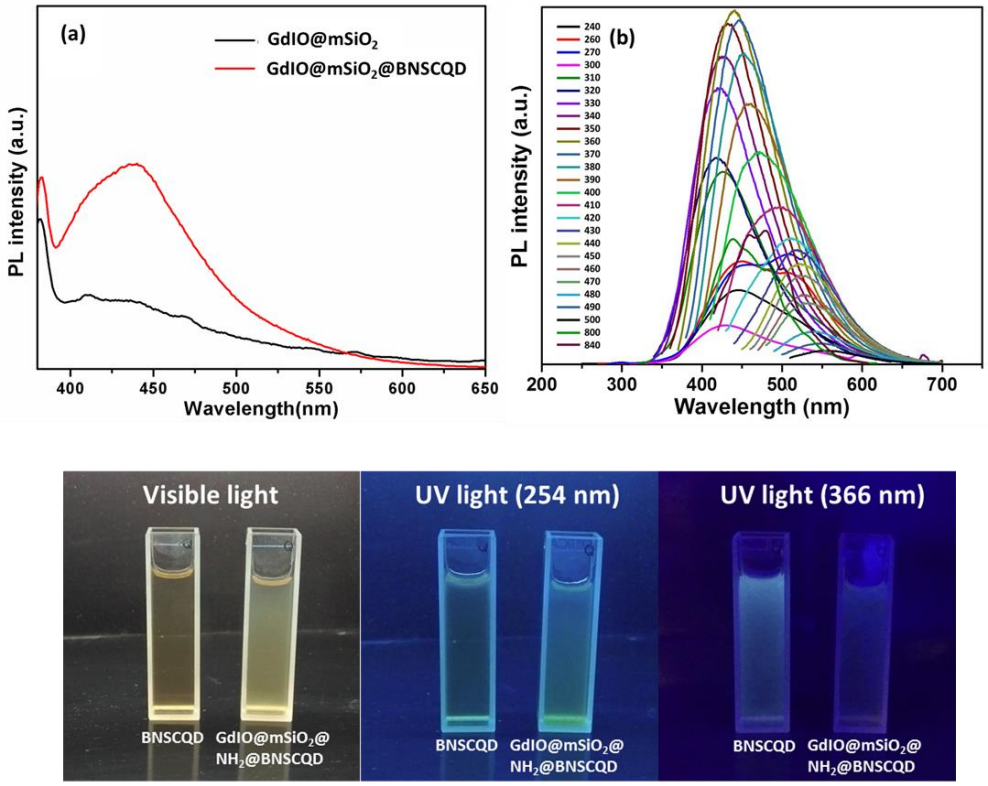

Fig. 7 (a) Comparison of PL GdIO@mSiO$_2$ and GdIO@mSiO$_2$@BNSCQD, (b) Excitation dependent emission of GdIO@mSiO$_2$@BNSCQD, (c) Digital images of BNSCQD and GdIO@mSiO$_2$@BNSCQD.

Magnetic property

The magnetization curves at room temperature (Fig. 8) for both samples GdIO and GdIO@mSiO$_2$@BNSCQD do not show any hysteresis and hence are superparamagnetic at room temperature. The field-dependent magnetization (M-H) curve of GdIO shows that the saturated magnetization (Ms) value of GdIO nanocubes was 36 emu g^{-1}, smaller than that of pure Fe_3O_4 nanocubes of similar size (52 emu g^{-1}). The reduced saturation magnetization of the GdIO nanocubes is possibly because of the decrease of the iron oxide content in the nanocubes. Furthermore, the incorporation of Gd could perturb the long range spin ordering

of the iron oxide core. Ms values of the GdIO@mSiO$_2$@BNSCQD hybrid sphere was found to be 10 emu/g. Reasonable saturation magnetization along with superparamagnetism is highly desirable for applications in magnetically guidable drug delivery and as a contrast enhancing agent in MRI. Hence, GdIO@mSiO$_2$@BNSCQD would be a suitable material for above applications. The potential imaging functionality of GdIO@mSiO$_2$@BNSCQD as T1 and T2 dual mode contrast agent during chemotherapy, their phantom MR imaging has been performed on a 1.5 T MRI scanner, and both longitudinal and transverse relaxivities r1 and r2 have been calculated. With an increase in the particle concentration in phantom solution, SI T1-weighted MR signal increased, whereas the T2-weighted MR signal decreased (Fig. 9a,b). Both T1 and T2 relaxation times are inversely proportional to the particle concentration as expected (Fig. 9c,d). The percentage of both T1 and T2 contrast enhancement of the composite sample GdIO@mSiO$_2$@BNSCQD with respect to metal ions has been calculated (Table 1) and compared with the contrast enhancement of control samples Fe_3O_4 and Gd_2O_3 (Table 2) using ImageJ software. The longitudinal relaxivity (r1) and transverse relaxivity (r2) were determined from the slope of the linear regression fit from the relaxation rate versus concentration curves. The r1 and r2 values of our GdIO@mSiO$_2$@BNSCQD particles were measured to be 10 mM^{-1} s^{-1} which is higher than r1 relaxivity of commercially available Gd-DTPA contrast agent (6.0 ± 0.6 mM^{-1} s^{-1}), whereas r2 relaxivity is 165 mM^{-1} s^{-1} which is more than that of commercially available dextrancoated ferrite nanoparticles such as ferridex (120 mM^{-1} s^{-1}) and combidex (65 mM^{-1} s^{-1}). The remarkable enhancement in r1 and r2 values of GdIO core compared with individual entities might be due to the coordination of water on the GdIO surface because of silica coating. According to Caravan et al.,[45] subtle combination of rotation correlation times and water exchange rate is required for high r1 and r2 values at low fields (below 1.5 T). This tendency points to an impact of silica coating thickness in relaxivity of silica-coated Gd(III) complexes. The importance of silica coating thickness in relaxivity is well documented for aqueous colloids of silica-coated iron oxide nanoparticles and Gd(III) complexes.[46,47] In our case, the higher r1 and r2 values of GdIO@mSiO$_2$@BNSCQD might be due to diffusion of water molecules through silica, which enhances water coordination on GdIO and hence relaxation times. The percentage of both T1 and T2 contrast enhancement of the composite sample GdIO@mSiO$_2$@BNSCQD with respect to metal ions has been calculated (Table 1) and compared with the contrast enhancement of control samples Fe_3O_4 and Gd_2O_3. Hence, the GdIO@mSiO$_2$@BNSCQD hybrid theranostic particle can act as a T1 as well as T2 contrast agent.

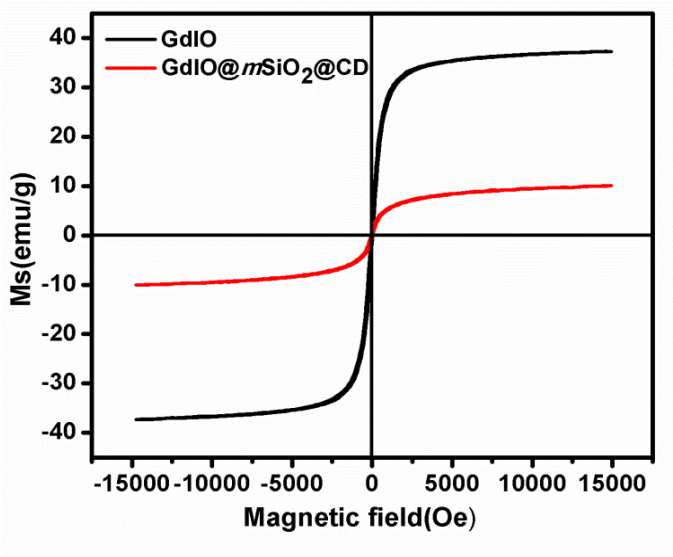

Fig. 8 Room temperature magnetization of the (a) GdIO and (b) GdIO@mSiO$_2$

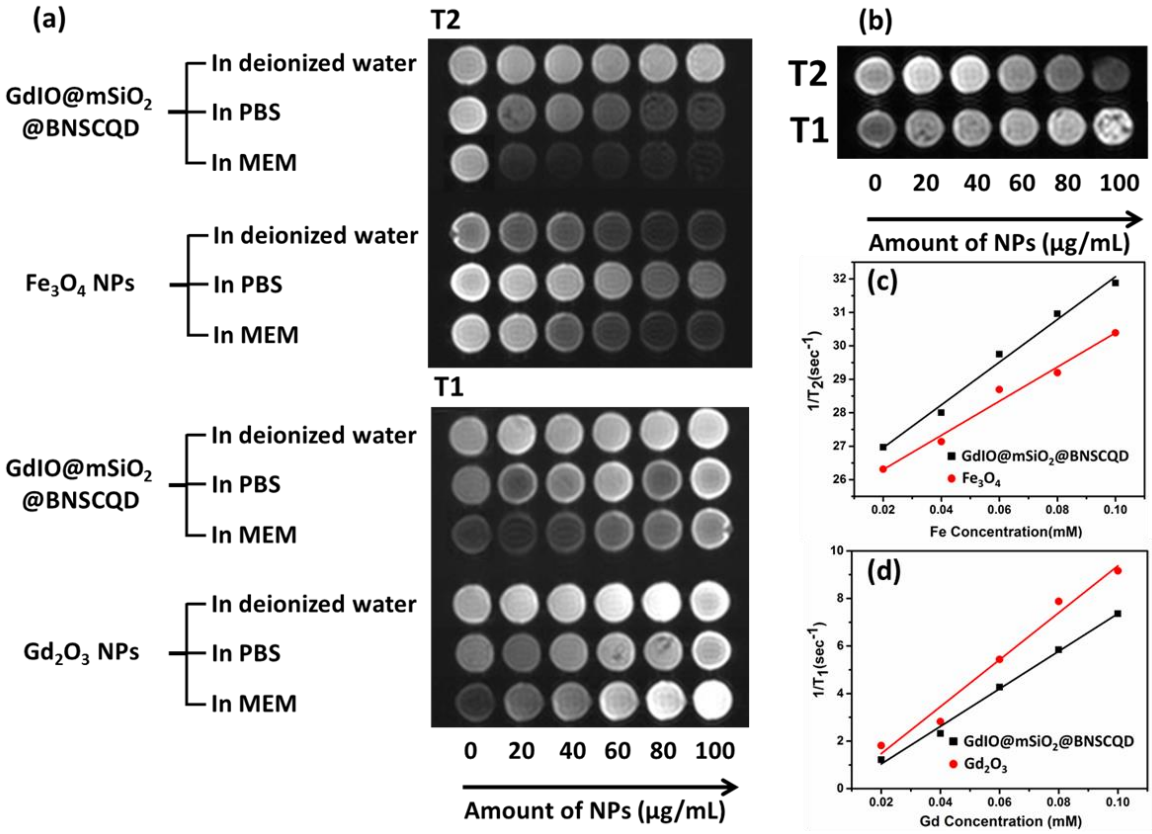

Fig. 9 (a) T1 and T2 weighted MR phantom images of GdIO@mSiO$_2$@BNSCQD, Fe_3O_4 and Gd_2O_3 particles, (b) invitro MR phantom images of GdIO@mSiO$_2$@BNSCQD in HepG2 cells, (c) concentration dependent longitudinal relaxation (1/T2) curves, (c) concentration dependent transverse relaxation curves 1/T1.

Table 1. Percentage of contrast enhancement with respect to GdIO@mSiO$_2$@BNSCQD particle concentration analysed using Image J.

	GdIO@mSiO$_2$@BNSCQD							
	T2 MR Contrast Enhancement (%)				T1 MR Contrast Enhancement (%)			
Sample concentration (μg/mL)	Deionized water	PBS	MEM	*invitro*	Deionized water	PBS	MEM	*invitro*
20	5.6	7.26	5.3	2.63	6.3	4.67	2.92	11.64
40	6.36	9.32	26.43	13.42	7.54	8.86	4.61	20.03
60	15.09	12.84	43.07	38.07	11.76	15.43	7.66	28.41
80	18.64	27.61	60.72	49.33	16.54	14.92	8.12	32.9
100	22.14	38.79	80.31	65.91	18.71	17.16	11.05	56.11

Table 2. Percentage of contrast enhancement in control samples Fe_3O_4 and Gd_2O_3.

	Fe_3O_4	Negative Control		Gd_2O_3		
	T2 MR Contrast Enhancement (%)			T1 MR Contrast Enhancement (%)		
Sample concentration (μg/mL)	Deionized water	PBS	MEM	Deionized water	PBS	MEM
20	10.04	17.36	21.37	7.5	4.29	5.88
40	12.13	18.41	32.02	12.98	6.42	18.32
60	24.6	28.94	49.83	18.23	9.37	29.04
80	25.29	39.33	57.34	21.62	12.04	37.17
100	24.13	60.17	62.12	18.7	15.4	68.33

5-Fluorouracil loading and release

Because of the high surface area and porous network structure, amine-functionalized GdIO@mSiO$_2$ can work as an excellent adsorbent for anticancer drug 5-Fu. The 5-Fu loading capacity of GdIO@mSiO$_2$ was determined by soaking the particles in 5-Fu solution (1 mg/mL) prior to capping with BNSCQD. The drug encapsulation efficiency was found to be 85% (Fig. 10a). The uncapping of the supramolecular gate on GdIO@mSiO$_2$ is triggered by two internal stimuli, that is, (1) low pH in lysosome environment which disrupts the electrostatic interaction between mesoporous wall and BNSCQD and (2) affinity of surface

boronic acid groups toward glycan receptor SL^a results in uncapping of mesochannels and release of the drug.[48-50] To verify the above fact, we conducted the release experiment by incubating GdIO@mSiO$_2$@5-Fu particles at different pH (Fig. 10b). The quantity of the released drug was monitored by UV−vis (λ_{max} = 266 nm). At pH 7.4, there is negligible release (<10%) of drug up to 50 h, indicating a tight stuffing of 5-Fu in inside GdIO@MSN spheres capped with BNSCQD which results in zero premature release. However, when the drug-loaded particle was incubated at lower pH 4.2, there was a burst release of 5-Fu up to 30% in 12 h and then slowly increases up to 82% at the end of 60 h (Fig. 10b). The release behavior does not show explosive release but sustained release because of fine control of drug transport by the BNSCQD gatekeeper. Such types of sustained release systems are highly desirable because more drugs can be protected before the drug reaches endosome and thus be released in the cytoplasm. The percentage of drug release reaches maximum because of the combined effect of gate opening by BNSCQD and loss of electrostatic interaction between 5-Fu and surface silanol groups.

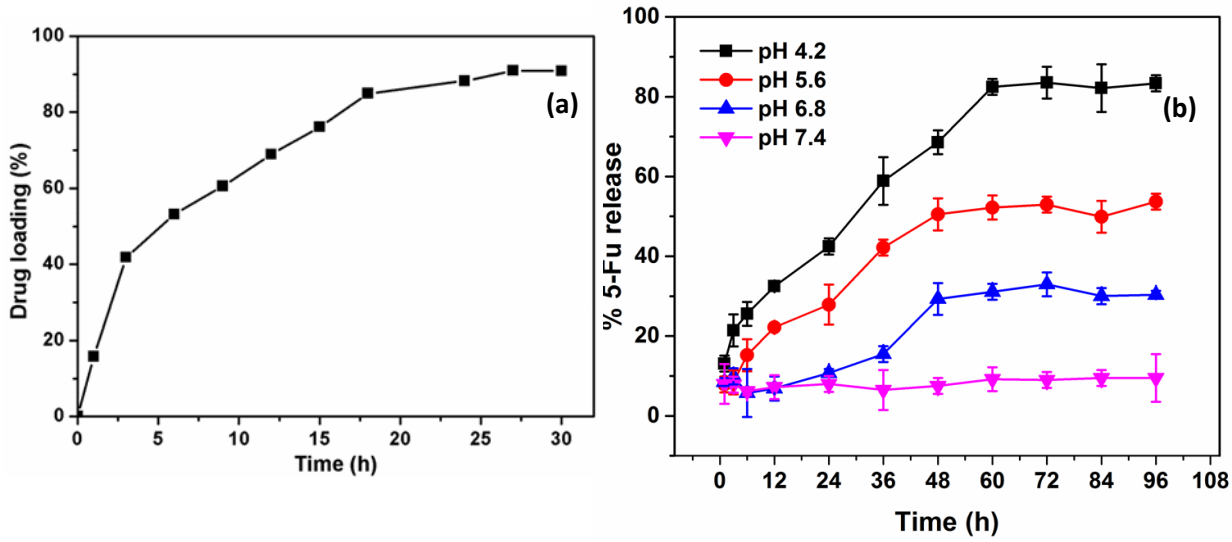

Fig. 10 (a) Increase in drug loading on GdIO@mSiO$_2$ with respect to time and (b) Release of 5-Fu from GdIO@mSiO$_2$@BNSCQD at different pH.

Receptor sensing based drug release study

To investigate the receptor-responsive gate opening property of 5-Fu@GdIO@mSiO$_2$@BNSCQD, we performed one competitive binding experiment. The drug release was conducted in presence and absence of free SL^a which has a stronger binding affinity for surface boronic acid groups of BNSCQD at low pH. The concentration of SL^a was varied between 0 and 1 μM. Keeping the pH constant at 4.5 the release of 5-Fu with SL^a has been presented in Fig. 11a. It was observed that with the increase in the availability of

SL^a, the release of 5-Fu increases. There was an immediate release of 5-Fu when excess SL^a is present, which was not observed when the drug release experiment was conducted in absence of SL^a. At the same time, control experiments were also performed in the 5-Fu loaded uncapped material in the presence and absence of SL^a (Fig. 11b). It was perceived that when there is no BNSCQD gate at the opening of the mesochannel, the release of 5-Fu difference in the drug release behavior in the presence and absence of SL^a is negligible. Because the detachment of BNSCQD from GdIO@mSiO2 is assimilated with the uncapping event, in the absence of SL^a little 5-Fu was released signifying efficient confinement of the drug in the pores of MSN by BNSCQD. All these observations demonstrated the significant role of BNSCQD supramolecular switch in the GdIO@$mSiO_2$ hybrid nanosystem. The therapeutic cargoes can be encapsulated at physiological pH and circulated in normal blood stream which is favorable for drug storage and control release without significant leakage. From the UV calibration curve, we quantified that at pH 4.5 1 µg of 5-Fu-loaded GdIO@$mSiO_2$@BNSCQD can release 0.0071 µg 5-Fu.

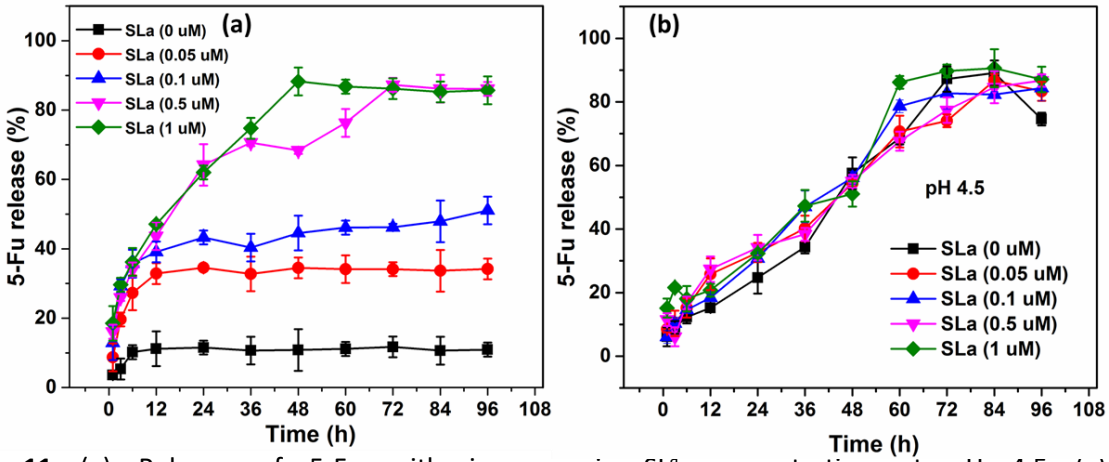

Fig. 11 (a) Release of 5-Fu with increase in SL^a concentration at pH 4.5 (a) 5-Fu@GdIO@$mSiO_2$@BNSCQD, (b)5-Fu@GdIO@$mSiO_2$.

In vitro cytotoxicity

To verify the cytotoxic effect of our drug carrier GdIO@$mSiO_2$@BNSCQD, we conducted cell viability in 3T3, PC3, and HePG2 cells through MTT (3-(4,5-dimethyl thiazol-2-yl)-2,5-diphenyltetrazolium-bromide) assay. This method is based on the formation of dark red formazan crystals by the metabolically active cells after exposure to MTT. The individual components of the drug carrier impose negligible toxic effects (Fig. 12). More than 85% cell viabilities were observed when incubated with the GdIO@$mSiO_2$@BNSCQD for all cells used even at a concentration of upto 80 µg/mL (Fig. 13a). Subsequently, the proliferation of HePG2 cells reduced significantly with the drug-loaded particles 5-

Fu@GdIO@mSiO$_2$@BNSCQD under the release condition in comparison to those of 3T3 and PC3 cells (Fig. 13b). The IC50 value of the drug-loaded particle was found to be 45 μg/mL which is equivalent to 0.9 μg/mL of free 5-Fu. The IC50 value of free 5-Fu is 5 μg/mL in HePG2 cells as reported in the literature. Such a significant reduction in the proliferation of HePG2 cells in comparison to other cells is attributable to the active intracellular uptake of drug-loaded particles in a SL^a receptor-mediated endocytosis. In contrast, PC3 has negligible expression of surface glycan SLa as reported in the literature51 and also verified by flow cytometry. The boronic acid groups present on BNSCQD gatekeeper recognises SLa receptors and results in target-specific delivery of the drug. The interaction of BNSCQD and SL^a has been thoroughly investigated in Chapter 2. In case of SL^a, the combined interaction of boronic acid-cis diol and thiophene-secondary amine results in aggregation among BNSCQD and enhancement in fluorescence signal.

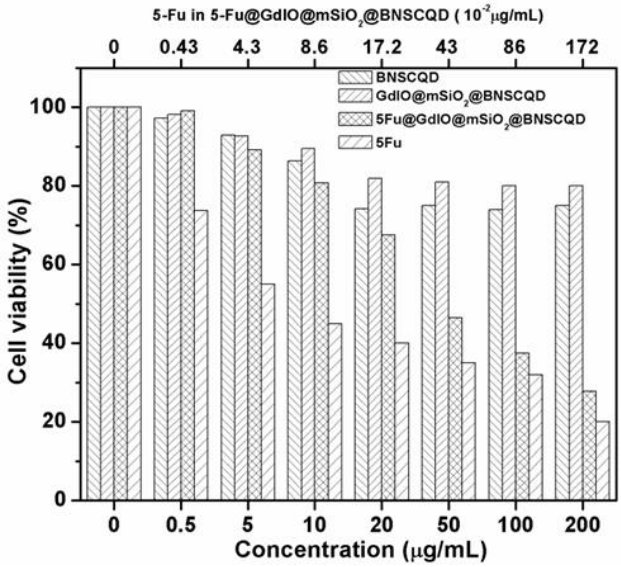

Fig. 12 MTT assay of BNSCQD, GdIO@mSiO$_2$@BNSCQD, 5Fu@GdIO@mSiO2@BNSCQD, and free 5-Fu.

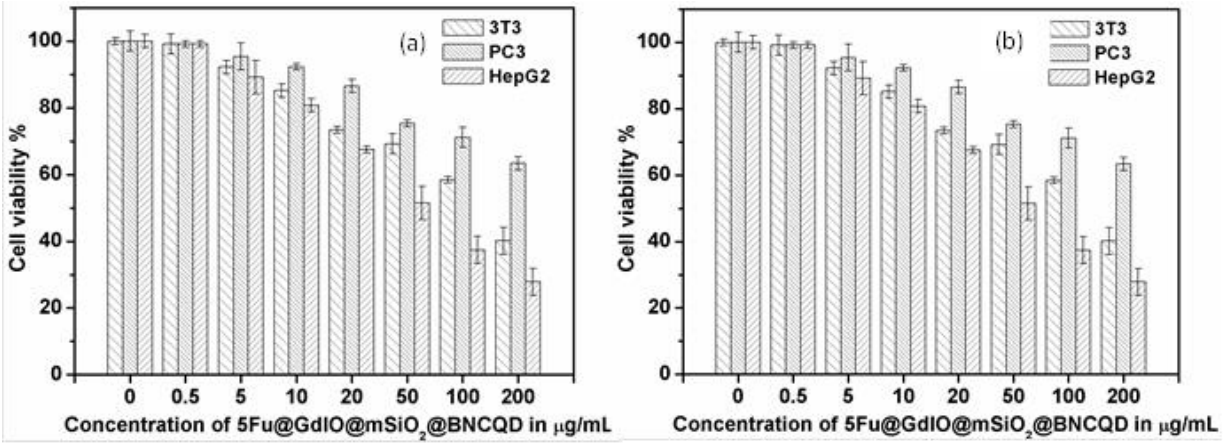

Fig. 13 (a) Cell viability of GdIO@mSiO$_2$@BNSCQD particle in different cell lines, (b) Effect of 5-Fu@GdIO@mSiO$_2$@BNSCQD on viability of different cells under drug release condition.

Intracellular uptake and apoptosis

Cancer cell targeting as well as optical imaging properties of uniquely designed 5-Fu@GdIO@mSiO$_2$@BNSCQD-gated nanoparticles have been verified in PC3 and HePG2 cells using fluorescence microscopy. With the increase in the incubation time the green signal from the cytoplasm progressively increased in the case of the HePG2 cells, which indicates that the particles are selectively targeted to HePG2 cells through Sla receptor-mediated endocytosis and are localized in the cytoplasm (Fig. 14). The cytotoxic effect of 5-Fu@GdIO@mSiO$_2$@BNSCQD was investigated by observing the nuclear fragmentation in HepG2 cells, which is a trademark of nuclear apoptosis. In a dose-dependent manner, an increase in the formation of fragmented nuclei containing condensed nuclear material was observed in fluorescence microscopy after staining with DAPI (Fig. 15).

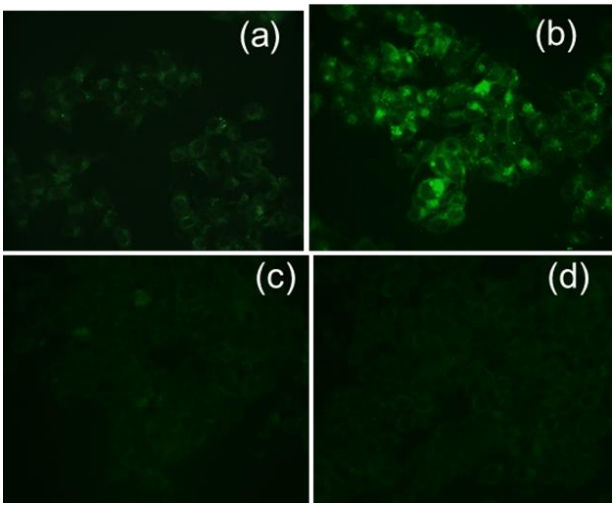

Fig. 14 Fluorescence image of HePG2 cells incubated with GdIO@mSiO$_2$@BNSCQD under drug release condition (a) image at 0 min, (b) image at 30 min, (c) image of 3T3 cell at 0 min, (d) 30 min

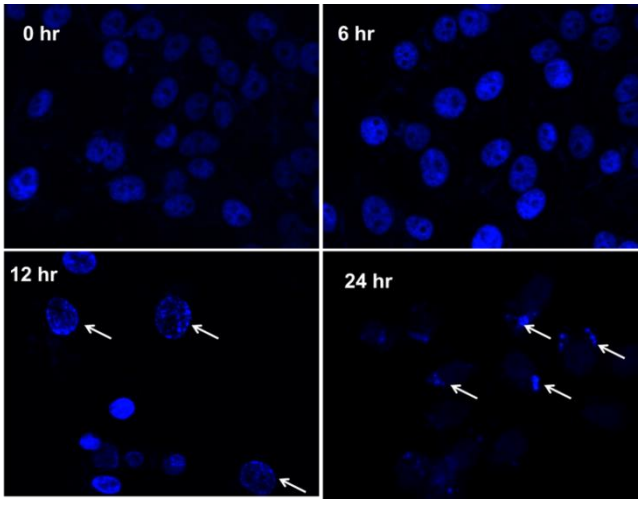

Fig. 15 DAPI fluorescence images of HePG2 cells incubated with 5-Fu@GdIO@mSiO$_2$@BNSCQD particles. With progress of time the hallmark apoptotic features such as nuclear condensation, fragmentation, and formation of apoptotic bodies becomes clear.

Proposed mechanism

Fig. 16 schematically presents the working mechanism of the theranostic particle. When the gated particle reaches the tumor environment, BNSCQD gets detached from the particle because of the loss of electrostatic interaction to some extent and gets attached to the surface SL^a receptor because of the binding affinity of boronic acid groups toward SL^a. In addition, the fluorescence signal of BNSCQD is further enhanced when it binds to SLa. Hence, the particle acts as an excellent targeted fluorescence imaging agent.

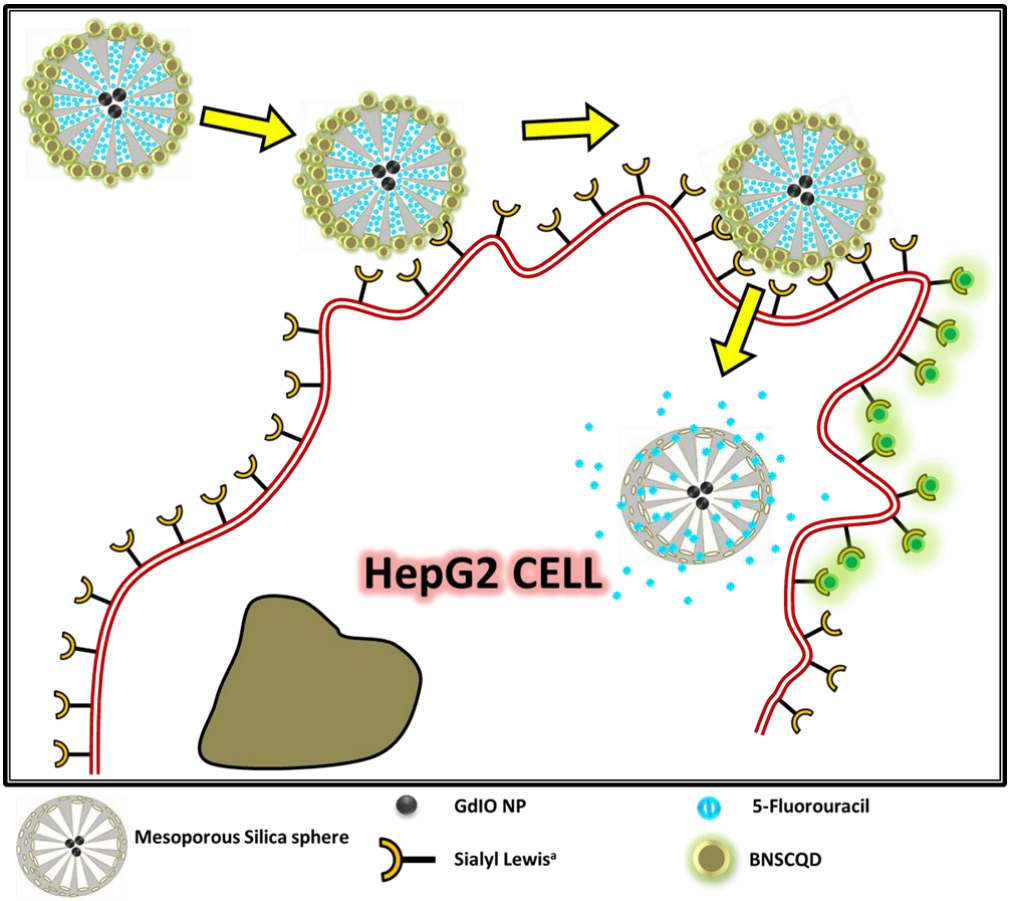

Fig. 16 Schematic presentation of target specific internalization and fluorescence switch on mechanism of 5-Fu@GdIO@mSiO_2@BNSCQD theranostic particle through BNSCQD-SL^a interaction.

Conclusion

In this chapter,

- We have developed a smart theranostic nanoparticle by integrating excellent characteristics of gadolinium iron oxide, MS, and hetero atom-doped carbon quantum dot (BNSCQD) and following a host−guest approach.

- BNSCQD imparts multiple functions such as simultaneous pH-sensitive gate opening, leading to control drug release, optical imaging, and receptor targeted internalization of the theranostic particle.
- The drug release experiment under variable pH and in the presence of competitive binding ligand SLa clearly shows the excellent responsiveness of the BNSCQD capped MSN hybrid system toward dual stimuli.
- Due to the reasonably good r1 r2 relaxivities of the magnetic core and excellent fluorescence property of the doped carbon quantum dot, the hybrid can be utilized to monitor the therapeutic response through MRI and/or fluorescence imaging.

References

1. National Institutes of Health [NIH]. National Institute of Health Roadmap for Medical Research: *Nanomedicine*. 2006. http://nihroadmap.nih.gov/nanomedicine (**accessed May 15, 200**6).
2. European Science Foundation [ESF]. *Nanomedicine*. An ESFEuropean Medical Research Councils (EMRC) Forward Look Report; France ESF: Strasbourg Cedex, 2004.
3. J. Shi, P. W. Kantoff, R. Wooster and O. C. Farokhzad, *Nat. Rev. Cancer* , 2017, **17**, 20-37.
4. E.-K. Lim, T. Kim, S. Paik, S. Haam, Y.-M. Huh and K. Lee, *Chem. Rev.*, 2015, **115**, 327-394.
5. Z. Cheng, A. A. Zaki, J. Z. Hui, V. R. Muzykantov and A. Tsourkas, *Science*, 2012, **338**, 903-910.
6. J. E. Lee, N. Lee, T. Kim, J. Kim and T. Hyeon, *Acc. Chem. Res*., 2011, **44**, 893-902.
7. F. Tang, L. Li and D. Chen, *Adv. Mater.*, 2012, **24**, 1504-1534.
8. D. Tarn, C. E. Ashley, M. Xue, E. C. Carnes, J. I. Zink and C. J. Brinker, *Acc. Chem. Res*., 2013, **46**, 792-801.
9. S. Alberti, G. J. A. A. Soler-Illia and O. Azzaroni, *Chem. Commun*., 2015, **51**, 6050-6075.
10. H. Meng, M. Xue, T. Xia, Y.-L. Zhao, F. Tamanoi, J. F. Stoddart, J. I. Zink and A. E. Nel, *J. Am. Chem. Soc*., 2010, **132**, 12690-12697.
11. M. W. Ambrogio, T. A. Pecorelli, K. Patel, N. M. Khashab, A. Trabolsi, H. A. Khatib, Y. Y. Botros, J. I. Zink and J. F. Stoddarrt, *Org. Lett*., 2010, **12**, 3304-3307.

12. Z. Li, J. C. Barnes, A. Bosoy, J. F. Stoddart and J. I. Zink, *Chem. Soc. Rev*., 2012, **41**, 2590-2605.
13. H. Zhou, X. Wang, J. Tang and Y.-W. Yang, *Polym. Chem*., 2016, **7**, 2171-2179.
14. Q. Gan, X. Lu, W. Dong, Y. Yuan, J. Qian, Y. Li, J. Shi and C. Liu, *J. Mater. Chem*., 2012, **22**, 15960-15968.
15. F. Muhammad, M. Guo, W. Qi, F. Sun, A. Wang, Y. Guo and G. Zhu, *J. Am. Chem. Soc.*, 2011, **133**, 8778-8781.
16. W. Gui, W. Wang, X. Jiao, L. Chen, Y. Wen and X. Zhang, *ChemPhysChem*, 2015, **16**, 607-613.
17. L. A. Torre, F. Bray, R. L. Siegel, J. Ferlay, J. Lortet-Tieulent and A. Jemal, *Ca-Cancer J. Clin.*, 2015, **65**, 87-108.
18. P. L. Bedard, A. R. Hansen, M. J. Ratain and L. L. Siu, *Nature*, 2013, **501**, 355-364.
19. S. Mura and P. Couvreur, *Adv. Drug Deliv. Rev*., 2012, **64**, 1394-1416.
20. T. M. Allen, *Nat. Rev. Cancer*, 2002, **2**, 750-763.
21. R. Sinha, G. J. Kim, S. Nie and D. M. Shin, *Mol. Cancer Ther.*, 2006, **5**, 1909-1917.
22. Y.-P. Sun, B. Zhou, Y. Lin, W. Wang, K. A. S. Fernando, P. Pathak, M. J. Meziani, B. A. Harruff, X. Wang, H. Wang, P. G. Luo, H. Yang, M. E. Kose, B. Chen, L. M. Veca and S.-Y. Xie, *J. Am. Chem. Soc.*, 2006, **128**, 7756-7757.
23. Y. Wang and A. Hu, *J. Mater. Chem. C*, 2014, **2**, 6921-6939.
24. X. T. Zheng, A. Ananthanarayanan, K. Q. Luo and P. Chen, *Small*, 2015, **11**, 1620-1636.
25. R. Wang, K.-Q. Lu, Z.-R. Tang and Y.-J. Xu, *J. Mater. Chem. A*, 2017, **5**, 3717-3734.
26. S. Y. Lim, W. Shen and Z. Gao, *Chem. Soc. Rev*., 2015, **44**, 362-381.
27. G. Hong, S. Diao, A. L. Antaris and H. Dai, *Chem. Rev.*, 2015, **115**, 10816-10906.
28. J.-H. Liu, L. Cao, G. E. LeCroy, P. Wang, M. J. Meziani, Y. Dong, Y. Liu, P. G. Luo and Y.-P. Sun, *ACS Appl. Mater. Interfaces*, 2015, **7**, 19439-19445.
29. P. G. Luo, S. Sahu, S.-T. Yang, S. K. Sonkar, J. Wang, H. Wang, G. E. LeCroy, L. Cao and Y.-P. Sun, *J. Mater. Chem. B*, 2013, **1**, 2116-2127.
30. S. Sahu, B. Behera, T. K. Maiti and S. Mohapatra, *Chem. Commun.*, 2012, **48**, 8835-8837.
31. C. Ding, A. Zhu and Y. Tian, *Acc. Chem. Res*., 2014, **47**, 20-30.
32. Y. Song, W. Shi, W. Chen, X. Li and H. Ma, *J. Mater. Chem*., 2012, **22**, 12568-12573.

33. A.-A. Nahain, J.-E. Lee, I. In, H. Lee, K. D. Lee, J. H. Jeong and S. Y. Park, *Mol. Pharm.*, 2013, **10**, 3736-3744.
34. L. Chai, J. Zhou, H. Feng, C. Tang, Y. Huang and Z. Qian, *ACS Appl. Mater. Interfaces*, 2015, **7**, 23564-23574.
35. M. Zheng, S. Ruan, S. Liu, T. Sun, D. Qu, H. Zhao, Z. Xie, H. Gao, X. Jing and Z. Sun, *ACS Nano*, 2015, **9**, 11455-11461.
36. R. K. Das and S. Mohapatra, *J. Mater. Chem. B*, 2017, **5**, 2190-2197.
37. C. Han, H. Xu, R. Wang, K. Wang, Y. Dai, Q. Liu, M. Guo, J. Li and K. Xu, *J. Mater. Chem. B*, 2016, **4**, 5798-5802.
38. Q.-X. Mao, E, S. J.-M. Xia, R.-S. Song, Y. Shu, X.-W. Chen and J.-H. Wang, *Langmuir*, 2016, **32**, 12221-12229.
39. X.-W. Hua, Y.-W. Bao, Z. Chen and F.-G. Wu, *Nanoscale*, 2017, **9**, 10948-10960.
40. S. Sahu, N. Sinha, S. K. Bhutia, M. Majhi and S. Mohapatra, *J. Mater. Chem. B*, 2014, **2**, 3799-3808.
41. G. Modugno, C. Me´nard-Moyon, M. Prato and A. Bianco, *Br. J. Pharmacol.*, 2015, **172**, 975-991.
42. Y. Choi, S. Kim, M.-H. Choi, S.-R. Ryoo, J. Park, D.-H. Min and B.-S. Kim, *Adv. Funct. Mater.*, 2014, **24**, 5781-5789.
43. T.-H. Shin, Y. Choi, S. Kim and J. Cheon, *Chem. Soc. Rev*., 2015, **44**, 4501-4516.
44. N. Lee, D. Yoo, D. Ling, M. H. Cho, T. Hyeon and J. Cheon, *Chem. Rev*., 2015, **115**, 10637-10689.
45. P. Caravan, *Chem. Soc. Rev*., 2006, **35**, 512-523.
46. S. L. C. Pinho, G. A. Pereira, P. Voisin, J. Kassem, V. Bouchaud, L. Etienne, J. A. Peters, L. Carlos, S. Mornet, C. F. G. C. Geraldes, J. Rocha and M.-H. Delville, *ACS Nano*, 2010, **4**, 5339-5349.
47. S. V. Fedorenko, S. L. Grechkina, A. R. Mustafina, K. V. Kholin, A. S. Stepanov, I. K. Nizameev, M. K. Kadirov, R. R. Zairov, A. N. Fattakhova, R. R. Amirov and S. E. Solovev, *Colloids Surfaces B Biointerfaces* , 2017, **249**, 243-249.
48. X. Zhang, Z. Zhang, X. Su, M. Cai, R. Zhuo and Z. Zhong, *Biomaterials*, 2013, **34**, 10296-10304.
49. A. Matsumoto, H. Cabral, N. Sato, K. Kataoka and Y. Miyahara, *Angew. Chem., Int. Ed.*, 2010, **49**, 5494-5497.

50. S. Deshayes, H. Cabral, T. Ishii, Y. Miura, S. Kobayashi, T. Yamashita, A. Matsumoto, Y. Miyahara, N. Nishiyama and K. Kataoka, *J. Am. Chem. Soc*., 2013, **135**, 15501-15507.
51. V. B. Chachadi, M. F. Ali and P.-W. Cheng, *PLoS One*, 2013, **8**, No. e57416.

Chapter – 5

Synthesis and Characterization of Heteroatom Doped Hollow Carbon Spheres for fluorescence Imaging and Photothermal Therapy of Cancer

5.1 Introduction

In 1867, German physician W. Busch reported a patient's tumor was "re-absorbed" after a high fever, induced by acute infections.[1] The use of circulatory water bath to treat uterine cervical cancer cells was also reported during that era. Owing to the elementary technology of that age neither the clinical application nor the studies of thermal therapy were further explored. Interest in thermal therapy was revived in 1980 and because of the fast development of optical materials and nanotechnology thermal therapy has become a fast growing field now-a-days. Through great efforts in developing technology for controlled and localized heating, as well as better understanding of the mechanisms behind temperature-induced cell killing, modern thermal treatment has proven to be effective alone or when combined with other cancer treatments such as radiation therapy and chemotherapy. [2,3] Typically, photothermal therapy (PTT) refers to treating cancer by targeted distribution of biocompatible nanoparticles and heat to the site of tumor without harming the healthy tissue. The heat generated is not enough to cause a macroscopic temperature increase but a localized temperature rise is achieved, termed as “hot spots”.[4] These hot spots are responsible for alteration in plasmatic membrane functioning, activation of thermally sensitive proteins and overexpression of some proteins in cellular environment. Currently, advanced nanoparticles generate heat utilizing non-toxic near-infrared range (NIR) for treating cancer cells. With respect to the limited penetration depth (0.01 - 3 cm) of NIR light as well as the varied locations of tumors in humans, the delivery of localized light may be either invasive or non-invasive in nature.

Nanomaterials with intense absorption in the near-infrared (NIR) region are promising for photothermal therapy (PTT). Numerous light responsive nanomaterials have been investigated for PTT, such as gold,[5] palladium,[6] copper,[7,8] iron,[9] gadolinium[10,11] and titanium[12] based noble metals and nanocomposites. Likewise, protein,[13] polymer,[14] and porphyrin [15,16] based nanoassemblies have also achieved thorough destruction of residual cancer cells and prevention of its recurrence. Although such nanoscale characteristics can enhance the detection or treatment of cancer, the single functionality in all the above examples of nanosystems limits their utility, because multiple systems are required to detect, monitor, and treat cancer. Notably, carbon-based nanostructures have received tremendous attention owing to their outstanding physical and chemical properties. Carbon nanotubes (CNTs) and graphene have been widely used in biomedical imaging and phototherapy applications. Initially, polyethylene glycol (PEG), antibody and silica associated carbon

nanotubes were synthesized and implied for photothermal ablation of metastatic tumour in mice.[17,18] Here the nanotubes (0.2 mg Kg^{-1}) reported a invivo tumour environment temperature raise of 55 °C. Further, two distinct reports on platinum and nitrogen doped carbon dot directed the synthesis of carbon based PTT material using potassium(II) tetrachloroplatinate, p-phenylenediamine, urea, citric acid and PEG as precursors.[19,20] The photothermal generated temperature for these doped carbon quantum dots (30-50 µg mL^{-1}) ranged between 55- 70 °C respectively. Recently, Gong et al. synthesized fluorinated carbon nanofibre for NIR guided chemophotothermal therapy and demonstrated their application in vitro in HeLa cells.[21] The reported nanofibre generated temperature of 70 °C with 0.2 mg mL^{-1} particle concentration. Similarly, Gao et al. have reported indocyanine green decorated carbon nanohorns for treating 4T1 tumor bearing nude mice.[22] These nanohorns (5 µg mL^{-1}) were reported to generate a change in heat of 40 °C. The efficacy of *in vivo* PTT basically depends on 1) accumulation of light-sensitive nanoparticles at targeted area through passive enhanced permeability and retention (EPR) effect or active targeting, 2) size and shape of the particles which is very important from biological point of view, 3) light to heat conversion efficiency and 4) the light power density with excitation time.

In pursuit of exploring carbon nanomaterials for theranostic applications, this chapter describes nitrogen doped mesoporous hollow carbon sphere using direct synthesis technique from pyrrole and aniline as precursors. It was found that, in the optimized synthesis conditions N doped carbon hollow spheres embedded with highly luminescent N-doped carbon dots (NCQD) have been formed. The structural and photoluminescence property of the materials at various synthesis conditions has been studied using transmission electron microscopy, Raman and fluorescence spectroscopy. The heat generating capacity of the material upon exposure to 980 nm laser has been investigated. In vitro intracellular fluorescence imaging and photothermal ablation effect of synthesized hollow spheres have been studied in detail in human oral cancer cells (FaDu) cells.

5.2 Experimental

Chemicals

Deionized water was purchased from Sigma Aldrich. Ammonium persulfate was supplied by Thermofisher Scientific Chemicals. Aniline was procured from Sisco Chem Ltd. Pyrrole was

supplied by Spectrochem Ltd. Triton X-100 and absolute ethanol was purchased from Changshu Yangyuan chemicals.

Synthesis of NCQD-HC and acid modified NCQD-HCS nanoparticles

Triton X-100 (0.1 g) was dissolved in 80 ml of deionized water. Then, a mixture of aniline (0.4 ml) and pyrrole (0.3 ml) was added to it under vigorous stirring. After 30 min of reaction, the mixture was maintained at 0°C followed by dropwise addition of precooled aqueous solution of ammonium persulphate (4 ml, 0.5 M). The reaction was stirred overnight for complete polymerization. Finally, the product was washed using deionized water and dried under vacuum at 60°C for 12 h. The dried sample was transferred to crucible and calcined at different temperatures (600°C, 700°C, 800°C and 900°C) for 10 h under N_2 atmosphere. After cooling the product was collected and stored in vacuum. The carboxylic acid group modification on surface of mesoporous carbon spheres was done by air calcination of the product at 300°C for 1 h. After thermal treatment, particles were dispersed in aqueous medium and used for the experiments.

Photothermal setup

The various amounts (10, 20, 30 μg mL^{-1}) of aqueous dispersed NCQD-HCS-800 were taken in a PL cuvette and irradiated with 980 nm NIR laser (1 Wcm^{-2}). The distance between the source and particles was maintained at 8.4 cm. After each time interval the temperature change was noted using a thermosensor rod.

Cytotoxicity assays

FaDu cells (1×10^4 cells) were seeded separately into 96-well plates and incubated in 200 μL Minimum esssential medium (MEM) and HaCaT cells (1×10^4 cells) were seeded separately into 96-well plates and incubated in 200 μL Dulbecco's modified Eagle's medium (DMEM) containing 10% FBS for 24 h (37 °C, 5% CO_2). After incubation, cells were treated with different concentrations of NCQD-HCS-800 (10, 25, 50, 100, 150 and 200 μg/mL) for 6 h. Following treatment was done by irradiating 980 nm laser (1W) maintaining a distance of 2.5 cm for 5 minutes per well. After 3 h of incubation, MTT solution was removed and replaced with 200 μL of DMSO. Absorbance was read at 570 nm using a microplate reader (BIO-RAD iMARK, 96 well type). The experiment was performed three times independently.

Cell cycle analysis by flow cytometry

Cell cycle analysis by flow cytometry with PI staining was performed using FaDu and HaCaT cells were incubated for 12 h in the presence of 50 µg mL^{-1} concentration of NCQD-HCS-800 nanoparticles at 37 °C in CO_2 incubator. Then each well was exposed to 980 nm laser (1W) maintaining a distance of 2.5 cm for 5 minutes. The cells were then harvested with trypsinisation and fixed with chilled 70% ethanol and stored at -20 °C. Then, the cells were washed with ice cold PBS (10 mM, pH 7.4) and incubated with 20 µl of DNAase-free RNase (10 mg mL^{-1}) and 20 µl of DNA intercalating dye PI (1 mg mL^{-1}) at 37 °C for 10 min in the dark. The distribution of cells in the different cell-cycle phases was analysed from the DNA histogram using a Becton-Dickinson FACS Calibur flow cytometer and analysed with Flow Jo software.

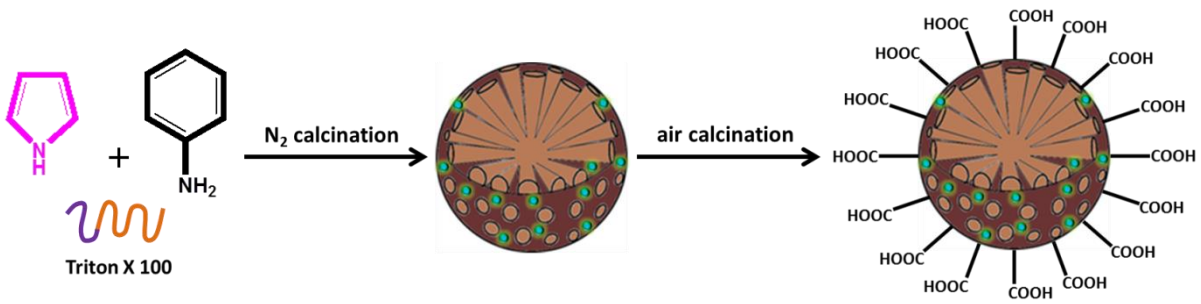

Fig. 1 Schematic representation of synthesis of NCQD-HCS

5.3 Results and discussion

The synthetic strategy for NCQD-HCS follows a direct template free method as illustrated in Figure 1. Briefly, the carbon precursors, hollow polyaniline-co-polypyrrole (PACP) nanospheres (Fig. 1), were prepared using the strategy of confined interfacial copolymerization of aniline and pyrrole in the presence of Triton X-100 micelle.[23,24] Then, the hollow PACP nanospheres were directly carbonized in a furnace under protection of an inert gas to readily obtain the target hollow N-doped carbon nanospheres. The key to realize highly porous structures is the utilization of the robust conjugated polymeric precursor that permits sufficient framework carbonizability and nanostructure inheritability, regardless of the rigorously applied carbonization conditions. The Triton X-100 supports both formation of self-assembly as well as porosity to the carbon spheres. After polymerization, the polymer was subjected to carbonization under nitrogen flow to obtain NCQD-HCS. The obtained

HCNs exhibit a well-defined nanospherical morphology. To regain the hydrophilicity of the assynthesized hollow spheres, a post modification of carboxylic acid groups was done by air calcination process.

Phase analysis by XRD and Raman spectroscopy

The comparative low angle XRD pattern (Figure 2A), shows the formation of porous matrix in the carbon spheres after subjected to inert calcination process. An intense peak at 2θ = 0.74°, suggests the body centred cubic mesophase development in NCQD-HCS-800 after treatment at 800°C.[25] Raman spectra of the as synthesized nanospheres exhibit the bonding, order and crystallinity of the materials (Figure 2). Figure 2 indicates change in disordered graphitic property of nanospheres with respect to variation in calcination temperature of precursor carbon polymer spheres, as revealed by two Raman nodes. The G-band (1593 cm^{-1}) corresponds to E_{2g} mode of hexagonal graphite resembling the vibrational energy level of sp^2 hybridized carbon atoms in graphitic layer. A blue shift of the G-band in case of NCQD-HCS-600 to NCQD-HCS-900 was found to be 32 cm^{-1}.[26] This shows that raise in synthesis temperature has affected the % nitrogen doping in the carbon matrix resulting in variation of chemical bond lengths. The I_D/I_G values for NCQD-HCS-600, NCQD-HCS-700, NCQD-HCS-800 and NCQD-HCS-900 were found to be 1.12, 1.06, 1 and 0.93 respectively. The decrease in I_D/I_G ratio suggests increase in graphitic nature of the matrix with respect to increase in synthesis temperature.

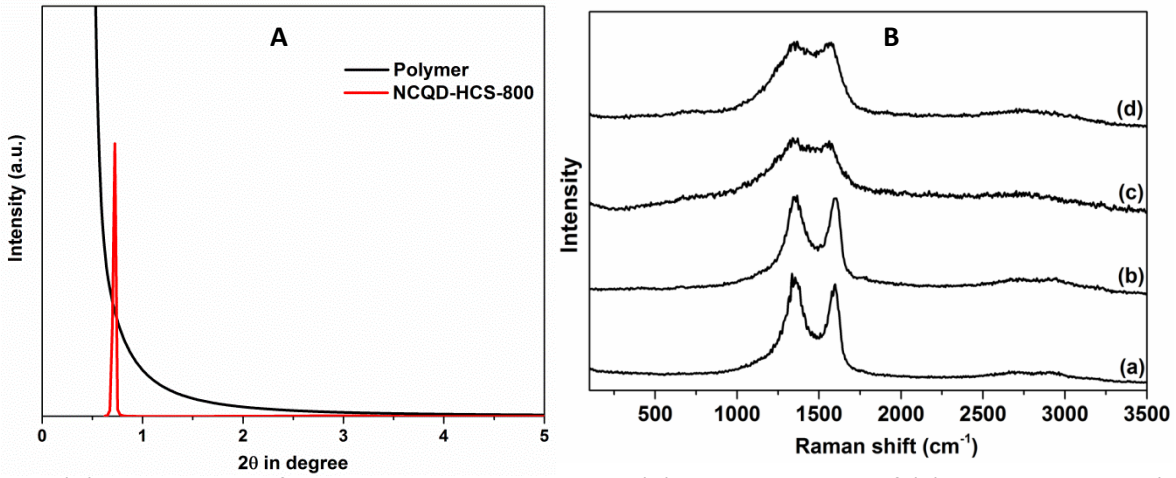

Fig. 2 (A) Comparison of low angle XRD pattern and (B) Raman spectra of (a) NCQD-HCS-600, (b) NCQD-HCS-700, (c) NCQD-HCS-800 and (d) NCQD-HCS-900.

TEM

Figure 3 shows the TEM micrograph of NCQD-HCS synthesized at different temperatures. The spherical nanoassemblies have shown a change in morphological features with respect to

temperature variation. Figure 3c and 3d indicate complete formation of hollow spheres with discrete boundaries. The nanospheres are almost monodisperse with an average particle size of 40-50 nm (Figure 3e). The discrete dark spots in figure 3g can be correlated with the development of NCQDs (~ 4-5 nm diameter) in hollow spheres during synthesis. The outer HCS shell has an average diameter 15 nm and the inner hollow space comprises of 35 nm in diameter (Figure 3g). The atomic weight % of each element in NCQD-HCS-800 is shown in figure 3h.

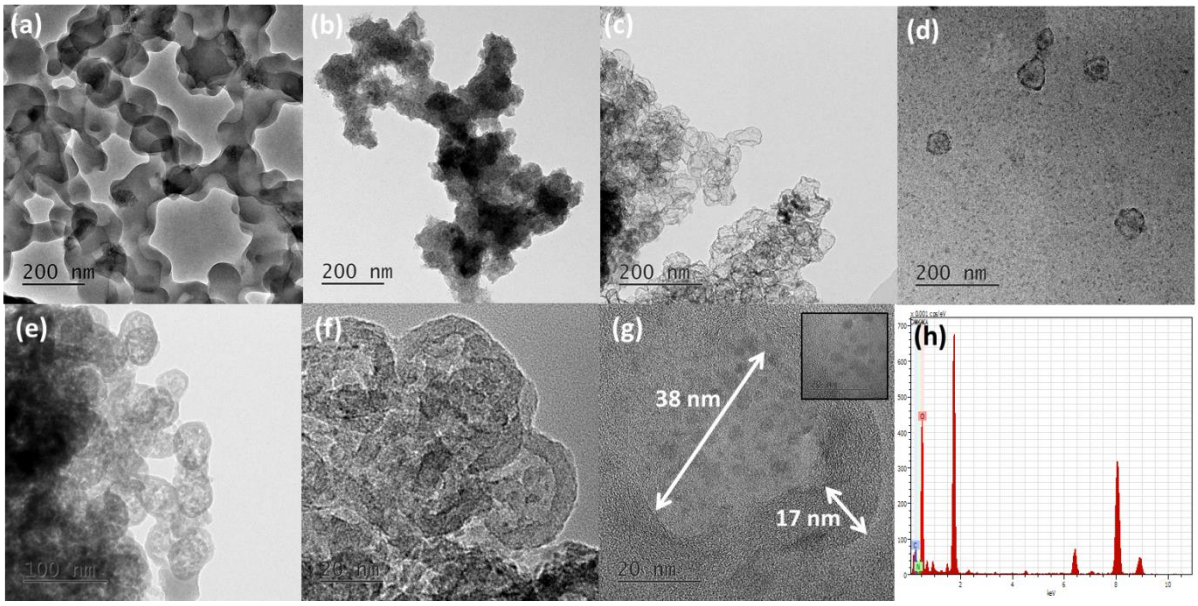

Fig. 3 TEM images of NCQD-HCS synthesized at (a) 600°C, (b) 700°C, (c) 800°C and (d) 900°C. (e) High resolution images of NCQD-HCS-800. (g) HRTEM of a single NCQD-HCS-800 hollow sphere (inset: NCQD deposition on carbon spheres) and (h) EDAX spectra of NCQD-HCS-800.

N_2 adsorption - desorption study

Nitrogen adsorption-desorption data elucidates the porous nature of our assynthesized nanoparticles. A comparative N_2 adsorption-desorption isotherms of different NCQD-HCS has been represented in Figure 4. The NCQD-HCS-600 reveals a type III isotherm whereas other curves indicate a type IV isotherm curves (Figure 4a). The BET surface area of NCQD-HCS-600, NCQD-HCS-700, NCQD-HCS-800 and NCQD-HCS-900 were found to be 97, 336, 540 and 628 m^2g^{-1} respectively (Table 1). This suggests that temperature increase enhanced the Ostwald ripening process and favoured the formation of higher surface area as reported for NCQD-HCS-900 spheres. Figure 4B exhibits the pore size distribution of the carbon nanospheres.[27] The BJH shows a narrow pore size distribution and found to be ~ 3nm. But, the pore volume in case of NCQD-HCS-800 and NCQD-HCS-900 is found to be much higher when compared to the other two nanospheres. However, the nanostructures with large

surface area and pore size are beneficial for transportation and encapsulation of guest molecules.

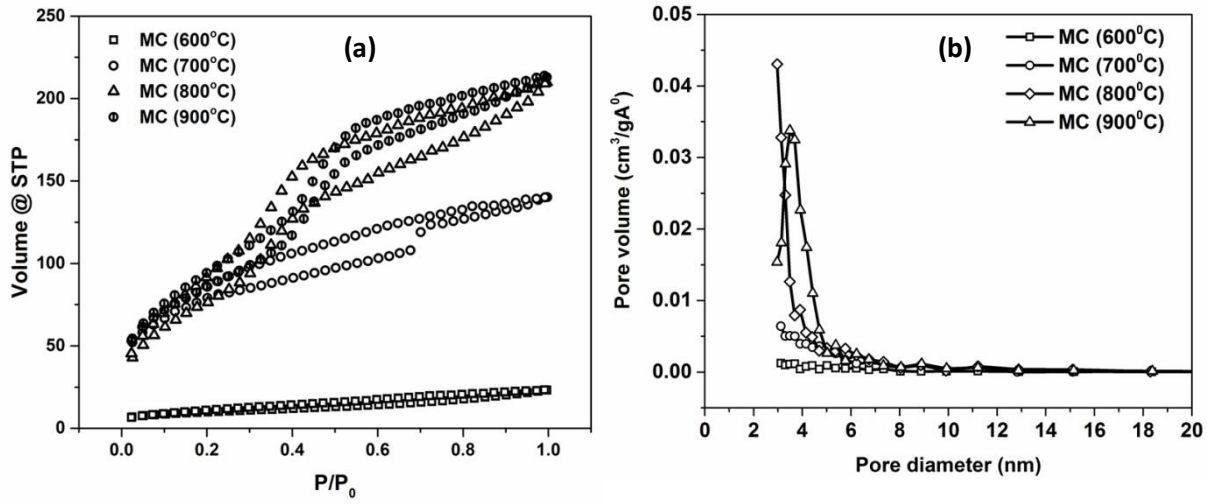

Fig. 4 Comparison plots of (a) Nitrogen adsorption-desorption isotherm, (b) pore size distribution of various assynthesized hollow carbon nanospheres.

Table 1 Comparison of BET data for various assynthesized hollow carbon nanospheres.

Sample	Surface area (m^2g^{-1})	Pore diameter (nm)
NCQD-HCS-600	97	3.12
NCQD-HCS-700	336	3.12
NCQD-HCS-800	540	2.96
NCQD-HCS-900	628	3.48

Luminescence property

Under day light, the aqueous solution of carboxylic acid functionalized NCQD-HCS-800 is yellowish-brown and bright green under UV excitation. The aromatic π network in the carbon matrix are responsible for absorption of wavelengths in UV region. At a fixed excitation of λ_{ex} = 340 nm, NCQD-HCS-800 shows an emission peak at 425 nm (Figure 5a). Figure 5b shows the excitation dependent emission of NCQD-HCS-800, which attributes to the presence of NCQDs embedded in the NCQD-HCS-800 matrix. Moreover, in our case, significant upconversion phenomena (λ_{ex} range= 650-1000 nm) was observed for the aqueous suspended NCQD-HCS-800 nanospheres (Figure 5c). Similarly, when excited with sole 980

nm laser source, there were four upconversion peaks observed within 200 to 750 nm. In figure 5d intense peaks at 315, 340 and 490 nm describes the spheres to be suitable for application in NIR bioimaging and phototherapy. The PL quantum yields (QY) collected for each sample is noted in Table 2. The NCQD-HCS-800 exhibits the highest QY of 14.6 %, which pronounces them best applicable for biological imaging studies under a wide range of excitation wavelengths.

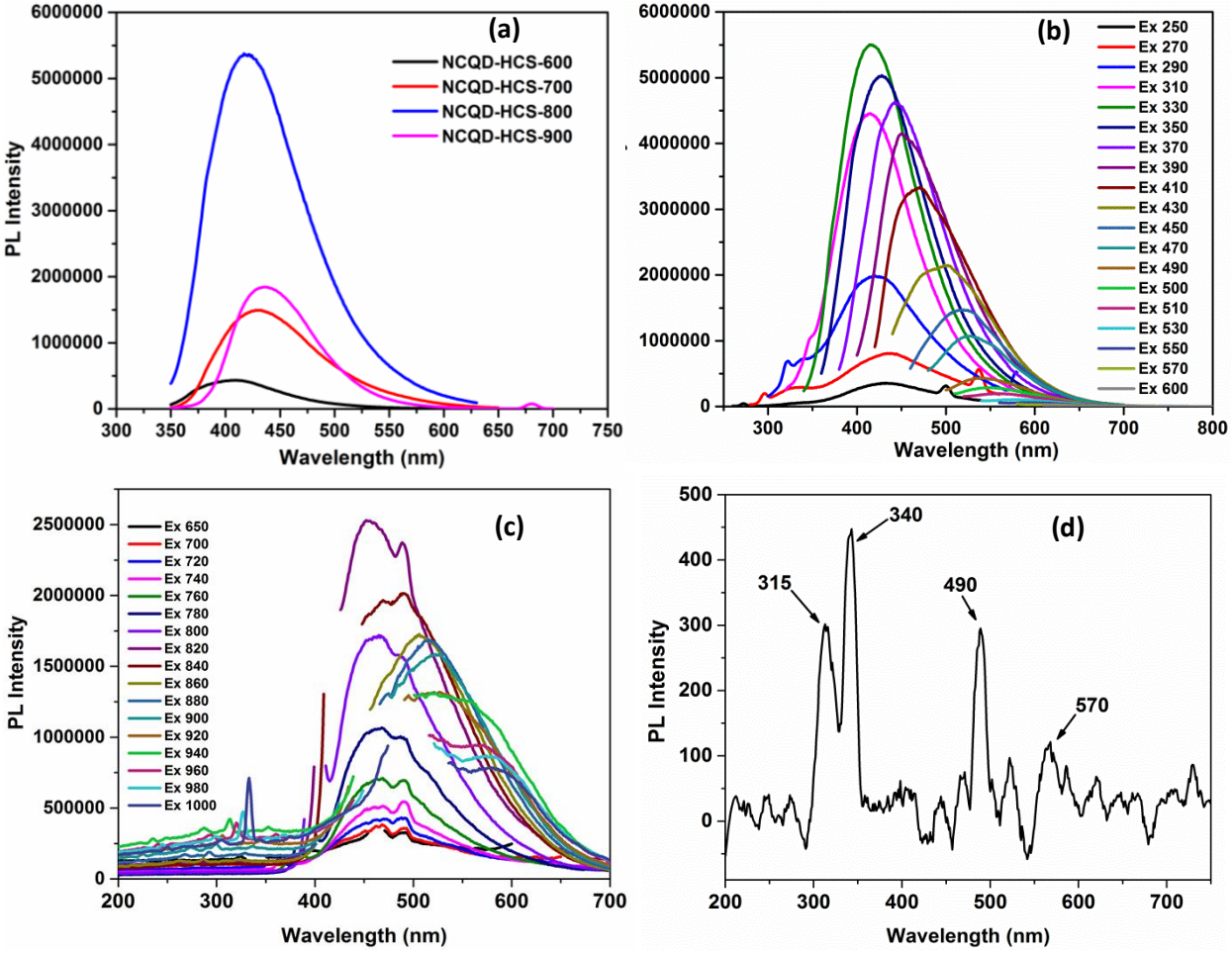

Fig. 5 (a) PL emission spectra (λ_{ex} = 340 nm) of BNSCQD with different boron contents (b)Down and (c) Up conversion profile of NCQD-HCS-800, (c) upconversion by NCQD-HCS-800 under 980 nm laser (1 Wcm^{-2}).

Table 2 Comparison table for quantum yield in different samples.

Sample	Quantum Yield
Polymer	0.11
NCQD-HCS-600	3.85
NCQD-HCS-700	6.4
NCQD-HCS-800	14.6
NCQD-HCS-900	9.4

Photothermal property

In order to explore NCQD-HCS for theranostic applications we investigated the optical absorption and photothermal conversion of NCQD-HCS-800. Standard drug carrier materials such as graphene oxide nanoparticles, mesoporous silica, iron oxide nanoparticles (SPION) and Au nanoparticles UV–Vis–NIR absorption spectra show that the NCQD-HCS possess a broad absorption band from the UV to NIR wavelength range (300-1400 nm) (Figure 6b). Carbon spheres, porous carbon spheres, and nanosized carbon dots have been extensively investigated by many groups.[28-32] When subjected to 980 nm NIR irradiation, the aqueous solution of NCQD-HCS-800 showed significant raise in temperature. Thus, suggesting it to be suitable towards application in photothermal therapy. The enhancement of temperature from 38 °C to 70 °C in Figure 6a shows that thermal effect of the assynthesized nanoparticles is directly proportional to the concentration of particles in the solution. Furthermore, in comparison to other standard drug carrier materials such as graphene oxide nanoparticles, mesoporous silica, iron oxide nanoparticles (SPION) and Au nanoparticles porous material like silica, our N-doped mesoporous carbon exhibits significant photothermal property under NIR exposure (Figure 6b). The photothermal conversion efficiency for all the synthesized carbon spheres were calculated following the method recently reported by Wu et al. in case of diketopyrrolopyrrole-dithiophene based polymer dots,[33]

$$\eta = \frac{hA\,(T_{max} - T_{amb}) - Q_0}{I\,(1 - 10^{-A_\lambda})}$$

where,

η = Photothermal conversion efficiency

h = Heat transfer coefficient

A = Surface area of container

T_{max} = Maximum temperature attained by the system

T_{amb} = Ambient temperature of the system

Q_0 = Energy radiated from solvent and container

I = Incident laser power

A_λ = Absorbance at 980 nm laser

and compared with the photothermal conversion efficiency of NCQDs in Table 2. The results revealed that with increase in calcination temperature the photothermal conversion efficiency of carbon spheres increased from 10.32% to 76.3%. However, in comparison to NCQDs the thermal conversion efficiency was quite high with respect to the carbon spheres. Thus, suggesting the large absorption coefficients of the NCQDs as well as the graphitic network of hollow carbon spheres are responsible for the photothermal effect. Therefore, these synthesized mesoporous nanospheres can be effectively used in the PTT based cancer treatment.

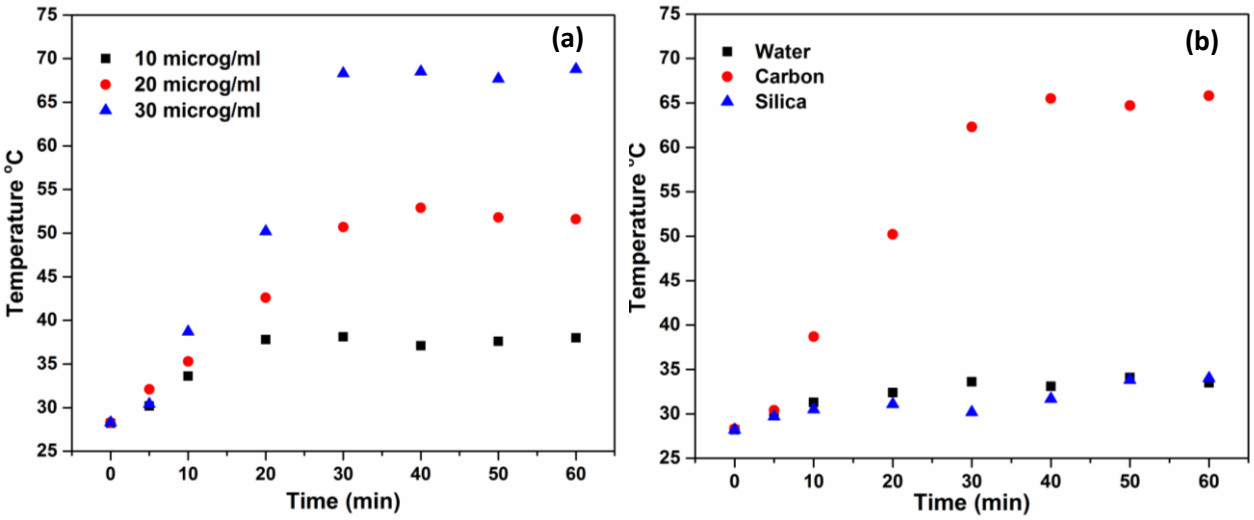

Fig. 6 Comparison plots of (a) photothermal property with respect to time and particle concentration of NCQDD-HCS-800 and (b) with mesoporous silica nanospheres.

Table 2 Comparison table of photothermal conversion efficiency for all synthesized nanoparticles.

Sample	Photothermal conversion efficiency (%)
NCQD-HCS-600	10.32
NCQD-HCS-700	37.13
NCQD-HCS-800	60.8
NCQD-HCS-900	76.3
NCQD	56.55

MTT study based on carrier under dark and NIR treatment

To validate the cytotoxic effect of our hollow spheres (NCQD-HCS-800), we directed cell viability in FaDu and HaCaT cells through MTT (3-(4,5-dimethyl thiazol-2-yl)-2,5-diphenyltetrazolium-bromide) assay. The hollow spheres impose negligible toxic effects under dark condition for both the cell lines (Figure 7). More than 80% HaCaT cells were found viable when exposed to light with incubated NCQD-HCS-800 whereas 33% FaDu cell

viability was observed under same conditions. Subsequently, the proliferation of FaDu cells decreased considerably with the increase in particle concentration (Figure 7b). The IC50 value of NCQD-HCS-800 was found to be 50 μg/ mL. Such a significant reduction in the proliferation of FaDu cells in comparison to other cells is attributable to the active intracellular uptake and photothermal effect of NCQD-HCS-800 particles under 980NIR laser irradiation. In contrast, HaCaT cells have negligible response to the temperature rise by NIR laser induced photothermal therapy which is further supported by flow cytometry analysis and confocal imaging .

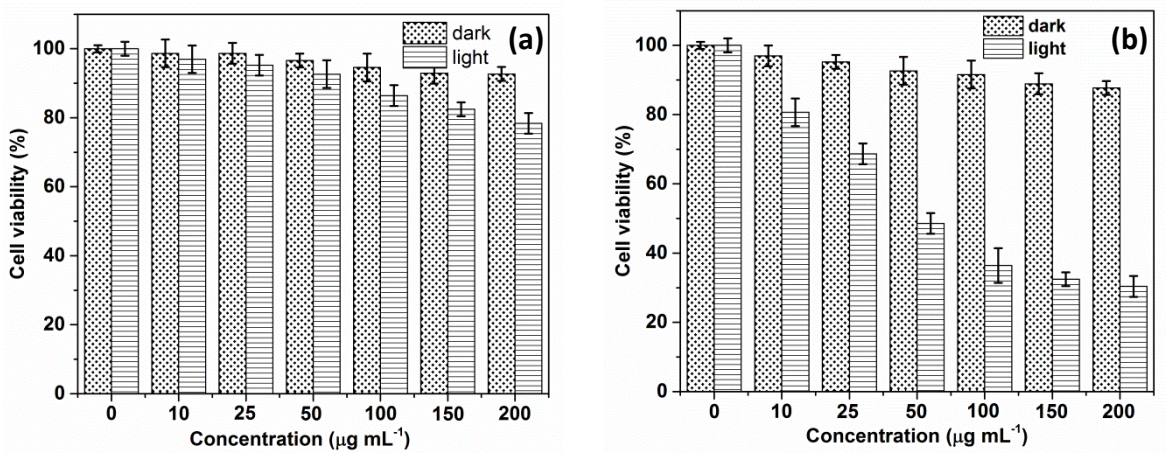

Fig. 7 Cell viability in (a) HaCaT and (b) FaDu cells under dark condition and 980 nm laser irradiation

Apoptotic analysis by Flow cytometry

A quantitative evaluation of the NCQD-HCS-800 nanoparticles mediated cell death was carried out using cell cycle analysis, using FACS. Significant cell death of 45% was observed for FaDu cells with respect to the control HaCaT cells under similar conditions, evidenced by fluorescence histogram (Figure 8). A decrease in cells in G0/G1 phase with an increase in cell concomitant in S and G2/M phase indicates that the arrest of cell cycle in S and G2/M phase was more prominent, when FaDu cells were irradiated with 980 nm laser. Figure 8c and 8f shows cell death increased from 4% to 45% (in FaDu) when compared to HaCat cell (2.4% to 5.1%) in treated cells. This detention is accountable for appreciable morphological changes in cell, as visualized by fluorescence microscopy, and ultimately resulted in cell death.

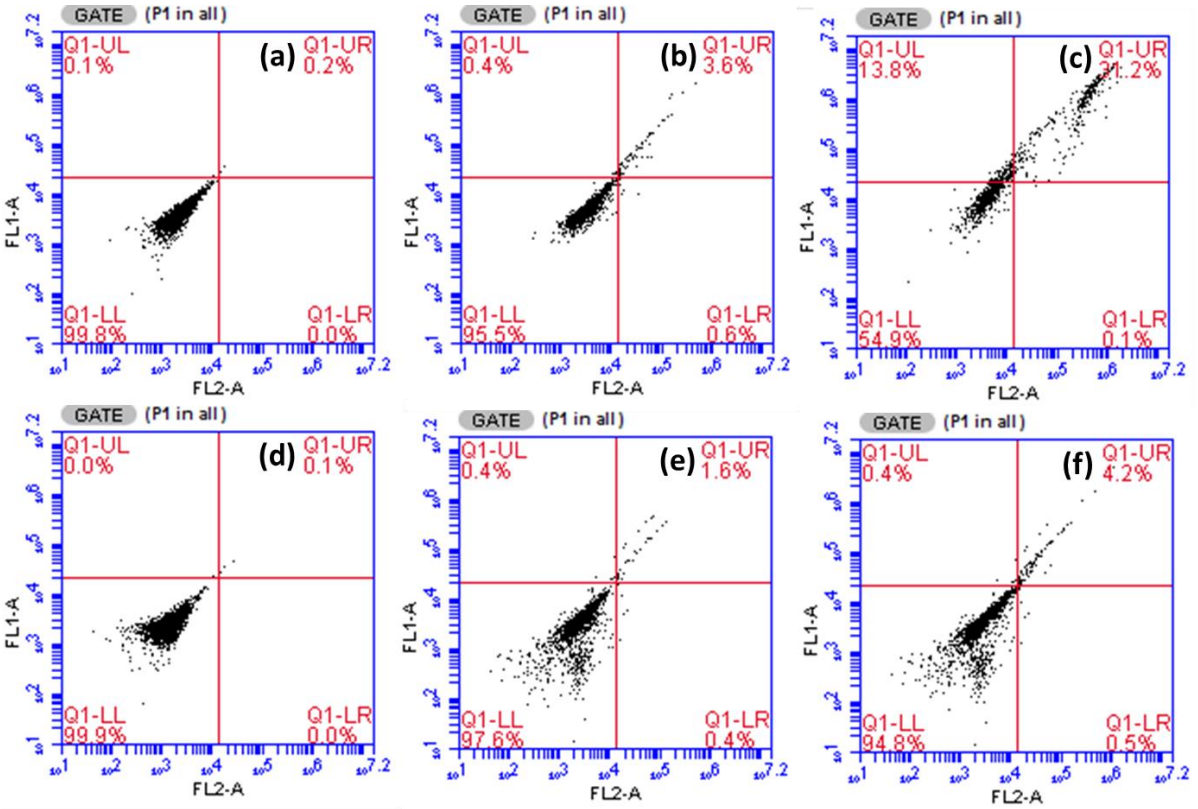

Fig. 8 Comparison plots of FaDu cells (a) control, (b) maintained in dark and (c) after treated with 980 nm irradiation and HaCaT cell line (d) control, (e) maintained in dark and (f) after treated with 980 nm irradiation (50 µg mL^{-1} NCQD-HCS-800 nanoparticles).

Confocal Imaging

In vitro cellular uptake of NCQD-HCS-800 nanospheres by the both FaDu and HaCat cells was investigated using confocal microscopy. Both the cells incubated with NCQD-HCS-800 nanocapsules in dark endocyted the capsules as evidenced by the intense green fluorescence signal coming from NCQD-HCS (488 nm excitation) in the cytoplasm leaving a clear nuclear zone (Fig. 8)**.** After irradiating with 980 nm laser for 5 and 10 minutes cycle, the cytoplasmic dissolution were observed in FaDu cells (Fig. 9c, 9d), which was not found in HaCaT cells. The DAPI staining supports our investigation by detecting nuclear deformation in FaDu cells after treated with laser source. These cellular changes can be attributed to formation of hot spots by NCQD-HCS-800 in the cellular environment, followed by triggering some cellular responses and sensitize the cells resulting in changing the plasmatic membrane function, activating thermally sensitive proteins, and overexpression of some proteins.[34,35]

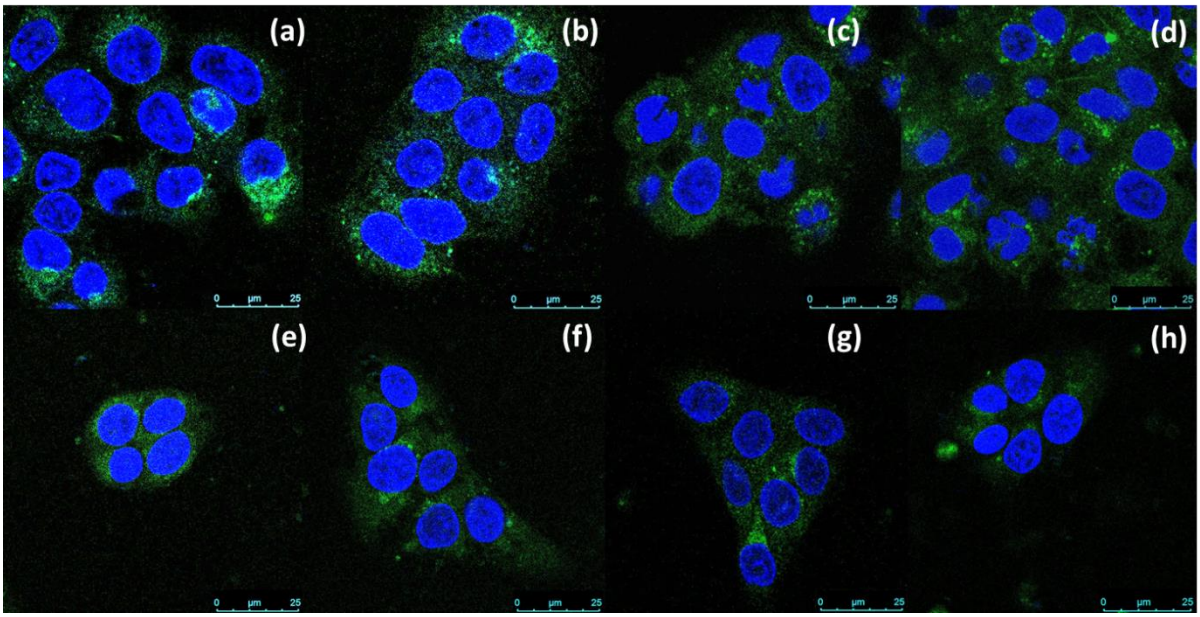

Fig. 9 Comparison plots of FaDu cells (a) control, (b) maintained in dark and after treated with 980 nm irradiation for (c) 5 min, (d) 10 min and HaCaT cell line (e) control, (f) maintained in dark and after treated with 980 nm irradiation for (g) 5 min and (h) 10 min (50 µg mL^{-1} NCQD-HCS-800 nanoparticles).

5.4 Conclusion

In this chapter,

- N-doped mesoporous hollow carbon spheres have been synthesized using polyaninile-co-polypyrrole block polymers.
- The synthesis condition has been optimized in order to produce materials with high photoluminescence as well as photothermal effect under NIR irradiation.
- The N-doped carbon hollow spheres showed high photothermal conversion efficiency.
- Thus, these materials may serve as promising PTT and fluorescence imaging agents without inducing obvious side effects for image-guided photothermal cancer treatment.

5.5 References

1 W. Busch, *Berliner Klinische Wochenschrift*, 1867, **13**, 5-137.

2 W. B. Coley, *Clin. Orthop. Relat. Res*., 1991, **262**, 3-11.

3 S. Lal, S. E. Clare and N. J. Halas, *Acc. Chem. Res*., 2008, **41**, 1842-1851.

4 E. Guisasola, A. Baeza, L. Asín, J. M. dela Fuente and M. V. Regí, *Small Methods*, 2018, **2**, 1800007.

5 M. P. Melancon, M. Zhou and C. Li, *Acc. Chem. Res*., 2011, **44**, 947-956.

6 X. Huang, S. Tang, X. Mu, Y. Dai, G. Chen, Z. Zhou, F. Ruan, Z. Yang and N. Zheng, *Nat Nanotechnol*., 2011, **6**, 28-32.

7 S. Zhang , C. Sun , J. Zeng , Q. Sun , G. Wang , Y. Wang ,Y. Wu , S. Dou , M. Gao and Z. Li, *Adv. Mater*., 2016, **28**, 8927-8936.

8 N. Li, Q. Sun, Z. Yu, X. Gao, W. Pan, X. Wan and B. Tang, *ACS Nano*, 2018, **12**, 5197-5206.

9 A. Espinosa, R. Di Corato, J. K. Tabi, P. Flaud, T. Pellegrino and C. Wilhelm, *ACS Nano*, 2016, **10**, 2436-2446.

10 X. Liang , Y. Li , X. Li , L. Jing , Z. Deng , X. Yue , C. Li and Z. Dai, *Adv. Funct. Mater*., 2015, **25**, 1451-1462.

11 A. K. Parchur, G. Sharma, J. M. Jagtap, V. R. Gogineni, P. S. LaViolette, M. J. Flister, S. B. White and A. Joshi, *ACS Nano*, 2018, **12**, 6597-6611.

12 W. He, K. Ai, C. Jiang, Y. Li, X. Song, L. Lu, *Biomaterials*, 2017, **132**, 37-47.

13 Q. Chen , C. Liang , C. Wang and Z. Liu, *Adv. Mater*., 2015, **27**, 903-910.

14 K. Yang , H. Xu , L. Cheng , C. Sun , J. Wang and Z. Liu, *Adv. Mater*., 2012, **24,** 5586-5592.

15 Jonathan F. Lovell, Cheng S. Jin, Elizabeth Huynh, Honglin Jin, Chulhong Kim, John L. Rubinstein, Warren C. W. Chan, Weiguo Cao, Lihong V. Wang and Gang Zheng, *Nat Mater*., 2011, **10**, 324-332.

16 Y. Li, T. Lin, Y. Luo, Q. Liu, W. Xiao, W. Guo, D. Lac, H. Zhang, C. Feng, S. W. Hogiu, J. H. Walton, S. R. Cherry, D. J. Rowland, D. Kukis, C. Pan and K. S. Lam, *Nat Commun*., 2014, **5**, 4712.

17 C. Liang , S. Diao , C. Wang , H. Gong , T. Liu , G. Hong , X. Shi , H. Dai and Z. Liu, *Adv. Mater*., 2014, **26**, 5646-5652.

18 C. Wang , L. Xu , C. Liang , J. Xiang , R. Peng and Z. Liu, *Adv. Mater*., 2014, **26**, 8154-8162.

19 Y. W. Bao, X. W. Hua, X. Chen and F. G. Wu, *Biomaterials*, 2018, **183**, 30-42.

20 S. M. Ardekani, A. Dehghani, M. Hassan, M. Kianinia, I. Aharonovich, V. G. Gomes, *Chem. Eng. J.*, 2017, **330**, 651-662.

21 P. Gong, L. Guo, M. Pang, D. Wang, L. Sun, Z. Tian, J. Li, Y. Zhang and Z. Liu, *J. Mater. Chem. B*, 2018, **6**, 3068-3077.

22 C. Gao, P. Dong, Z. Lin, X. Guo, B. P. Jiang, S. Ji, H. Liang and X. C. Shen, *Chem. Eur. J.*, 2018, **24**, 12827-12837.

23 F. Xu, Z. Tang, S. Huang, L. Chen, Y. Liang, W. Mai, H. Zhong, R. Fu and D. Wu, *Nat Commun.*, 2014, **6**, 7221.

24 C. Q. Zhou, J. Han, G. P. Song and R. Guo, *J. Polym. Sci. Pol. Chem.*, 2008, **46**, 3563-3572.

25 Q. Lu , Z. Wang, P. Wang and J. Li, *Nanoscale Res Lett.*, 2010, **5**, 761-768.

26 B. Guo, Q. Liu, E. Chen, H. Zhu, L. Fang and J. R. Gong, *Nano Lett.*, 2010, **10**, 4975-4980.

27 S. Mohapatra, S. R. Rout, R. K. Das, S. Nayak and S. K. Ghosh, *Langmuir*, 2016, **32**, 1611-1620.

28 Y. C. Chen, W. T. Chiu, J. C. Chen, C. S. Chang, L. H. C. Wang, H. P. Lin and H. C. Chang, *J. Mater. Chem. B*, 2015, **3**, 2447-2454.

29 L. Wang, Q. Sun, X. Wang, T. Wen, J. J. Yin, P. Wang, R. Bai, X. Q. Zhang, L. H. Zhang, A. H. Lu and C. Chen, *J. Am. Chem. Soc.*, 2015, **137**, 1947-1955.

30 L. Zhou, Y. Jing, Y. Liu, Z. Liu, D. Gao, H. Chen, W. Song, T. Wang, X. Fang, W. Qin, Z. Yuan, S. Dai, Z. A. Qiao and C. Wu, *Theranostics*, 2018, **8**, 663-675.

31 B. Geng, D. Yang, D. Pan, L. Wang, F. Zheng, W. Shen, C. Zhang and X. Li, *Carbon*, 2018, **134**, 153-162.

32 F. A. Permatasari, H. Fukazawa, T. Ogi, F. Iskandar and K. Okuyama, *ACS Appl. Nano Mater.*, 2018, **1**, 2368-2375.

33 H. Chen, J. Zhang, K. Chang, X. Men, X. Fang, L. Zhou, D. Li, D. Gao, S. Yin, X. Zhang, Z. Yuan and C. Wu, *Biomaterials*, 2017, **144**, 42-52.

34 L. Zou, H. Wang, B. He, L. Zeng, T. Tan, H. Cao, X. He, Z. Zhang, S. Guo and Y. Li, *Theranostics*, 2016, **6**, 762-772.

35 E. Guisasola, A. Baeza, L. Asín, J. M. D. Fuente and M. V. Regí, *Small Methods*, 2018, **2**, 1800007.

Chapter – 6

Upconverting Mesoporous Carbon Nanospheres with Light-responsive Molecular Gate for Gemcitabine Delivery and Fluorescence Imaging

6.1 Introduction

The inherent limitation of conventional chemotherapeutic drugs in cancer treatment has inspired the researchers to develop various nanotechnology based formulations owing to the uniquely appealing features for drug delivery, diagnosis and imaging as well as therapeutic nature of some nanomaterials themselves. In this particular area, mesoporous theranostic particles with high payload, controlled drug release, and imaging capability have received enormous attention due to their open framework structure, large surface area and well-defined porosity which make them potentially useful as a carrier of guest molecules. Conjugation, entrapment, absorption, and encapsulation of drugs and diagnostic agents in mesoporous network can result in combined loading, ultimately achieving the function of theranostics at the molecular and cellular level. Stimuli responsive mesoporous silica nanoparticles (MSNs) with adjustable pore sizes and large surface areas have been demonstrated as a theranostic platform to carry therapeutic cargoes as well as diagnostic agents.[1-3] Among externally controlled stimuli, light offers many advantages such as noninvasiveness, high temporal resolution, and the ability to be controlled remotely with relatively high local precision.[4,5]

A substantial number of papers on light actuated mesoporous silica based drug delivery systems have been published where the cargo molecules are retained while in storage and in circulation, but the delivery of their payload is finely controlled upon arriving at the desired target. For example Stoddart and Zink have published a number of papers on design of mechanized mesoporous silica modified with azobenzene impellers which intelligently controls the cargo release with variation in light intensity and irradiation time.[6-8] The same group have also reported another strategy for controlled molecular transport through cyclodextrin based reusable nanovalves where the release of the drug occurs through photosensitive cleavage of cyclodextrin.[9] The key in designing photo-controlled mechanized silica is the light triggered transformation of functional light responsive polymers/molecules through a photosensitizer to induce changes of the MSN drug loading systems which could further trigger the release of drugs.[5] Most of these systems have achieved limited success because of low tissue penetration and intense damage of living tissue by UV light used to excite sensitizer. To tackle this issue NIR-mediated MSN drug delivery vehicle has been designed by integrating upconverting nanoparticles within the pores of MSN.

Upon NIR radiation, NIR photons are upconverted into UV/vis photons by the UCNPs,[10] which in turn dissociates UV/Vis photosensitive gatekeeper molecules decorated on the mesopores of MSNs, realizing the controlled release of loaded drugs. In most cases, Tm^{3+} doped UCNPs are first coated with $mSiO_2$, forming core@shell or yolk@shell structures (UCNP@$mSiO_2$).**[11]** After drug loading, the mesopores are sealed by crosslinking with nitrobenzyl derived linker molecules. NIR radiation is converted by UCNPs into UV light, which in turn arouses the photochemical intramolecular reactions of NB, resulting in photolysis of NB to the nitroso derivatives, breaking the long-chain molecules and opening the ‘‘gate’’. However this kind of hybrid nanocarriers have several disadvantages like 1) multistep synthesis which ultimately results in product loss, 2) post synthesis coating process which results nonuniform distribution of one material over other, 2) low upconversion efficiency and high cost of rare earth materials can be a huge challenge for practical applications, 4) intrinsic drawbacks like low capacity for hydrophobic drug loading, easy flocculation of MSN in aqueous solutions, and lack of intrinsic optical properties do not present substantial scope for practical in vivo applications.

Mesoporous carbon nanoparticles (MCN) have received tremendous attention because of lower cytotoxicity, high surface area which ensures higher hydrophobic drug loading capacity and tunable emission properties. However, unlike other drug delivery carriers such as MSNs,[12,13] gold nanoparticles[14,15] or iron oxides,[16-19] the biomedical properties and applications of MCNs have been much less explored most probably due to the difficulties in fabricating hydrophilic, nanosized and highly dispersed MCNs which hold promises for the biological applications such as bioimaging, and also because of the lack of scope for functionalization of traditionally synthesized MCNs. The key to success in applications strongly depends on the ability to design well-defined MCNs, combined with highly porous structures with high density of surface functional groups. On the other hand, on-demand drug delivery using stimuli-responsive nanoparticles is useful for local and recurring therapies such as in the treatment of solid tumors because it minimizes the side effects associated with anticancer therapeutic agents.

This context ensures better NIR light responsive delivery of hydrophobic drug gemcitabine we have introduced luminescent mesoporous carbon hollow spheres with NIR cleavable molecular gate. Here, a substituted nitrobenzene organic linker as shown in scheme 1, has been designed to gate the loaded gemcitabine by simple alkyne-azide click reaction. The conjugation of drug has been established through FTIR studies. The DLS and zeta

potential studies over time ensure excellent stability of the nanoparticles in physiological medium. The in vitro cytotoxicity of the drug carrier was evaluated in human oral cancer cells (FaDu) through MTT assay. The cell killing ability of the multifunctional theranostic

particle was further investigated using flow cytometry and confocal analysis. We have explored the therapeutic effect of such type of multifunctional theranostic system for the treatment of human oral cancer cells. We anticipate that in comparison to porous silica based theranostics our system would have 1) better drug loading capability due to π-π stacking interaction of hydrophobic drugs with carbon carrier; 2) *in situ* upconversion property of embedded carbon quantum dots promotes photocleavage of molecular gate under NIR; 3) synergistic thermal ablation effect and chemotherapeutic effect ensures better curative response, 4) intense photoluminescence of carrier provides promising opportunity for image guided therapy.

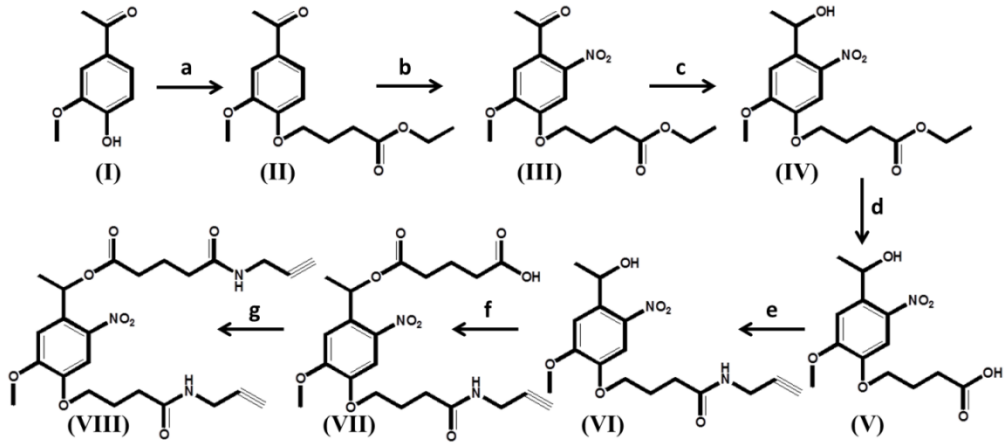

Scheme 1 Schematic presentation of the synthetic route for linker molecule.

6.2 Experimental

Chemicals

4-azidoaniline, acetovanillone, propargylamine, ethyl 4-bromobutyrate and deionized water were purchased from Sigma Aldrich. Petroleum ether and tetrahydrofuran was supplied by Thermofisher Scientific Chemicals. Dichloromethane, ethyl acetate and N,N-dimethylformamide was supplied by Spectrochem Ltd. Absolute ethanol was purchased from Changshu Yangyuan chemicals.

Synthesis of (II)

The starting material, 1-(4-hydroxy-3-methoxyphenyl)ethanone (I, 3 g, 18 mmol), ethyl-4-bromobutyrate (3 mL, 21.7 mmol), and potassium carbonate (3.7 g, 27 mmol) were

sequentially added to DMF (15 mL) and stirred overnight under nitrogen atmosphere. The reaction mixture was precipitated in deionized water (300 mL, 4°C); the mixture was stirred for 2 h for complete precipitation. Then, the precipitate was filtered and washed with deionized water. The product was dried at room temperature, and the final product was collected as a white powder (5.1 g, 96 wt.%). ^{1}H NMR (400 MHz, $CDCl_3$) δ 7.55-7.51 (m, 2H), 6.9 (d, 1H), 4.16-4.11 (m, 4H), 3.9 (s, 3H), 2.56-2.52 (m, 5H), 2.20-2.16 (m, 2H), 1.27-1.23 (t, 3H).

Synthesis of (III)

Ethyl 4-(4-acetyl-2-methoxyphenoxy)butanoate (II, 2.5 g, 9 mmol) was added slowly to a stirring solution of nitric acid (6 mL, 4°C, ice bath). The reaction was maintained in an ice bath for 1h until and monitored using thin-layer chromatography (TLC) (50:50 ethyl acetate:hexane, product RF ~ 0.5). Further, precipitation of the product was performed using deionized water. The completion of precipitation was achieved after overnight storage at 4°C. The yellow solid was collected using filtration and purified using column chromatography. (Yield of yellow solid product was 1.8 g, 69 wt.%). ^{1}H NMR (400 MHz, $CDCl_3$) δ 7.63 (s, 1H), 6.74 (s, 1H), 4.20-4.15 (m, 4H), 3.97 (s, 3H), 2.58-2.54 (t, 2H), 2.23-2.20 (t, 2H), 1.30-1.26 (t, 3H).

Synthesis of (IV)

Ethyl 4-(4-acetyl-2-methoxy-5-nitrophenoxy)butanoate (III, 2 g, 5.7 mmol) was added to 30 mL ethanol and sodium borohydride (0.15 g, 3.6 mmol) mixture. The reaction was stirred overnight at 35°C temperature. Then the mixture was precipitated in deionized water stirred for 4 h and stored overnight at 4°C. The precipitate was recovered by filtration and washed with deionized water to get a pale yellow powder (1.3 g, 71 wt.%) as the product. ^{1}H NMR (400 MHz, DMSO-d6) δ 6.73 (s, 1H), 6.58 (s, 1H), 6.15 (s, 1H), 4.73 (d, 1H), 3.86 (q, 4H), 3.1 (s, 3H), 1.66 (t, 2H), 1.19-1.11 (m, 2H), 0.51 (d, 3H), 0.39 (t, 3H).

Synthesis of (V)

Potassium hydroxide (0.13 g, 2.2 mmol) was added dropwise to a solution of 1:1 THF (10 mL) and water (10 mL) containing dissolved Ethyl 4-(4-(1-hydroxyethyl)-2-methoxy-5-nitrophenoxy)butanoate (IV, 0.5 g, 1.5 mmol) in it. The reaction mixture was stirred at room temperature for 4h. The precipitation of the product was performed by dropping the pH of the

reaction mixture to ~4 using hydrochloric acid. The resulting mixture was stored at 4°C for overnight to attain the product (0.36 g, 68 wt.%), recovered using filtration and dried using a vacuum oven at 40°C. ^{1}H NMR (400 MHz, DMSO-d6) δ 11.39 (s, 1H), 6.74 (s, 1H), 6.57 (s, 1H), 6.05-5.99 (m, 1H), 4.48 (q, 1H), 3.24 (t, 2H), 3.14 (s, 3H), 1.58 (t, 2H), 1.15 (p, 2H), 0.53 (d, 3H).

Synthesis of (VI)

4-(4-(1-hydroxyethyl)-2-methoxy-5-nitrophenoxy)butanoic acid (0.24 g, 0.8 mmol), NHS (1.7 mmol), EDC.HCl (1.7 mmol) and DCM (10 mL) were added into a round-bottomed flask and stirred for 30 min under inert atmosphere and dark condition. Then propargylamine (0.04 g, 0.8 mmol) was slowly injected at room temperature to the mixture and reaction was stirred overnight. A light yellow colour solid product was collected and washed with HCl (1 M), NaOH (1 M) and deionized water (Yield was found to be 0.22 g, 85 wt.%). ^{1}H NMR (400 MHz, DMSO-d6) δ 7.54 (t, 1H), 6.74 (s, 1H), 6.57 (s, 1H), 6.05-5.99 (m, 1H), 3.86 (m, 4H), 3.14 (s, 3H), 1.58 (t, 2H), 1.15 (p, 2H), 0.53 (d, 3H).

Synthesis of (VII)

4-(4-(1-hydroxyethyl)-2-methoxy-5-nitrophenoxy)-N-(prop-2-ynyl)butanamide (0.17 g, 0.5 mmol) was taken in a round bottom flask containing 15 ml DCM and was stirred for 10 min. Then succinic anhydride (0.05g, 0.5 mmol) and DMAP (0.06 g, 0.5 mmol) was added to this and the reaction was refluxed at 60°C for 12 h. Then the crude pale yellow solid was collected by drying the DCM, followed by the next synthetic step.

Synthesis of (VIII)

VII (0.27 g, 0.6 mmol) was dissolved in DCM (50 mL) under N_2 atmosphere, followed by addition of NHS (0.7 mmol) and EDC.HCl (0.7 mmol) respectively. Then propargylamine (0.04 g, 1 mmol) was slowly injected at room temperature to the mixture and reaction was stirred overnight. A yellow colour solid product was collected in ethyl acetate and washed with HCl (1 M) and deionized water. This yields in the synthesis of the linker molecule, used for gating of gemcitabine in mesoporous carbon spheres. (Yield was found to be 0.2 g, 65 wt.%). ^{1}H NMR (400 MHz, $CDCl_3$) δ 7.72 (t, 2H), 7.55 (s, 1H), 7.05 (s, 1H), 6.42 (m, 1H), 4.07-4.02 (m, 6H), 3.98 (s, 3H), 2.66-2.63 (m, 4H), 2.46-2.41 (m, 4H), 1.6-1.4 (m, 4H), 1.26 (d, 3H).

Synthesis of azide modified NCQD-HCS-800 nanoparticles

First, acid modified NCQD-HCS-800 was synthesized following the synthetic route described in chapter 5. Then, acid modified NCQD-HCS-800 (200 mg) was dispersed in 40 ml of deionized water followed by addition of 50 ml of EDC/NHS (1 mg ml^{-1}) mixture under stirring for 30 min at room temperature. After 1h, 4-azidoaniline (20 mg) was added to the mixture solution and stirred vigorously for 8h in the dark. The azide modified spheres were washed with ethanol and deionized water and dried under vacuum for 12h.

Encapsulation of drug using click chemistry

The azide-modified mesoporous carbon spheres (10 mg) were first incubated in phosphate-buffered saline (10 mM, 20 mL, pH 7.4) of gemcitabine hydrochloride (15 mg) for 12h at room temperature. The carbon spheres were recovered using centrifugation and washed with PBS buffer. Then, the drug loaded spheres were dried under high vacuum to produce the gemcitabine loaded nanoparticles. The drug loaded carbon spheres (50 mg) were dispersed in dry DMF (20 mL) under nitrogen atmosphere. Further, the linker molecule (VIII) was added slowly to the solution and stirred for 6h at room temperature.[20] After completion of reaction, the particles were centrifuged and washed with diethyl ether and ethanol, and dried for further experiments.

Gemcitabine release under NIR irradiation

The linker gated gemcitabine loaded NCQD-HCS-800 were taken in a PL cuvette and irradiated with 980 nm NIR laser (1 Wcm^{-2}). The distance between the source and particles was maintained at 8.4 cm. The release of gemcitabine was examined by the UV-Vis spectrophotometer (λmax = 266 nm). Control experiments were conducted in same conditions under dark.

Cytotoxicity assays

FaDu cells (1×10^4 cells) were seeded separately into 96-well plates and incubated in 200 µL Minimum essential medium (MEM) and HaCaT cells (1×10^4 cells) were seeded separately into 96-well plates and incubated in 200 µL Dulbecco's modified Eagle's medium (DMEM) containing 10% FBS for 24 h (37 °C, 5% CO_2). After incubation, cells were treated with 50 µg/mL of linker gated gemcitabine loaded NCQD-HCS-800 for 6 h. Following treatment was done by irradiating 980 nm laser (1W) maintaining a distance of 2.5 cm for 5 minutes per

well. After 3 h of incubation, MTT solution was removed and replaced with 200 μL of DMSO. Absorbance was read at 570 nm using a microplate reader. The experiment was performed three times independently. Control experiments were conducted under the same dark conditions.

Apoptotic analysis by flow cytometry

Cell cycle analysis by flow cytometry with PI staining was performed using FaDu and HaCaT cells were incubated for 12 h in the presence of 50 μg mL^{-1} concentration of linker gated gemcitabine loaded NCQD-HCS-800 nanoparticles at 37°C in 5% CO_2 incubator. Then each well was exposed to 980 nm laser (1W) maintaining a distance of 2.5 cm for 5 minutes. The cells were then harvested with trypsinisation and fixed with chilled 70% ethanol and stored at -20 °C. Then, the cells were washed with ice cold PBS (10 mM, pH 7.4) and incubated with 20 μl of DNAase-free RNase (10 mg mL^{-1}) and 20 μl of DNA intercalating dye PI (1 mg mL^{-1}) at 37 °C for 10 min in the dark. The distribution of cells in the different cell-cycle phases was analysed from the DNA histogram using a Becton-Dickinson FACS Calibur flow cytometer and analysed with Flow Jo software (BD ACCURI C6).

DAPI staining for nuclear morphology study

To study the nuclear morphology of the FaDu and HaCaT cells, DAPI staining was performed following the earlier reported procedure. FaDu cells incubated with linker gated gemcitabine loaded NCQD-HCS-800 nanoparticles and treated with NIR irradiation in vitro for 24h. The cells were fixed with 3.7% formaldehyde for 15 min, permeabilized with 0.1% Triton X-100 and stained with 1 mg/ml DAPI for 5 min. The cells were then washed with PBS and examined under fluorescence microscopy (Olympus IX 70).

6.3 Results and discussion

We synthesized the NIR cleavable linker VIII (Scheme 1) to gate gemcitabine in the hollow matrix of NCQD-HCS-800 nanoparticles. The metal-free click chemistry between azide modified hollow carbon spheres and triple bond of linker molecule (VIII) provides a novel strategy to hold the drug effectively within the system (Scheme 2).

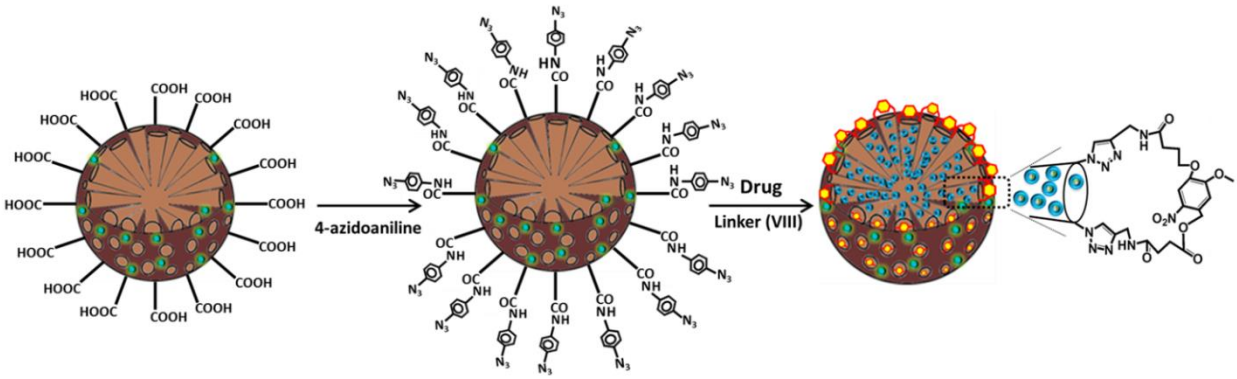

Scheme 2 Schematic presentation of linker gated drug loaded NCQD-HCS-800 spheres.

Particle size distribution and zeta potential

The particle size of various carbon spheres synthesized at different temperature is compared in Fig. 1a. It was observed that with the raise in reaction temperature the particle size decreased for NCQD-HCS particles. Simultaneously, after surface modification with azide and (VIII) the particle size of NCQD-HCS-800 changed within a range of $\pm$ 20 nm respectively. Furthermore, the surface charge analysis after post modifications on NCQD-HCS-800 has been shown in Fig. 2. It exhibits that the surface of linker (VIII) gated carbon spheres are nearly neutral at pH 6.3. Thus, the particle size and zeta potential data supports that the nanoformulation is suitable towards application *in vivo* treatment of cancer.

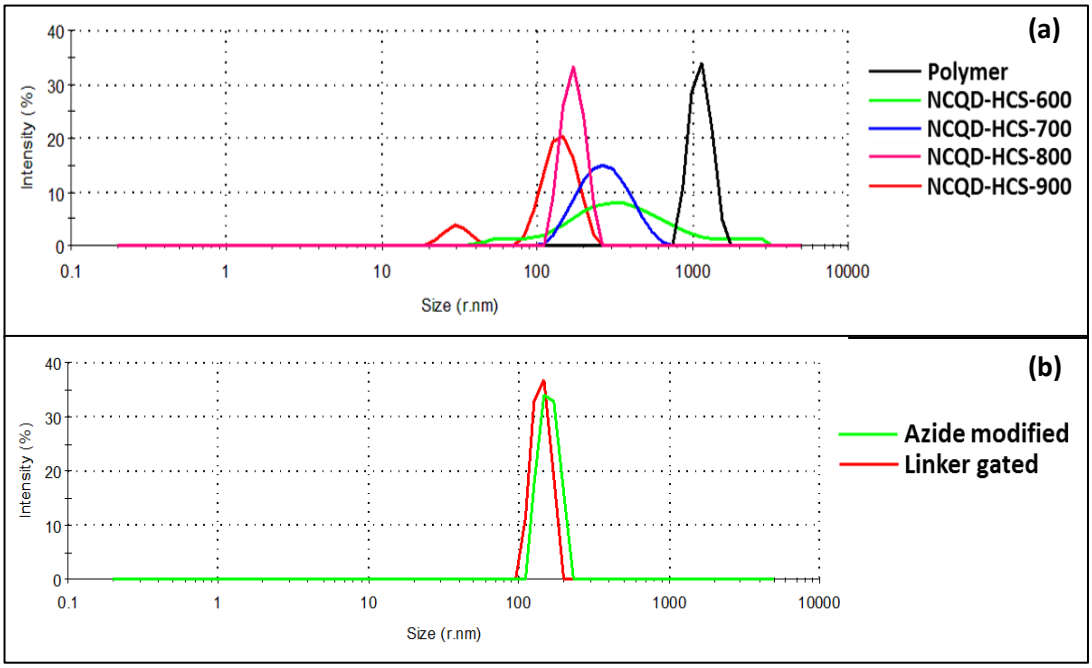

Fig. 1 (a) Comparison of various particle sizes of NCQD-HCS carbon nanospheres synthesized at different reaction temperature and (b) NCQD-HCS-800 after surface modification.

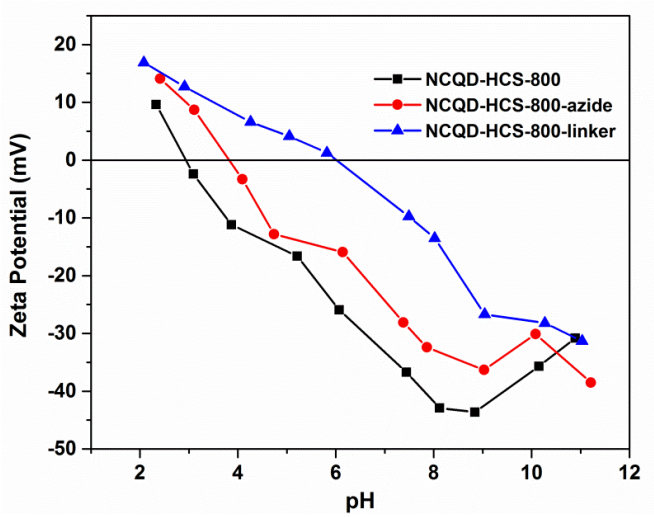

Fig. 2 Zetapotential of NCQD-HCS-800 after post synthetic surface modifications.

Gemcitabine loading using click chemistry

Due to the high surface area and porous network structure, azide-functionalized NCQD-HCS-800 can work as an excellent adsorbent for anticancer drug gemcitabine. The gemcitabine loading capacity of azide-functionalized NCQD-HCS-800 was determined by soaking the particles in 15 mL of gemcitabine solution (1 mg/mL) prior to gating with linker (VIII). The drug encapsulation efficiency was found to be 88% (Fig. 3) and with a drug loading content % of 15.7%. Then the particles were suspended in DMF for linker conjugation. To verify the surface modification and gating with linker on the carbon spheres, FTIR study was performed for different stages of synthesis (Fig. 4). The conjugation between azide modified hollow carbon spheres and linker molecule was confirmed by the disappearance of IR peak at 2110 cm^{-1}, which indicated the $–N_3$ modification on carbon spheres.

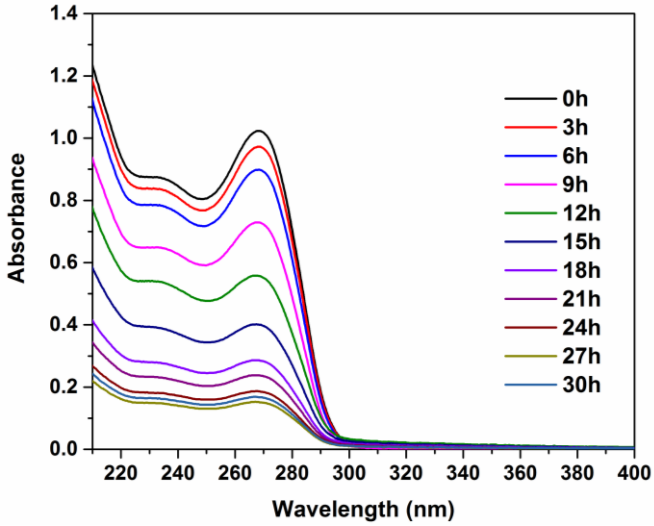

Fig. 3 UV absorbance spectra intensity of gemcitabine and supernatant after loading at different interval of time.

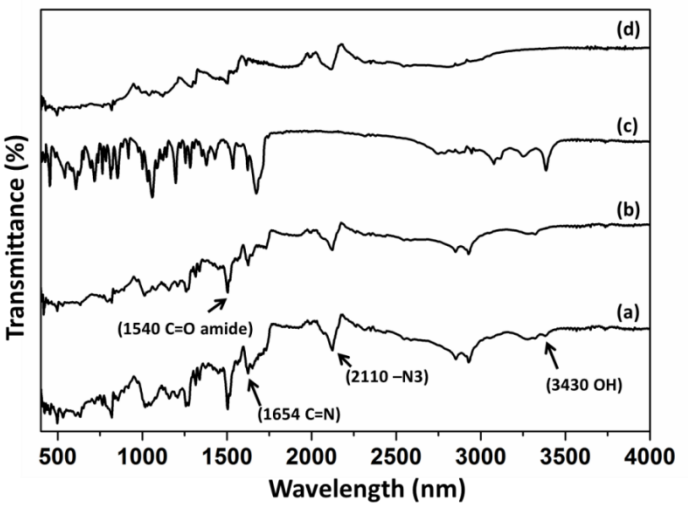

Fig. 4 FTIR spectra of (a) azide modified NCQD-HCS-800, (b) linker conjugated NCQD-HCS-800, (c) gemcitabine and (d) linker conjugated gemcitabine loaded NCQD-HCS-900.

$$\text{Drug loading content (\%)} = \frac{\text{Weight of the drug in nanoparticles}}{\text{Weight of the nanoparticles}} \times 100$$

$$= \frac{0.0078}{0.05} \times 100 = 15.7\%$$

$$\text{Encapsulation efficiency (\%)} = \frac{\text{Weight of the drug in nanoparticles}}{\text{Weight of the nanoparticles}} \times 100$$

$$= \frac{0.044}{0.05} \times 100 = 88\ \%$$

Gemcitabine release under NIR irradiation

After confirmation of photocleavage of linker (VIII) by NIR light, we encapsulated gemcitabine as a model drug (linker capped gemcitabine loaded NCQD-HCS-800). The gemcitabine was added prior to the final gating step with linker, and we monitored its release under 980 nm NIR irradiation, using UV-Vis spectroscopy. Fig. 5a shows burst release of 68% drug within 10 min of light exposure whereas in dark the release is only upto 18%. When subjected to on-off irradiation time with 6 min on and 4 min off irradiation, the stimuli based controlled release of drug was observed in the developed system (Fig. 5b). To commensurate the light responsive drug release mechanism, we compared the emission spectra of NCQD-HCS-800 under 980 nm excitation and the absorbance spectra of linker (VIII) molecule (Fig. 6A). The emission peak at 340 nm overlaps the absorbance peak of photocleavable linker. On the other hand, Fig. 6B shows hypochromic shift of the absorbance

peak of linker molecule, when subjected to 340 nm UV irradiation for different interval of time.

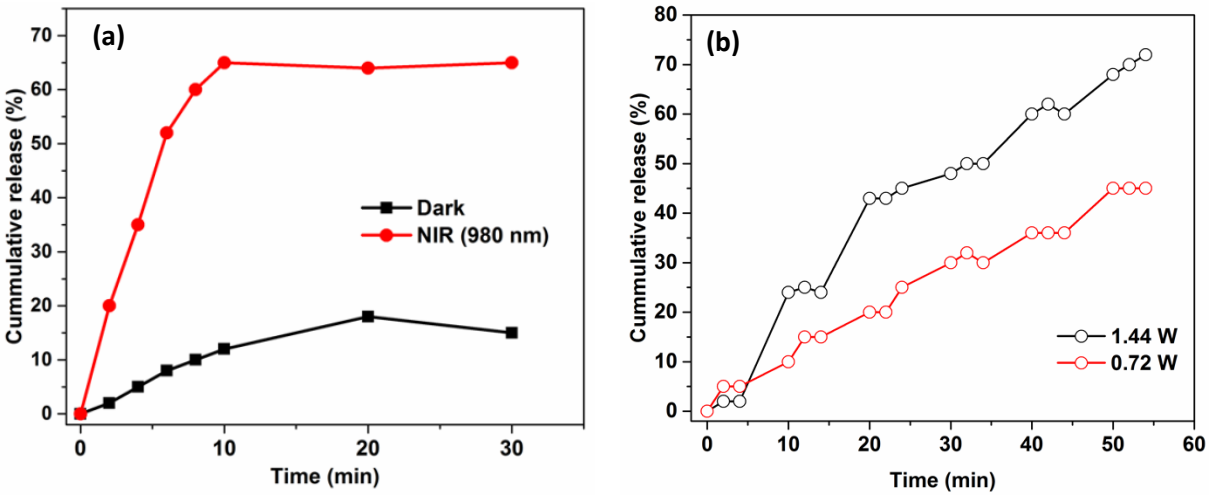

Fig. 5 (a) Gemcitabine release profile by linker gated NCQD-HCS-800 and (b) Cumulative release of gemcitabine from NCQD-HCS-900 as a function of time in the periodic irradiation of NIR laser with different power density.

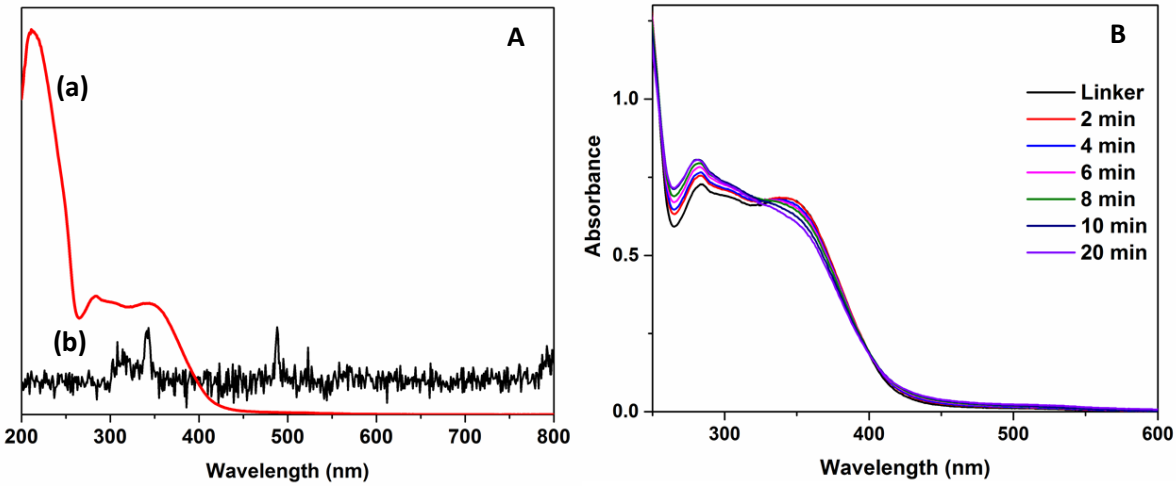

Fig. 6 A (a) UV absorbance plot of linker versus upconversion spectra (λ_{ex} = 980 nm) of NCQD-HCS-800 and (b) time based UV absorbance spectra of linker molecule under 340 nm irradiation.

MTT study under dark and NIR treatment

To verify cytotoxic effect of the nanodrug delivery system (gemcitabine loaded linker gated NCQD-HCS-800), we verified cell viability in FaDu cells through MTT (3-(4,5-dimethyl thiazol-2-yl)-2,5-diphenyltetrazolium-bromide) assay. The carbon spheres impose negligible toxic effects under dark condition for both the cell line (Fig. 7). More than 95% FaDu cells were found viable when incubated in dark condition whereas 24% FaDu cell viability was observed under exposure of 20 min of irradiation. Subsequently, the proliferation of FaDu cells decreased considerably with the increase in time of 980 nm laser exposure (Fig. 7). As

found in chapter 5, IC_{50} value of NCQD-HCS-800 was found to be 50 µg/ mL and hence the particle concentration was maintained to that concentration while conducting these experiments. Such a significant reduction in the proliferation of FaDu cells in comparison to other cells is attributable to the active intracellular uptake, and combinatorial (photothermal and chemo-) effect of gemcitabine loaded linker gated NCQD-HCS-800 particles under 980NIR laser irradiation. In contrast, NIR laser induced combinatorial therapy is further evidenced by flow cytometry analysis and confocal imaging under same conditions.

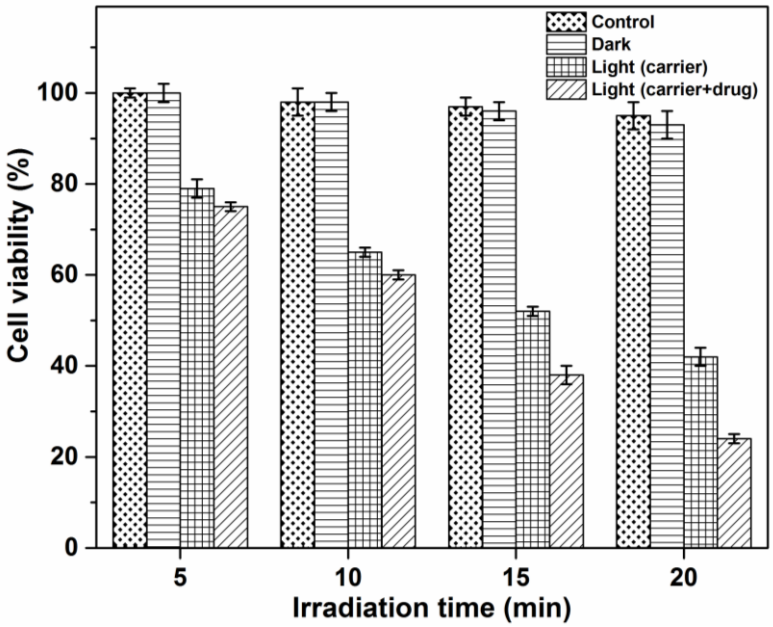

Fig. 7 Cell viability in FaDu cells with respect to time of 980 nm laser exposure.

FACS study dark and NIR treatment

A quantitative evaluation of combinatorial therapy (chemo- and photothermal) can be visualized from the gemcitabine loaded NCQD-HCS-800 nanoparticles. Although gemcitabine is rarely applied in oral cancer treatment, the overall effect of our designed system was able to establish a cell death of 61% under 10 min irradiation and 78% under 20 min irradiation time in FaDu cells (Fig. 8). As compared to the photothermal based cell killing with respect to findings in chapter 5, the chemotherapeutic effect was found to be 16 and 20% with raise in irradiation time. A decrease in cells in G0/G1 phase with an increase in cell concomitant in S and G2/M phase indicates that the arrest of cell cycle in S and G2/M phase was more prominent, when FaDu cells were irradiated with 980 nm laser. Figure 8c and 8d shows cell death raise of 17 % (in FaDu) with response to increase in irradiation time

from 10 min. This detention is accountable for appreciable morphological changes in cell, as visualized by fluorescence microscopy, and ultimately resulted in cell death.

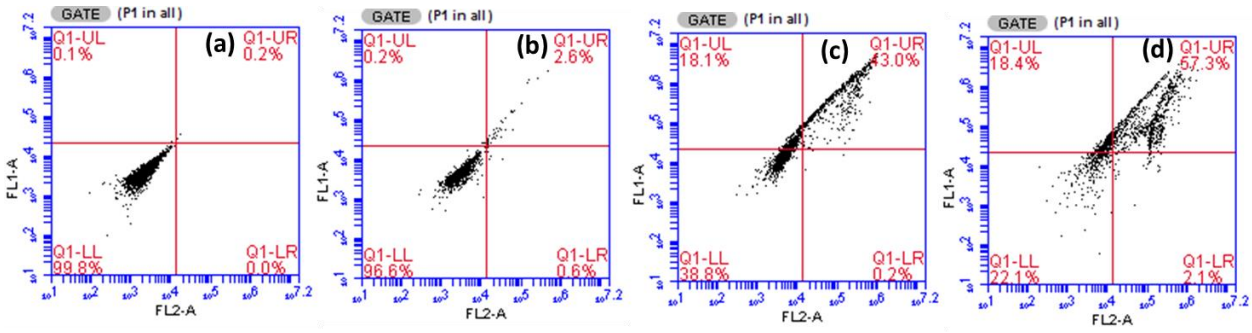

Fig. 8 Comparison plots of FaDu cells (a) control, (b) in dark, (c) 10 min and (d) 20 min of laser irradiation.

Confocal Imaging

In vitro cellular uptake of NCQD-HCS-800 nanospheres by both FaDu and HaCat cells was investigated using confocal microscopy. Both the cells incubated with NCQD-HCS-800 nanocapsules in the dark, endocyted the capsules as evidenced by the intense green fluorescence signal coming from NCQD-HCS (488 nm excitation) in the cytoplasm leaving a clear nuclear zone (Fig. 9)**.** After irradiating with 980 nm laser for 5 and 10 minutes cycle, the cytoplasmic dissolution was observed in FaDu cells (Fig. 9c, 9d), which was not found in HaCaT cells. The DAPI staining supports our investigation by detecting nuclear deformation in FaDu cells after being treated with laser source. These cellular changes can be attributed to formation of hot spots by NCQD-HCS-800 in the cellular environment, followed by triggering of some cellular responses and sensitize the cells, resulting in changing the plasmatic membrane function, activating thermally sensitive proteins, and overexpression of some proteins.[21,22]

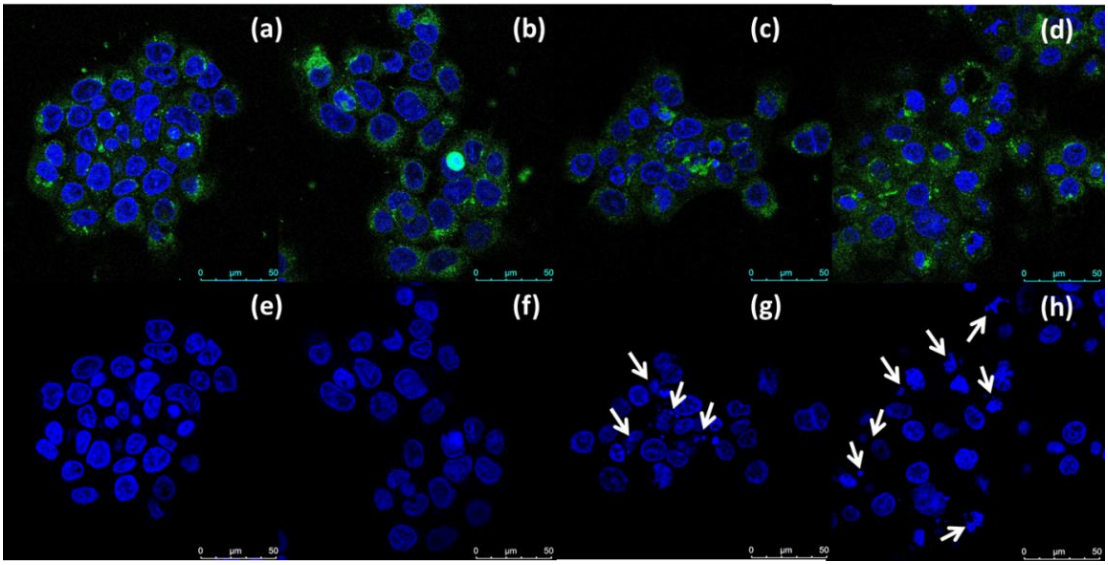

Fig. 9 Comparison plots of FaDu cells (a) control, (b) maintained in dark and after treated with 980 nm irradiation for (c) 10 min, (d) 20 min and DAPI stained nucleus of FaDu cells (e) control, (f) maintained in dark and after treated with 980 nm irradiation for (g) 10 min and (h) 20 min (50 µg mL^{-1} NCQD-HCS-800 nanoparticles).

Proposed mechanism for the combinatorial effect by our designed system

The design of our final theranostic construct has been presented in scheme 2. The upconversion property of carbon quantum dots and doped carbon dots has been extensively studied by our laboratory and other research groups.[23-27] As shown in Fig. 3A, upon irradiation with a 980 nm laser, several emission processes are expected to occur in NCQD with in the range 250 nm to 550 nm. Since our synthesized photocleavable linker *(VIII)* absorbs at 340 nm, the emitted radiation from NCQD at 340 nm introduces photoreactions of o-nitrobenzyl groups present in *VIII*. Hence the cleavage of the gate initiates the release of the drug. Furthermore, the π-π stacking interaction is disrupted in acidic pH which is frequently observed in cancer cell microenvironment. At the same time the mesoporous NCQD-HCS-800 absorbs radiation from 980 nm and raises the local temperature realising photothermal therapy.

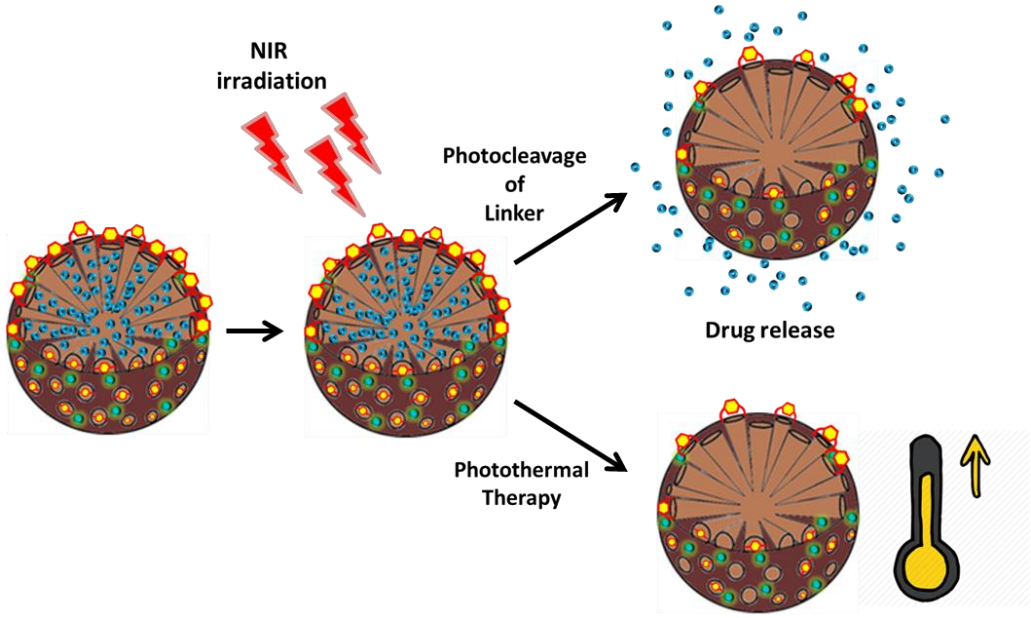

Scheme 3 Plausible mechanism for the combinatorial therapy by our nanotheranostic carbon spheres.

6.4 Conclusion

In this chapter,

- Mesoporous hollow carbon spheres with gemcitabine encapsulation efficiency of 88% have been constructed.
- The combinatorial cell killing efficiency owing to the photothermal effect and chemotherapeutic effect has been investigated in detail in human oral cancer cells.
- The combinatorial therapy was found to decrease the cancer cell viability up to 22% within 20 min (5 min pulse) of NIR irradiation.
- A high luminescence quantum yield of 14.6% opens opportunity towards bioimaging.

6.5 References

1. P. Yang, S. Gai and J. Lin, *Chem. Soc. Rev.*, 2012,**41**, 3679-3698.
2. K. Möller and T. Bein, *Chem. Mater.*, 2017, **29**, 371-388.
3. J. Wen, K. Yang, F. Liu, H. Li, Y. Xu and S. Sun, *Chem. Soc. Rev.*, 2017,**46**, 6024-6045.
4. G. Yang, X. Sun, J. Liu, L. Feng and Z. Liu, *Adv. Funct. Mater.*, 2016, **26**, 4722-4732.
5. T. Zhao, L. Chen, Q. Li and X. Li, *J. Mater. Chem. B*, 2018, **6**, 7112-7121.
6. S. Angelos, E. Choi, F. Volgtle, L. D. Cola and J. I. Zink, *J. Phys. Chem. C*, 2007, **111**, 6589.

7. D. P. Ferris, Y. L. Zhao, N. M. Khashab, H. A. Khatib, J. F. Stoddart and J. I. Zink, *J. Am. Chem. Soc.*, 2009, **131**, 1686-1688.
8. J. Lu, E. Choi, F. Tamanoi, J. I. Zink, *Small*, 2008, **4**, 421-426.
9. D. Tarn, D. P. Ferris, J. C. Barnes, M. W. Ambrogio, J. F. Stoddart and J. I. Zink, ***Nanoscale***, 2014,**6**, 3335-3343.
10. G. Jalani, R. Naccache, D. H. Rosenzweig, L. Haglund, F. Vetrone and M. Cerruti, *J. Am. Chem. Soc.*, 2016, **138**, 1078-1083.
11. L. Sun, X. Ge, J. Liu, Y. Qiu, Z. Wei, B. Tian and L. Shi, *Nanoscale*, 2014, **6**, 13242-13252.
12. X. Hao, X. Hu, C. Zhang, S. Chen, Z. Li, X. Yang, H. Liu, G. Jia, D. Liu, K. Ge, X. J. Liang and J. Zhang, *ACS Nano*, 2015, **9**, 9614-9625.
13. F. Tang, L. Li and D. Chen, *Adv. Mater.*, 2012, **24**, 1504-1534.
14. G. Chen, Y. Xie, R. Peltier, H. Lei, P. Wang, J. Chen, Y. Hu, F. Wang, X. Yao and H. Sun, *ACS Appl. Mater. Interfaces*, 2016, **8**, 11204-11209.
15. S. Han, A. Samanta, X, Xie, L. Huang, J. Peng, S. J. Park, D. B. L. Teh, Y. Choi, Y. T. Chang, A. H. All, Y. Yang, B. Xing and X. Liu, *Adv.Mater*., 2017, **29**, 1700244.
16. Y. Zhu, Z. Lei and Y. Tian, *Dalton Trans.*, 2014, **43**, 7275-7281.
17. K. Cheng, S. Peng, C. Xu and S. Sun, *J. Am. Chem. Soc.*, 2009, **131**, 10637-10644.
18. S. W. Cao,Y. J. Zhu, M. Y. Ma, L. Li and L. Zhang, *J. Phys. Chem. C*, 2008, **112**, 1851-1856.
19. B. Q. Lu, Y. J. Zhu, F. Chen, C. Qi, X.Y. Zhao and J. Zhao, *Chem Asian J.*, 2014, **9**, 2908-2914.
20. L. S. C. Verduyn, L. Mirfeizi, A. K. Schoonen, R. A. Dierckx, P. H. Elsinga and B. L. Feringa, *Angew. Chem. Int. Ed*., 2011, **50**, 11117-11120.
21. L. Zou, H. Wang, B. He, L. Zeng, T. Tan, H. Cao, X. He, Z. Zhang, S. Guo and Y. Li, Theranostics, 2016, 6, 762-772.
22. E. Guisasola, A. Baeza, L. Asín, J. M. D. Fuente and M. V. Regí, Small Methods, 2018, 2, 1800007.
23. S. Mohapatra, S. R. Rout, R. K. Das, S. Nayak and S. K. Ghosh, *Langmuir*, 2016, **32**, 1611-1620.
24. R. K. Das and S. Mohapatra, *J. Mater. Chem. B*, 2017, **5**, 2190-2197.
25. Y. Zhang and J. He, *Phys. Chem. Chem. Phys*., 2015, **17**, 20154-20159.
26. A. S. Castillo, M. A. Avidad, C. Pritz, M. C. Robles, B. Fernandez, M. J. Ruedas-Rama, A. M. Ferna´ndez, A. L. Ferna´ndez, F. S. Gonzalez, A. S. Fischer and L. F. C. Vallvey, *Chem. Commun*., 2013, **49**, 1103-1105.
27. A. M. Alam, B. Y. Park, Z. K. Ghouri, M. Park and H. Y. Kim, *Green Chem.*, 2015, **17**, 3791-3797.

Chapter – 7

Summary and future scope

7.1 Summary

The doping of heteroatom in carbon quantum dots provides improved photophysical and chemical properties for its application in ultrasensitive sensing and targeted treatment of human cancer cells. With respect to this, the work addressed in this doctoral thesis addresses development of some smart multifunctional carbon quantum dots which can be used for the detection of biologically important agents and administration of widely accepted anticancer drugs like 5-fluorouracil and gemcitabine. The luminescence properties of these nanoparticles opens the possibility for monitoring the therapeutic response through fluorescence and MRI based bioimaging. The major findings of the present thesis work are as follows:

- Highly luminescent, B, N, S doped carbon quantum dots have been synthesized by one step hydrothermal approach. The BNSCQD probe strongly binds to glucosamine at nanomolar levels with a detection limit of 0.75 nM. To the best of our knowledge, this is the only quantum dot based sensor operating in the visible region for the detection of glucosamine at the nanomolar level.

- A simple fluorescence turn on sensor for the detection of fluoride ion in totally aqueous medium at neutral pH has been developed by integrating boronic acid functionalized carbon quantum dot (BNSCQD) and dopamine. This CQD sensor was successfully used in real samples and human serum samples. Cellular toxicity test showed that BNSCQD possess low toxicity. Our fluorescence sensor can efficiently be used to monitor fluoride contamination inside the cell.

- A novel type of multifunctional hybrid nanoparticle composed of magnetic gadolinium oxide-iron oxide core, mesoporous silica shell gated with BNSCQD has been constructed. The overall size of this theranostic construct is 42 nm and it is highly stable in aqueous medium. The recognition and fluorescence turn on response of BNSCQD toward cell surface glycan sialyl Lewis^a (SL^a) enables targeted drug release and excellent fluorescence imaging of SL^a overexpressed HepG2 cancer cells.

- N-doped mesoporous hollow carbon spheres have been synthesized using polyaninile-co-polypyrrole block polymers. These mesoporous carbon hollow spheres were efficient in generating localized thermal ablation effect in FaDu cells, under a 980 nm laser irradiation. Impressive fluorescence property of these nanospheres allows in vitro imaging of cancer at different excitation wavelengths.

- N-doped mesoporous hollow carbon spheres acts as an excellent carrier for loading hydrophobic anticancer drug gemcitabine. The substituted nitrobenzene organic linker gate tightly holds the drug in the mesoporous network and minimises the possibility of premature drug release. Such a theranostic nanoparticle shows elevated cell killing effect due to combined chemotherapeutic and photothermal therapy.

7.2. Future scope

Although there are many exciting potential biomedical applications of luminescent heteroatom doped carbon quantum dots, considerable challenges and issues remain to be resolved. Some issues such as the exact origin of fluorescence, the role of dopant ions, and their location in CQD were not resolved yet. Thus, these issues should be addressed for fundamental understanding and tuning the luminescence properties of doped CQD. So far for the recovery of CQD from reaction medium tedious techniques like column chromatography and/or dialysis are adopted. The scaling up of the fabrication techniques is the most important for their practical pharmaceutical applications.

Inventive design of NIR responsive nanocarriers has allowed unprecedented control over the drug delivery process through the use of NIR radiation with deep tissue penetration. However, investigation on the toxicological properties of materials needs more careful examination of the nanocarriers circulation, accumulation and metabolism, to give researchers a more systematic understanding of the fate of materials in the body.

Complexity of biological systems restricts nanoparticles with a single therapeutic effect and often fails to meet their purpose, leading to problems such as drug resistance. ROS generating properties of carbon nanomaterials has recently been explored. Hence the developed multifunctional theranostic materials can be evaluated for their possible application in photodynamic therapy.

List of Publications

Thesis related publications

(1) **R. K. Das** and S. Mohapatra, Highly luminescent, heteroatom-doped carbon quantum dots for ultrasensitive sensing of glucosamine and targeted imaging of liver cancer cells, ***Journal of Materials Chemistry B***, 2017, 5, 2190-2197. (Citations: 32) RSC (**Most cited original research article 2017**)

(2) **R. K. Das**, A. Pramanik, M. Majhi, and S. Mohapatra, Magnetic mesoporous silica gated with doped carbon dot for site specific drug delivery, fluorescence and MR imaging, ***Langmuir***, 2018, 34, 5253-5262. (Citations: 9) ACS

(3) S. Mohapatra and **R. K. Das**, Novel hetero atom doped carbon quantum dot probe for fluorescence detection of fluoride ion in total aqueous medium, ***Analytica Chimica Acta***, 2019, 1058, 146-154. ELSEVIER

(4) Synthesis and Characterization of Heteroatom Doped Hollow Carbon Spheres for Fluorescence Imaging and Photothermal Therapy of Cancer. (manuscript submitted)

(5) Upconverting Mesoporous Carbon Nanospheres with Light-responsive Molecular Gate for Gemcitabine Delivery and Fluorescence Imaging. (manuscript under preparation)

Additional publications

(1) S. Mohapatra, S. R. Rout, **R. K. Das**, S. Nayak and S. K. Ghosh, Highly hydrophilic luminescent magnetic mesoporous carbon nanospheres for controlled release of anticancer drug and multimodal imaging, ***Langmuir***, 2016, 32, 1611-1620. (Citations: 43) ACS

(2) **R. K. Das**, J. P. Kar and S. Mohapatra, Enhanced photodegradation of organic pollutants by carbon quantum dot (CQD) deposited Fe3O4@mTiO2 nano-pom-pom balls, ***Industrial & Engineering Chemistry Research***, 2016, 55, 5902-5910. (Citations: 10) ACS

(3) S. Mohapatra, M. K. Bera, and **R. K. Das**, Rapid "turn-on" detection of atrazine using highly luminescent N-doped carbon quantum dot, ***Sensors and Acutators B***, 2018, 263, 459-468. (Citations: 9) ELSEVIER

Achievements

(1) "Best Oral Presentation Award" at *World Congress on Drug Discovery and Development* 2016, BioGenesis Health Cluster at Indian Institute of Science, Bangalore.

(2) "ISNM-BC (Beckman Coulter) Industrial Best Poster Award" at *Nanobioteck* 2017 (Indian Society of Nanomedicine-AIIMS Delhi), Indian Institute of Science Education and Research, Thiruvananthapuram.

(3) "Best Research Poster Award" in Department of Chemistry, National Institute of Technology, Rourkela at *Research Scholars Week* 2018.

Conferences attended

(1) National Conference on "Advances in Chemistry and their Biological and Industrial Relevance" (ACBIR). NIT Rourkela. 10-11th January 2014. (Poster presentation)
(2) World Congress on Drug Discovery & Development "Highly hydrophilic luminescent magnetic mesoporous carbon nanospheres for controlled release of anticancer drug and multimodal imaging" IISc Bangalore, India. 23-25th November 2016. (Oral Presentation)
(3) International Conference on Recent Advances in Material Chemistry Utkal University, India. 24-26th February 2017. (Poster Presentation)
(4) NANO INDIA 2017 IIT Delhi, India. 15-16th March 2017. (Poster Presentation)
(5) 21st CRSI National Symposium in Chemistry CSIR-IICT Hyderabad, India. 14-16th July 2017.
(6) Annual Conference of Indian Society of Nanomedicine (ISNM) IISER Thiruvananthapuram, India. 6-8th December 2017.